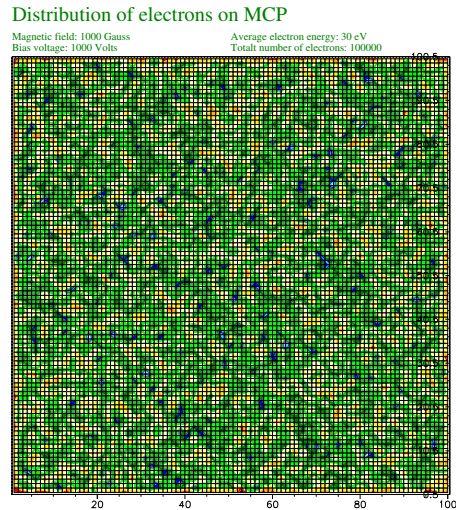


# Design, Simulation and Testing of a 2D Electron Source Based Calibrating System for a Proton Beam Ionisation Profile Monitor



Helge H. Refsum

July 15, 2004



Beam Diagnostics & Instrumentation  
Accelerators & Beams Department  
European Organization for Nuclear Research

in collaboration with



Department of Physics  
Faculty of Natural Sciences and Technology  
Norwegian University of Science and Technology



# Preface

The work presented here is my diploma thesis for the Master/Siv.ing.-degree at NTNU. The work was carried out at CERN, and I would like to thank my supervisors here Bernd Dehning and Jan Koopman, as well as Anne Borg at NTNU for their excellent guidance. I would also like to thank Rob Veenhof for his invaluable help with programming my simulations in Garfield, Giuseppe Foffano for his design work, and Michel Sillanoli for preparing and assembling the experimental setup.

Because of difficulties with the production of some of the parts needed for the experimental setup, the experiments could not be done until a few days before the deadline of this thesis. The experiments indicated that some of the initial conditions used in the simulations were inaccurate, however, there was not enough time to redo all the simulations. New simulation were done only for the cases where the change in initial conditions were expected to give a significant different result. The results of these simulations, are given in Chapter 4, together with the experimental results.



Helge H. Refsum

Geneva, July 15, 2004.



# List of Abbreviations

EGA	Electron Generator Array
EGP	Electron Generator Plate
IPM	Ionisation Profile Monitor
LHC	Large Hadron Collider
M3DFS	Maxwell 3D Field Simulator
MCP	Micro Channel Plate
SPS	Super Proton Synchrotron



# Useful Information

The following is taken from D. J. Griffiths, *Introduction to Electrodynamics*, Prentice-Hall, Inc., 3rd ed., 1999 and J. Lilley, *Nuclear Physics - Principles and Applications*, John Wiley & sons, Inc., 2001.

## Physical constants

$\epsilon_0 = 8.85 \times 10^{-12} \text{ C}^2/\text{Nm}^2$	Permittivity of free space
$\mu_0 = 4\pi \times 10^{-7} \text{ N/A}^2$	Permeability of free space
$c = 3.00 \times 10^8 \text{ m/s}$	Speed of light
$q = 1.60 \times 10^{-19} \text{ C}$	Elementary charge
$m = 9.11 \times 10^{-31} \text{ kg}$	Mass of the electron
$h = 6.63 \times 10^{-34} \text{ Js}$	Planck's constant
$k = 1.38 \times 10^{-23} \text{ J/K}$ $= 8.62 \times 10^{-5} \text{ eV/K}$	Boltzmann constant

## Conversion factors

$$1 \text{ eV} = 1.60 \times 10^{-19} \text{ J}$$
$$1 \text{ J} = 6.24 \times 10^{18} \text{ eV}$$

## Mathematical notation

$a, A$	Scalar quantity
$\mathbf{b}, \mathbf{B}$	Vector quantity
$\hat{\mathbf{c}}, \hat{\mathbf{C}}$	Unit vector



# Abstract

In this thesis the design of a calibration system, that measures the gain of the imaging system in the IPM, is discussed. Such a system is needed, as measurements have shown that the gain of the imaging system changes over time, in a non-homogenous way [1, 2]. This ageing effect is caused by changes in the MCP channel wall secondary emission coefficient, due to electron scrubbing. The MCP is only capable of emitting a limited number of electrons during its lifetime, and after a large number of electrons have been emitted, the gain is gradually reduced [3].

To measure this ageing effect, and to be able to compensate for it, a remote controlled, built-in calibration system was developed. Two sources were considered as electron emitters for the calibration, a heated wire grid and an EGP from Burle, Inc. [4] Previous test [2], and simulations presented in this thesis, showed that the wire grid would not produce an electron intensity at the MCP which was homogenous enough to be used for calibration purposes.

Promising results were obtained from simulations and experiments with the EGP. However, without a magnetic field available in the experimental setup, no final conclusions about the accuracy of the proposed calibration system can be given. The results of the simulations for low magnetic fields, coincide with what was found in the experimental data. However, to obtain an electron distribution which can be used for calibration purposes, a magnetic field of 1000 Gauss or more is recommended. This suggests that further test should be conducted in a setup with a magnetic field available. This will reveal if the system, as predicted by the simulations for high magnetic fields, can be used for calibration purposes.

Both simulations and experiments indicate that the proposed calibration system should not deteriorate the performance of the IPM during beam profile measurements. Simulations showed that the homogeneity of the electric field in operation mode will in fact improve with the calibration system implemented, compared to the original design. This should eventually be verified during actual beam profile measurements.



# Contents

<b>1</b>	<b>Introduction</b>	<b>1</b>
1.1	The IPM operating principle . . . . .	3
1.2	A new calibration system . . . . .	7
<b>2</b>	<b>Theory</b>	<b>11</b>
2.1	Computing the electromagnetic field . . . . .	11
2.1.1	Maxwell's equations . . . . .	12
2.1.2	Field contribution from charged particles . . . . .	13
2.2	Electron motion . . . . .	13
2.2.1	Electron trajectory with no magnetic field . . . . .	15
2.2.2	Electron trajectory with magnetic field . . . . .	16
2.3	MCP and EGP operating principle . . . . .	22
2.4	Electron emission . . . . .	24
2.4.1	Emission from heated metal wires . . . . .	24
2.4.2	Emission from EGP . . . . .	25
2.4.3	Resulting intensity at the MCP . . . . .	28
<b>3</b>	<b>Simulations</b>	<b>31</b>
3.1	Electrostatic field simulations . . . . .	32
3.1.1	The finite element method . . . . .	32
3.2	Electron path simulations . . . . .	35
3.2.1	The magnetic field . . . . .	37
3.2.2	Resolution . . . . .	37
3.3	Results of the simulations . . . . .	39
3.3.1	The original IPM . . . . .	39
3.3.2	IPM with wire grid emitter . . . . .	42
3.3.3	IPM with EGP . . . . .	51
3.3.4	The new design in operation mode . . . . .	60
<b>4</b>	<b>Experiments</b>	<b>63</b>
4.1	Setup . . . . .	63
4.2	Results . . . . .	66

<b>5</b>	<b>Discussion</b>	<b>75</b>
<b>6</b>	<b>Conclusion</b>	<b>83</b>
	<b>Bibliography</b>	<b>87</b>
<b>A</b>	<b>Garfield source code</b>	<b>89</b>
A.1	Electron drift from EGP . . . . .	89
A.2	Electron drift from wires . . . . .	99
A.3	Electron drift considering bias angle . . . . .	100
<b>B</b>	<b>Technical Drawings</b>	<b>101</b>

# Chapter 1

## Introduction

A *residual gas Ionisation beam Profile Monitor* (IPM) is one of the instruments under development in the *Super Proton Synchrotron* (SPS), and to be implemented in the *Large Hadron Collider* (LHC), for measuring the transverse beam size of the particle beam. The SPS has been in operation since 1976, and delivers protons and lead ions with momentum of up to 450 GeV/c. The extracted beam from the SPS is used in fixed target experiments, such as the COMPASS project where the goal is the study of hadron structure and hadron spectroscopy with high intensity muon and hadron beams [5].

The SPS will also be used as injector for the LHC, which is currently under construction. The LHC is scheduled to be operational in 2007, and will generate a beam of up to 7 TeV/c. The LHC will be the world's largest particle accelerator, situated approximately 100 m underground and with a circumference of 27 km. In the LHC head-on collisions of two beams of particles will be studied at energies previously unobtainable. Several different experiments are planned, common to them all is that their goal is to reveal secrets of the universe which cannot be disclosed with particle energies available today.

A sketch of the particle accelerators at CERN is shown in Fig. 1.1. The smaller accelerators serve as injectors for the larger ones.

The capability to measure beam profiles continuously in an accelerator, or storage ring, is important in order to confirm the normal damping of the betatron oscillations, to determine the onset and magnitude of normal and abnormal beam growths, and to infer the emittance of the beam.

Transverse beam profiles can be obtained by collecting the products of residual gas ionisation occurring when an incident particle beam passes through the imperfect vacuum in the monitor. At any given energy, the number of liberated ions and electrons in a given volume of residual gas is proportional to the density distribution of the incident particle beam so that the liberated ions and electrons contain beam profile information. The liberated electrons and ions can be collected with little disturbance to the incident beam; hence, continuous real time, nondestructive profile measurements are achievable [6].

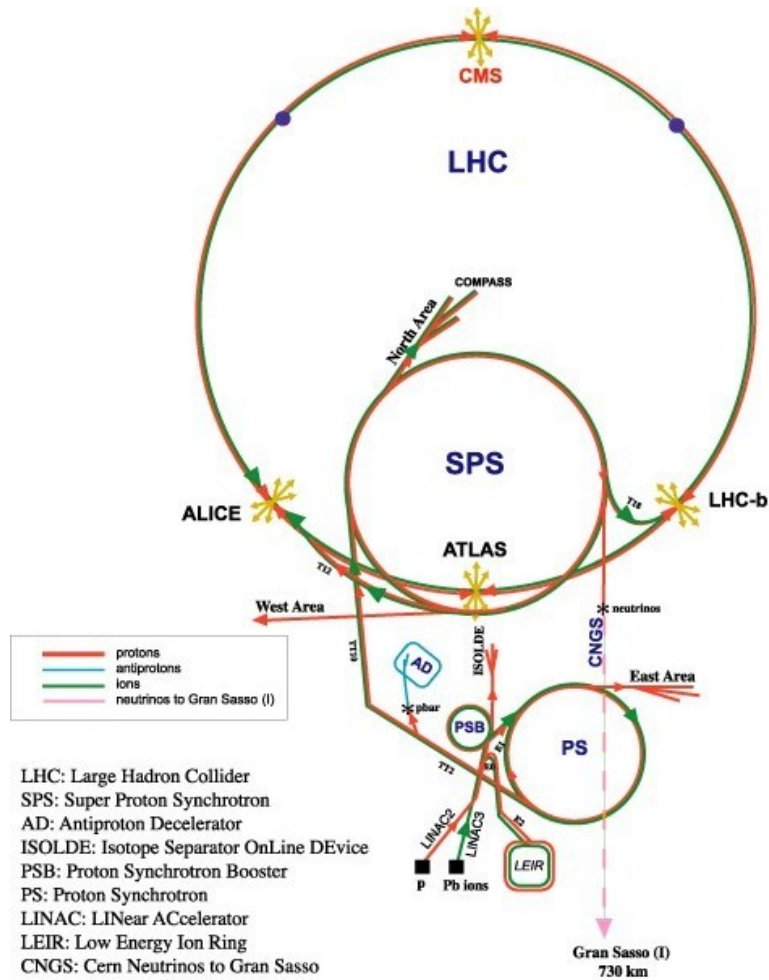
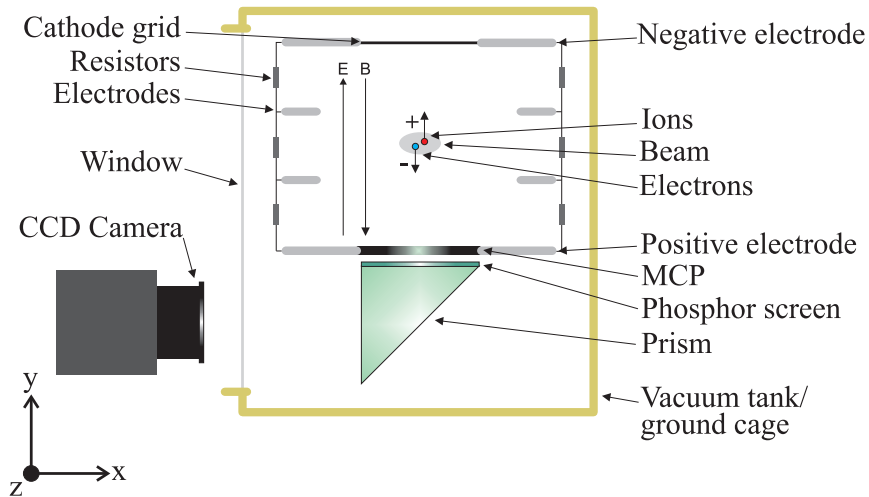


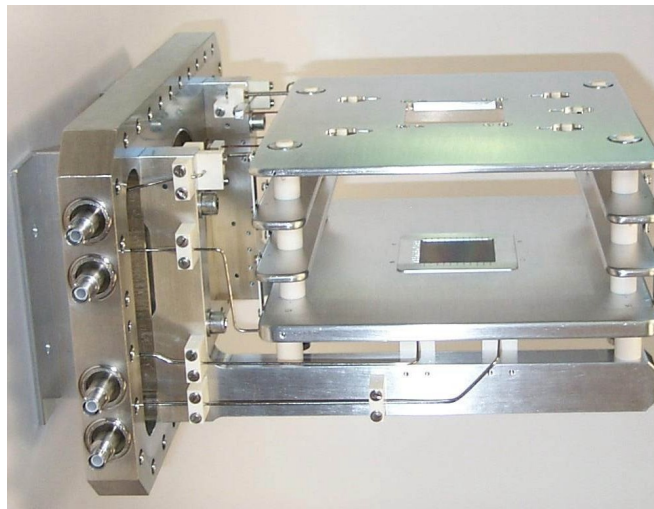
Figure 1.1: *CERN accelerators (not to scale). The smaller accelerator serve as injectors for the larger ones. The momentum of the particles which will be reach with the LHC is  $7 \text{ TeV}/c$ . Illustration from CERN web page [5].*

Today, IPMs are used in several high energy accelerators in order to monitor the beam profile [6, 7, 8]. An IPM from DESY, Hamburg, was installed in the SPS in 1997. Since then, the design of the IPM has been changed in several ways to improve the performance [9]. The IPM currently deployed in the SPS will be described in the next section.

## 1.1 The IPM operating principle



(a) Schematic operating principle.



(b) The inner part currently in use.

Figure 1.2: The IPM currently installed in the SPS. Photo courtesy of J. Koopman [1].

A sketch of the operating principle, as well as a photo, of the IPM used in the SPS today, is shown in Fig. 1.2. A detailed technical drawing is given in Appendix B. As mentioned in the previous section, the operating principle of the IPM is based on the ionisation of rest gas atoms and molecules by the passing beam due to the imperfect vacuum. In Fig. 1.2 the beam is passing in the  $z$ -direction, into the paper. Ions and electrons are liberated, and drift up or down

respectively, due to the applied electric field. The electric field is created by applying high voltage to the electrodes at the top and bottom of the chamber. The voltages applied are typically -1 to -2 kV for the upper electrode (cathode), and +1 to +2 kV for the lower electrode (anode). Consequently the direction of the electric field is in the +y-direction. The distance between the cathode and anode is 84 mm.

The lateral electrodes of the IPM, connected through resistors, are included to increase the homogeneity of the electric field. A homogenous field is necessary in order to preserve the spatial distribution of the ions and electrons as they drift through the chamber. A non-homogenous field would change these distributions, and result in beam profile measurements with an unacceptable large systematic error.

The function of the cathode grid is to prevent secondary electrons, created when ions hit the ground cage, from returning into the main chamber of the IPM. If the secondary electrons were allowed to return into the main chamber and mix with the primary electrons created by the beam, the electron distribution in space would no longer represent the true beam profile.

The electron distribution in space, reflecting the transverse density distribution of the particle beam, is forced down to the anode by the applied electric field. A *Micro Channel Plate* (MCP) measuring 5.08 cm by 5.08 cm is situated at the anode, and this is used to image the distribution. The function of the MCP is to amplify the electrical current from the incoming electron distribution. The amplified electron distribution then hits a phosphor screen. The phosphor screen converts the electron distribution into a photon distribution, which is viewed by a CCD camera, via a prism. This conversion allows the CCD camera to be situated outside the vacuum tank, making modifications to the imaging system simpler. Using a prism instead of a mirror, allows the phosphor layer to be deposited directly on the surface of the prism, reducing the need for alignment of the optical system.

In the IPMs used at CERN, in contrary to IPM system often used by others, the liberated electrons, and not the ions, are used to image the beam profile. Since the electrons have a much smaller mass than the ions, they are more sensitive to transverse deviation due to the space charge created by the circulating beam. In other words, the electron distribution diverges more easily than the ion distribution during its drift to the analysing device. To counteract this phenomenon, a magnetic field of up to 2000 Gauss is added in addition to the electric field. The direction of the magnetic field is in the -y-direction, as indicated in Fig. 1.2 (a).

The magnetic field, together with the initial velocity, cause the electrons to spiral at a small radius, while the electric field forces them down towards the anode. Utilising the electrons in this way instead of the ions to image the beam, results in better resolution for the measurements of the beam distribution [9]. This is mainly caused by the fact that the time the electrons use to travel from

## 1.1. THE IPM OPERATING PRINCIPLE

---

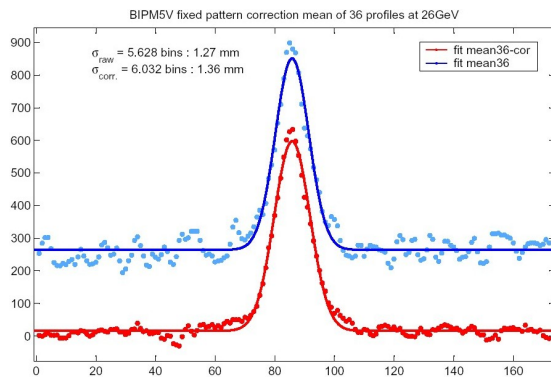
the beam to the analysing device, is much shorter than the time used for the ions. Consequently, the field of the beam affects the distribution less for electrons than for ions if suitable electric and magnetic fields are applied.

To give the reader an idea of what the IPM installation in the SPS tunnel looks like, a picture taken in access point BA5 is shown in Fig. 1.3. The IPM is situated inside the centre orange magnet. The magnets on each side are placed there to compensate for the bending of the beam caused by centre magnet.

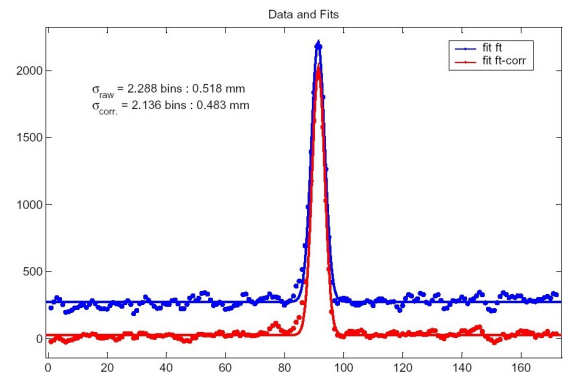


Figure 1.3: *One of the IPMs location in the SPS tunnel. The IPM is situated inside the centre orange magnet. Photo courtesy of J. Koopman [1].*

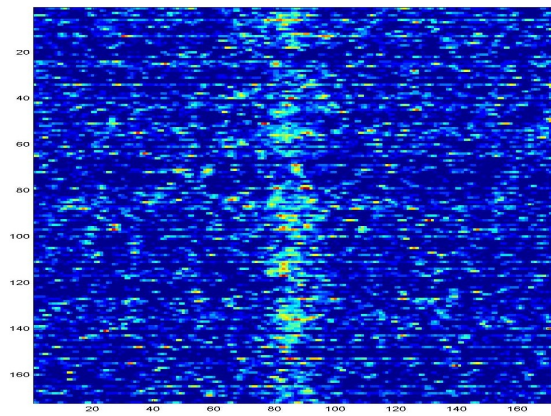
Typical observations made with the IPM during 2003 are shown in Fig. 1.4. Although results were promising, a new phenomenon was encountered with the IPMs after some time of operation. The gain of the MCPs was found to change with time, and the gain was reduced more in certain areas than others. This effect will be discussed in the next section.



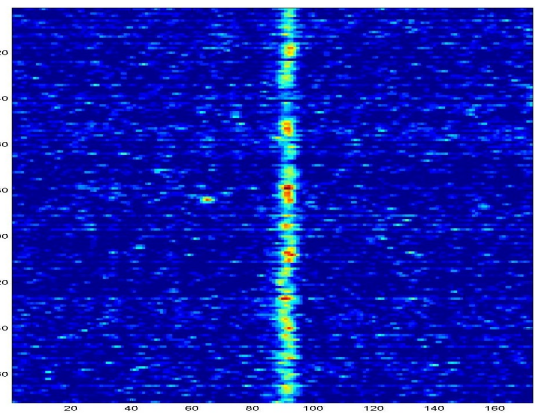
(a) 26 GeV Pilot bunch.



(b) 450 GeV Pilot bunch.



(c) 26 GeV Pilot bunch.



(d) 450 GeV Pilot bunch.

Figure 1.4: Data obtained from the IPM in 2003 [1].

## 1.2 A new calibration system

One of the difficulties encountered with the current IPMs, is the too rapid and non homogenous ageing of the MCPs. The ageing mainly affects the area of the MCP where the beam is imaged, causing a local decrease in the gain of the MCP. The reduction of the gain is caused by changes in the channel wall secondary emission coefficient due to electron scrubbing. The MCP is only capable of emitting a limited number of electrons during its lifetime, after a large number of electrons have been emitted, the gain is gradually reduced [3].

Because the MCP images the beam more or less in the same position throughout its lifetime, the gain is reduced more in the centre of the MCP than at the edges. With time, this causes distortion to the images created of the beam. A sketch of the problem is shown in Fig. 1.5.

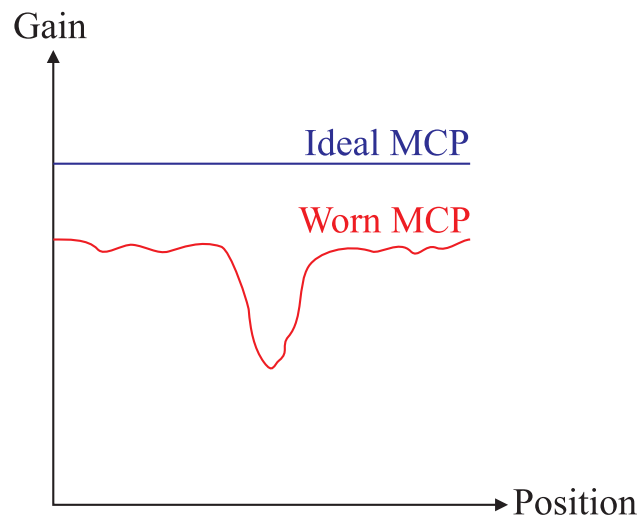


Figure 1.5: A sketch of the problems caused by uneven wearing of the MCP. The dip in the centre is caused by extensive imaging of the beam in the same position.

In the LHC the IPM is intended as a continuous beam observation device. The ageing of the MCPs is therefore an important issue, as regularly replacement of the MCPs is both difficult and costly, and would have to be done during machine shutdown.

To measure the ageing effect, and to be able to compensate for it, a remote controlled, built-in calibration system is to be developed. One method that has been proposed, is installing a grid of heating wires acting as an electron source above the cathode grid in the IPM [2]. The idea is to use this electron source to measure the gain of the MCP as a function of position, in periods where the IPM is not in normal operation. The measured variations in the gain can then be

used to improve the images acquired during operation of the IPM. The operating principle of a calibration system based on a heated wire grid is sketched in Fig. 1.6.

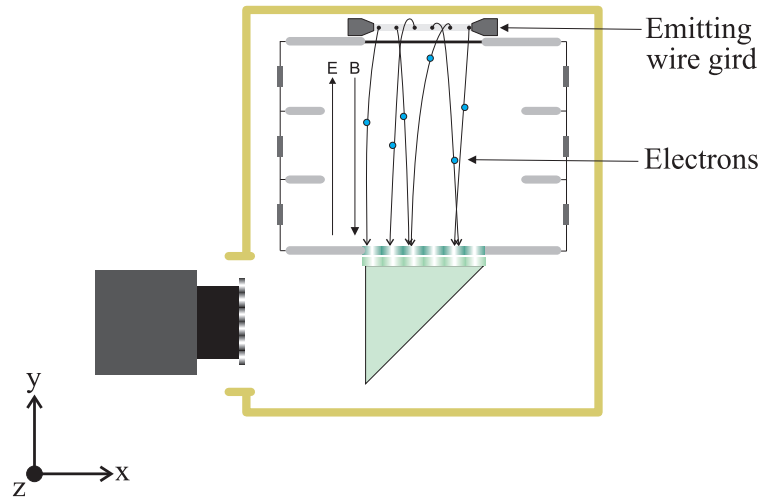


Figure 1.6: *The operating principle of a calibration system based on a wire grid emitting electrons. The paths of some electrons are indicated, illustrating the difficulties of obtaining a homogenous distribution at the MCP.*

The electron source must however be constructed to produce an electron field as homogenous as possible. This may be difficult using only a heated grid, as the wires act as point (or in fact line) sources, and the spread of the electrons during their drift through the chamber is small. The implementation of an *Electron Generator Plate* (EGP) as the electron source is therefore proposed. EGPs produced by Burle, Inc. [4] are specified to emitting homogenous fields of electrons covering the complete area of the MCPs used in the IPM [10, 11]. A sketch of a calibration system using an EGP as the electron source is shown in Fig. 1.7. A calibration system based on this principle is at the current time being developed for the RHIC and SNS accelerator in Oak Ridge, Tennessee. [12, 13]. A similar system is also planned for the Tevatron accelerator at Fermilab in Batavia, Illinois [14].<sup>1</sup>

The goal of this thesis is to design a calibration system that accurately measures the gain of the imaging system, where the MCP is expected to be the main source of error. The measured variations in the gain as a function of position obtained during calibration, will be used to improve the imaging of the beam during operation of the IPM. The changes made to the IPM to be able to implement the calibration system, must not decrease the performance of the IPM during operation.

<sup>1</sup>It is purely by chance that this is done by several people at the same time, the ideas for the calibration system has been developed individually, in parallel.

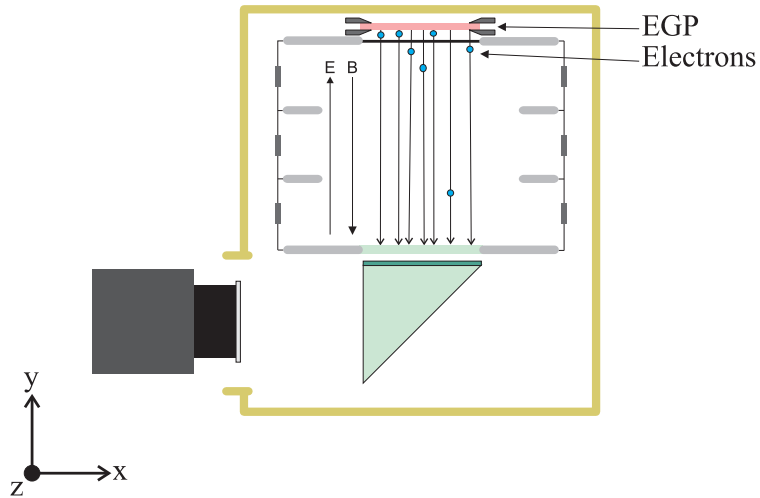


Figure 1.7: A calibration system for the IPM using an EGP as electron source. The EGP is specified to produce a homogenous field of electrons, allowing more accurate measurements of the gain of the MCP. Some electron paths are sketched to illustrate the working principle.

In order to reach this goal, detailed simulations of the electric field in the IPM will be presented, as well as simulations of the path of electrons drifting through the IPM under different conditions. An optimal design for the calibration system will be suggested, together with values for applied electric and magnetic field strengths.

To understand the physics behind this system, the operating principle of MCPs and EGPs will be reviewed in Chapter 2, along with some basic theory of electrodynamics. Detailed simulations of the electric fields present in the IPM, as well as simulations of electrons drifting from different sources, are given in Chapter 3. The experiments carried out are described in Chapter 4. Some new simulations, taking experimental values into account, are also presented in this chapter. The results are then compared with the simulations and theory in Chapter 5. As reference, the source code developed for the simulations and some technical drawings are given in Appendix A and B.



# Chapter 2

## Theory

In this chapter, basic theory required to understand the operating principle of the IPM and the future calibration system in more detail, will be reviewed. The first part of this chapter will briefly review the basics of electromagnetic theory, in order to understand how the programs used for the simulations work. An analytical description of how the initial energy of an emitted electron affects its path from emission to the analysing device, will also be given.

Further, a short description of the operating principle of MCPs and EGPs will be given. In the last sections of this chapter, some models for the electron emission from different sources, and how the emission affects the intensity of electrons at the MCP, will be described. These models will be used as initial conditions for the simulations described in the following chapter.

### 2.1 Computing the electromagnetic field

In order to describe the movement of electrons in an electromagnetic field, the first thing needed is a description of the field itself. D. Griffiths deals with this topic in his book *Introduction to electrodynamics*, 3rd Ed., 1999 [15]. The following sections are based on this book.

### 2.1.1 Maxwell's equations

The theory of classical electrodynamics can be summarised with Maxwell's equations [15]

$$\nabla \cdot \mathbf{E} = \frac{1}{\epsilon_0} \rho \quad (\text{Gauss's law}), \quad (2.1)$$

$$\nabla \cdot \mathbf{B} = 0 \quad (\text{no name}), \quad (2.2)$$

$$\nabla \times \mathbf{E} = -\frac{\partial \mathbf{B}}{\partial t} \quad (\text{Faraday's law}), \quad (2.3)$$

$$\nabla \times \mathbf{B} = \mu_0 \mathbf{J} + \mu_0 \epsilon_0 \frac{\partial \mathbf{E}}{\partial t} \quad (\text{Ampère's law with Maxwell's correction}). \quad (2.4)$$

$\mathbf{E}$  and  $\mathbf{B}$  denote the electric and magnetic field respectively.  $\epsilon_0$  and  $\mu_0$  are the permittivity and permeability of free space, while  $\rho$  is the charge density and  $\mathbf{J}$  is the current density.

In matter, in terms of free charges  $\rho_f$  and free currents  $\mathbf{J}_f$ , Maxwell's equations become

$$\nabla \cdot \mathbf{D} = \rho_f, \quad (2.5)$$

$$\nabla \cdot \mathbf{B} = 0, \quad (2.6)$$

$$\nabla \times \mathbf{E} = -\frac{\partial \mathbf{B}}{\partial t}, \quad (2.7)$$

$$\nabla \times \mathbf{H} = \mathbf{J}_f + \frac{\partial \mathbf{D}}{\partial t}. \quad (2.8)$$

The electric displacement  $\mathbf{D}$  is defined by

$$\mathbf{D} \equiv \epsilon_0 \mathbf{E} + \mathbf{P}, \quad (2.9)$$

where  $\mathbf{P}$  is the dipole moment per unit volume. The auxiliary field  $\mathbf{H}$  is defined by

$$\mathbf{H} \equiv \frac{1}{\mu_0} \mathbf{B} - \mathbf{M}, \quad (2.10)$$

where  $\mathbf{M}$  is the magnetic dipole moment per unit volume. For linear media, the relations between  $\mathbf{E}$  and  $\mathbf{D}$ , and between  $\mathbf{B}$  and  $\mathbf{H}$ , are given by

$$\mathbf{D} = \epsilon \mathbf{E} \quad (2.11)$$

$$\mathbf{H} = \frac{1}{\mu} \mathbf{B}, \quad (2.12)$$

where  $\epsilon$  and  $\mu$  are the permittivity and permeability of the media.

If there are charges in the volume, such as ions or electrons, their contribution to the field may also have to be considered.

### 2.1.2 Field contribution from charged particles

The electric field  $\mathbf{E}$  at position  $\mathbf{r}$  due to  $n$  point charges  $q_1, q_2, \dots, q_n$ , each at a distance  $r_1, r_2, \dots, r_n$ , is given by [15]

$$\mathbf{E}(\mathbf{r}) \equiv \frac{1}{4\pi\epsilon_0} \sum_{i=1}^n \frac{q_i}{r_i^2} \hat{\mathbf{r}}_i, \quad (2.13)$$

for a discrete charge distribution. For a continuous charge distribution, the corresponding expression is

$$\mathbf{E}(\mathbf{r}) = \frac{1}{4\pi\epsilon_0} \int_{\mathbb{V}} \frac{\rho(\mathbf{r}')}{r^2} \hat{\mathbf{r}} d\tau, \quad (2.14)$$

where  $\rho$  is the charge per volume,  $\tau$  an element of volume, and the expression is integrated over the volume  $\mathbb{V}$ .

When the electric and magnetic field is known, the motion of charged particles can be computed.

## 2.2 Electron motion

The force  $\mathbf{F}$  acting on a particle with charge  $q$ , moving at velocity  $\mathbf{u}$  in an electric field  $\mathbf{E}$ , and magnetic field  $\mathbf{B}$ , is given by the Lorentz force law [15]

$$\mathbf{F} = q(\mathbf{E} + \mathbf{u} \times \mathbf{B}). \quad (2.15)$$

The equation of motion can be derived from Newton's second law and the Lorentz force law, applying the relativistic expression for the momentum. Velocity is defined as

$$\mathbf{u} = \frac{d\mathbf{r}}{dt}, \quad (2.16)$$

where  $\mathbf{r}$  is the position vector and  $t$  is time. The acceleration is then

$$\mathbf{a} = \frac{d\mathbf{u}}{dt}. \quad (2.17)$$

The relativistic momentum is

$$\mathbf{p} = \gamma m \mathbf{u}, \quad (2.18)$$

where  $m$  is the rest mass and  $\gamma$  is defined as

$$\gamma = \frac{1}{\sqrt{1 - \frac{u^2}{c^2}}}, \quad (2.19)$$

where  $c$  is the speed of light. Newton's second law yields

$$\mathbf{F} = \frac{d\mathbf{p}}{dt}. \quad (2.20)$$

Substituting Eq. 2.18 into Eq. 2.20 gives

$$\mathbf{F} = m\left(\frac{d\gamma}{dt}\mathbf{u} + \gamma\frac{d\mathbf{u}}{dt}\right) \quad (2.21)$$

$$= m\left(\left(1 - \frac{u^2}{c^2}\right)^{-\frac{3}{2}}\frac{\mathbf{u}}{c^2}\mathbf{u} \cdot \frac{d\mathbf{u}}{dt} + \gamma\frac{d\mathbf{u}}{dt}\right) \quad (2.22)$$

$$= m\gamma\left(\mathbf{a} + \frac{\mathbf{u}(\mathbf{u} \cdot \mathbf{a})}{c^2 - u^2}\right) \quad (2.23)$$

Combining Eq. 2.23 and Eq. 2.15 gives

$$\frac{q}{m}\gamma^{-1}(\mathbf{E} + \mathbf{u} \times \mathbf{B}) = \mathbf{a} + \frac{\mathbf{u}(\mathbf{u} \cdot \mathbf{a})}{c^2 - u^2}. \quad (2.24)$$

An expression for  $\mathbf{u} \cdot \mathbf{a}$  is obtained by taking the scalar product between  $\mathbf{u}$  and Eq. 2.24

$$\frac{q}{m}\gamma^{-1}(\mathbf{u} \cdot \mathbf{E} + \mathbf{u} \cdot (\mathbf{u} \times \mathbf{B})) = \mathbf{u} \cdot \mathbf{a} + \frac{u^2}{c^2 - u^2}(\mathbf{u} \cdot \mathbf{a}). \quad (2.25)$$

Now  $\mathbf{u} \cdot (\mathbf{u} \times \mathbf{B}) = \mathbf{B} \cdot (\mathbf{u} \times \mathbf{u}) = 0$ , hence

$$\mathbf{u} \cdot \mathbf{a} = \frac{q}{m}\gamma^{-3}(\mathbf{u} \cdot \mathbf{E}). \quad (2.26)$$

Inserting this into Eq. 2.24, the expression for the acceleration becomes

$$\mathbf{a} = \frac{q}{m}\gamma^{-1}\left(\mathbf{E} + \mathbf{u} \times \mathbf{B} - \frac{1}{c^2}\mathbf{u}(\mathbf{u} \cdot \mathbf{E})\right). \quad (2.27)$$

The first term of this equation shows that the electric field will accelerate the electron in the direction of the field. The second term shows that the magnetic field will accelerate the electron perpendicular to both the electron velocity and the magnetic field. The last term is a relativistic term, which will normally be small compared to the two first, and act in direction opposite of the electron velocity. In the non-relativistic case the expression for the acceleration simplifies to

$$\mathbf{a} = \frac{q}{m}(\mathbf{E} + \mathbf{u} \times \mathbf{B}). \quad (2.28)$$

It is obvious that the motion of an electron in an electromagnetic field, is dependent upon the initial velocity of the electron, in other words the initial

kinetic energy of the electron. The relation between the kinetic energy  $U$  and velocity  $u$  of a particle is given by [15]

$$U \equiv U_{tot} - mc^2 = mc^2 \left( \frac{1}{\sqrt{1 - \frac{u^2}{c^2}}} - 1 \right) = mc^2(\gamma - 1), \quad (2.29)$$

which simplifies to the well known

$$U = \frac{1}{2}mu^2 \quad (2.30)$$

in the non-relativistic case. If electron Volts (eV) is used as unit for the energy, while the mass and velocity still are expressed in SI-units, the relationship becomes

$$U = \frac{mu^2}{2q}, \quad (2.31)$$

where  $q$  is the elementary charge. Throughout this thesis, eV will be used as energy unit.

### 2.2.1 Electron trajectory with no magnetic field

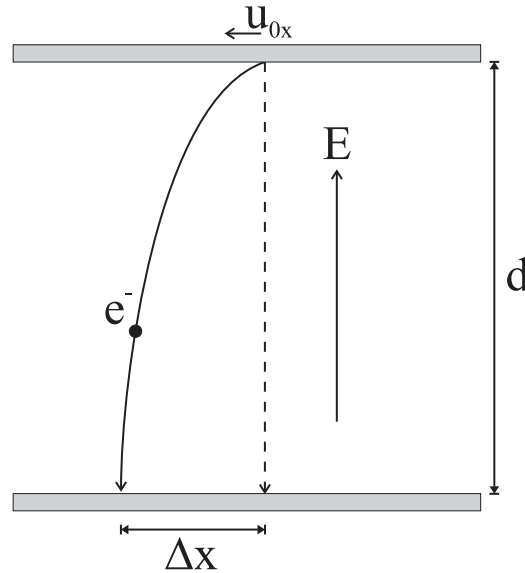


Figure 2.1: *The trajectory of an electron with initial velocity  $u_{0x}$  under the influence of an electric field, but with no magnetic field present.*

Figure 2.1 shows the parabolic motion of an electron in an electric field, without any magnetic field present. Assume for now that the electron has initial velocity only in the x-direction, that is  $u_{0y} = u_{0z} = 0 \neq u_{0x}$ . If the electric field  $E$  is homogenous and in the y-direction, the drift time  $t_d$  between the two infinite electrodes separated by a distance  $d$  will be given as [6, 16]

$$t_d = \sqrt{\frac{2d}{a}} = \sqrt{\frac{2dm}{qE}} = d\sqrt{\frac{2m}{q\Phi}}, \quad (2.32)$$

where  $\Phi$  is the potential difference between the electrodes. The drift of the electron in the x-direction  $\Delta x$  will then be

$$\Delta x = u_{0x}t_d. \quad (2.33)$$

Using Eq. 2.31 to substitute for the velocity and Eq. 2.32, the expression for the drift time becomes

$$\Delta x = \sqrt{\frac{2qU_x}{m}} \cdot d\sqrt{\frac{2m}{q\Phi}} = 2d\sqrt{\frac{U_x}{\Phi}}, \quad (2.34)$$

where  $U_x$  is the initial electron energy in the x-direction given in eV. Consequently, electrons with different  $U_x$  will arrive at different locations in the image plane when no magnetic field is applied. What happens when a magnetic field is applied, will be discussed in the next section.

### 2.2.2 Electron trajectory with magnetic field

Now, if a magnetic field is added in addition to the electric field, the motion of an electron will be a helix, as shown in Fig. 2.2. The radius  $R$  of the helix will be determined by the component of the velocity perpendicular to the magnetic field,  $u_{0x}$ . The radius can be computed using the relativistic cyclotron formula [15]

$$quB = p\frac{u}{R}. \quad (2.35)$$

The left-hand side of the equation is the magnetic component from the Lorentz force law, Eq. 2.15, where  $u$  now is the component of the velocity perpendicular to the magnetic field  $B$ . The right-hand side is the relativistic expression for the centripetal acceleration, where  $p$  is the component of relativistic momentum of the electron given by Eq. 2.18. Rearranging Eq. 2.35 yields an expression for the cyclotron radius

$$R = \frac{p}{qB} \quad (2.36)$$

$$R = \frac{\gamma mu}{qB}. \quad (2.37)$$

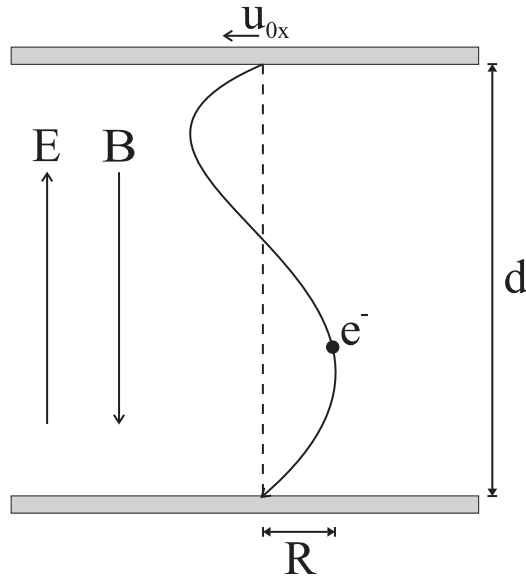


Figure 2.2: The trajectory of an electron with initial velocity  $u_{0x}$  under the influence of a magnetic, as well as an electric, field.

For the non-relativistic case, this simplifies to

$$R = \frac{mu}{qB}. \quad (2.38)$$

The period  $t_l$  of one complete revolution (the Larmor period) can be computed from [6]

$$t_l = \frac{2\pi R}{u}, \quad (2.39)$$

using Eq. 2.38 to substitute for  $u$  and  $R$  to obtain

$$t_l = \frac{2\pi m}{qB} = \frac{3.57 \cdot 10^{-7} \text{s} \cdot \text{Gauss}}{B}. \quad (2.40)$$

Note that the Larmor period is independent of the velocity of the electron.

If the magnetic field  $B$  is adjusted so that the drift time through the chamber is equal to one Larmor period (or an integral number thereof), that is  $t_l = t_d$ , the electrons will complete one revolution during their drift and preserve their initial position in the image plane. The following condition for the magnetic  $B_l$  field is then obtained

$$\frac{2\pi m}{qB_l} = d \sqrt{\frac{2m}{q\Phi}}, \quad (2.41)$$

$$B_l = \frac{\pi}{d} \sqrt{\frac{2m\Phi}{q}}. \quad (2.42)$$

A plot of the required magnetic field as a function of the potential is shown in Fig. 2.3.

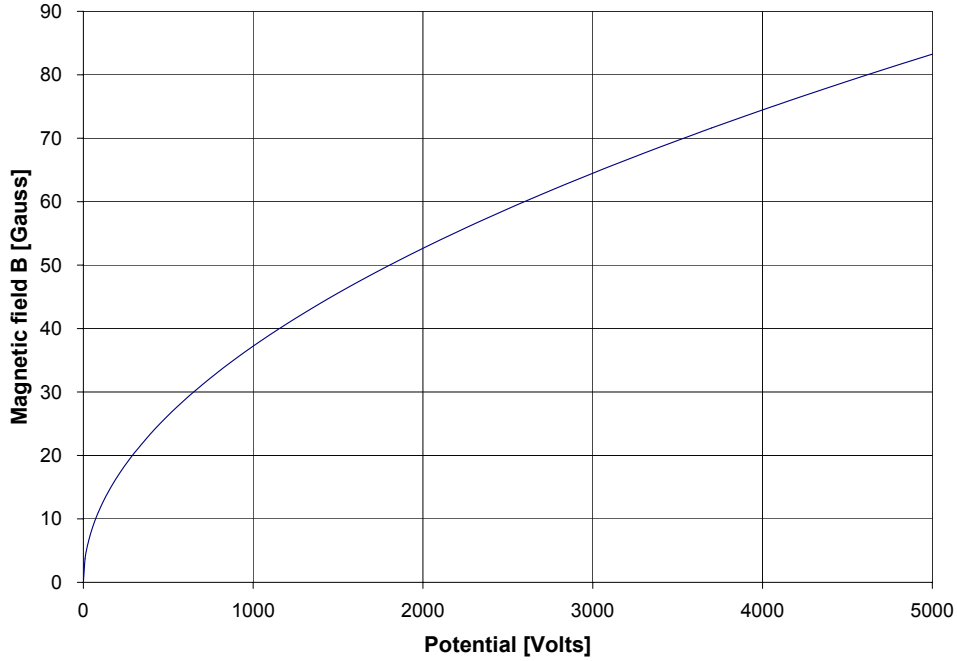


Figure 2.3: Required magnetic field for the electron to complete one revolution during its drift between two electrodes separated by distance  $d = 90$  mm.

If however the magnetic field is chosen to be half of that required for one complete revolution  $B = \frac{1}{2}B_l$ , a maximum offset of the electrons in the imaging plane will occur. This can be used to find the optimal magnetic field strength experimentally. By emitting electrons for example from a wire and varying the magnetic field, the narrowest pattern will be found at  $B = B_l$ , and the widest pattern at  $B = \frac{1}{2}B_l$ .

In reality, however, the electrons will also have a velocity component in the y-direction, parallel to the electric and magnetic fields. The general expression for the drift time then becomes [6]

$$t_g = \frac{md}{q\Phi} \cdot \left( -u_{0y} + \sqrt{2\frac{q}{m}\Phi + u_{0y}^2} \right), \quad (2.43)$$

or expressed as a function of energy in the y-direction  $U_y$  in eV

$$t_g = \frac{d}{\Phi} \sqrt{\frac{2m}{q}} \left( \sqrt{\Phi + U_y} - \sqrt{U_y} \right). \quad (2.44)$$

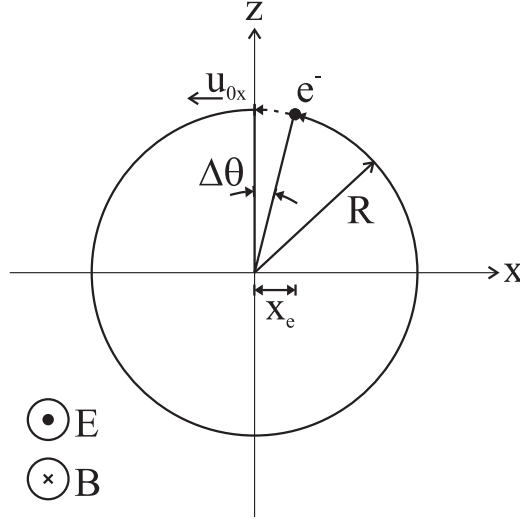


Figure 2.4: *The trajectory of an electron with velocity both in the y-direction (into the paper), and x-direction (perpendicular to the magnetic field), as seen from above. The direction of the electric field is out of the paper, and the magnetic field in to the paper.*

The difference in the drift time  $\Delta t = t_d - t_g$  will cause the electron to reach the imaging electrode before it has carried out a complete revolution, resulting in an offset  $x_e$  of the position in the image plane. As shown in Fig. 2.4, the offset in the x-direction  $x_e$  will be given by

$$x_e = R \sin(\Delta\theta) = R \sin\left(\frac{2\pi\Delta t}{t_d}\right), \quad (2.45)$$

where

$$\frac{\Delta t}{t_d} = \frac{t_d - t_g}{t_d} = 1 - \frac{t_g}{t_d}, \quad (2.46)$$

$$\frac{\Delta t}{t_d} = 1 + \sqrt{\frac{U_y}{\Phi}} - \sqrt{1 - \frac{U_y}{\Phi}}. \quad (2.47)$$

A plot of the relative offset in the x-direction  $x_e/R$ , as a function of the initial energy in the y-direction  $U_y$ , is given for a few different potentials  $\Phi$  in Fig. 2.5. As can be seen from the plots, variations in initial electron energy cause substantially offset in the imaging plane.

If large variations in the electron energy are expected, the best solution, if one seeks to prevent electron offset, is to add a magnetic field as strong as possible. The maximum possible offset will then be proportional to  $1/B$ , and given by twice the cyclotron radius in Eq. 2.36. The average offset will however be equal to the radius itself, as can be seen from Fig. 2.6.

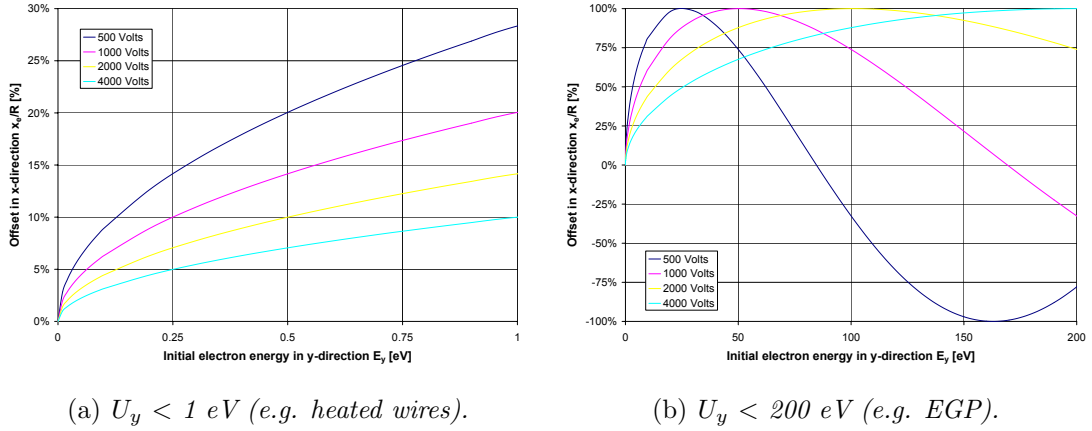


Figure 2.5: Relative offset in the  $x$ -direction  $x_e/R$  as a function of the initial energy in the  $y$ -direction  $U_y$ .

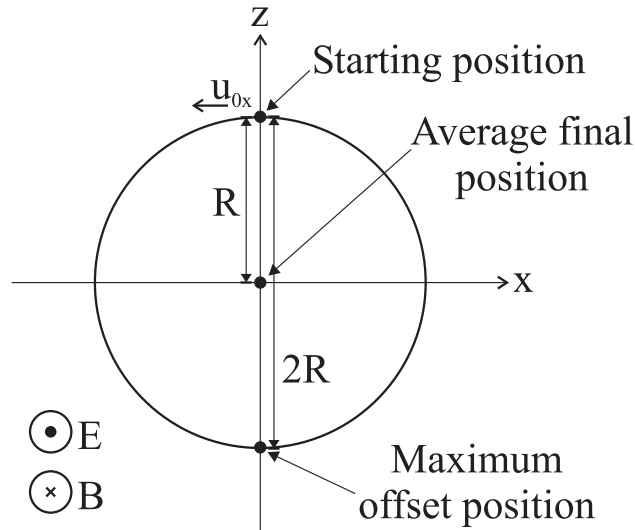


Figure 2.6: The final position of an emitted electron will always be somewhere along circumference. If the initial velocity  $u_{0x}$  varies substantially, there will be an equal probability of the final position being anywhere along this circumference. The resulting average final position, will therefore be at the centre, a distance  $R$  from the starting point. The maximum possible offset will be  $2R$ .

This concludes the description of how electrons move within electromagnetic fields. The next section will deal with what happens when the electrons reach the MCP situated at the anode of the IPM. In other words, a description of how the MCP works. As EGPs are based on the same technology as the MCPs, they

are described in a common section.

## 2.3 MCP and EGP operating principle

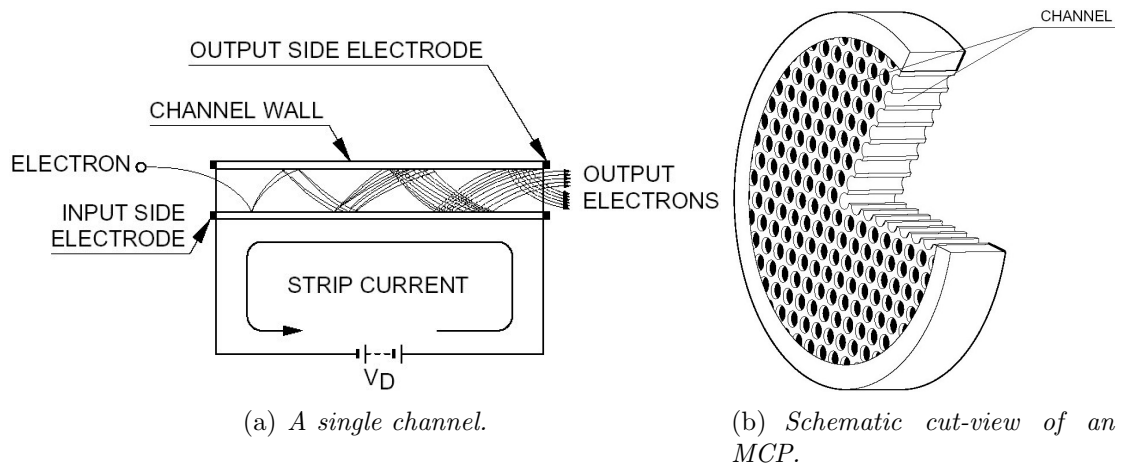


Figure 2.7: The operating principle of an MCP [1].

Figure 2.7 shows the working principle of a *Micro Channel Plate* (MCP). The MCP consists of several miniature electron multipliers, or *channels*, densely spaced and oriented parallel to each other. A voltage is applied across the channels, and when an incoming electron reaches a channel it initiates an avalanche of electrons in the channel. In this way, the distribution of the electrons reaching the MCP is amplified.

Typical channel diameters are 2-100  $\mu\text{m}$ , and the length to diameter ratio is generally between 40 and 100. The channels axes are usually normal to, or biased at a small angle to the MCP input surface. The bias angle is used to increase the chance of the incoming electrons hitting the channel walls and creating an avalanche, instead of just passing straight through. The resolution obtained by the MCP is limited only by the channel spacing.

The MCP is usually made from lead glass, treated to optimise secondary electron emission. Each face of the MCP is coated with a conducting metal layer, which serve as input and output electrodes. The gain of the MCP can be adjusted by varying the voltage applied to the electrodes. Normal operating voltage is up to 1000 V, and at this voltage the gain of a single MCP is typically  $10^4$ . A gain of more than  $10^8$  can be obtained by mounting up to three MCP in sequence. Time resolution is generally better than 100 ps [3, 17]. Some images of MCPs obtained by electron microscopy are shown in Fig. 2.8.

The operating principle of an *Electron Generator Plate* (EGP) is very similar to that of an MCP, except for the fact that no incoming electrons are needed. The glass matrix constituting the channels is made from a slightly different material, resulting in spontaneous electron emission when a voltage is applied

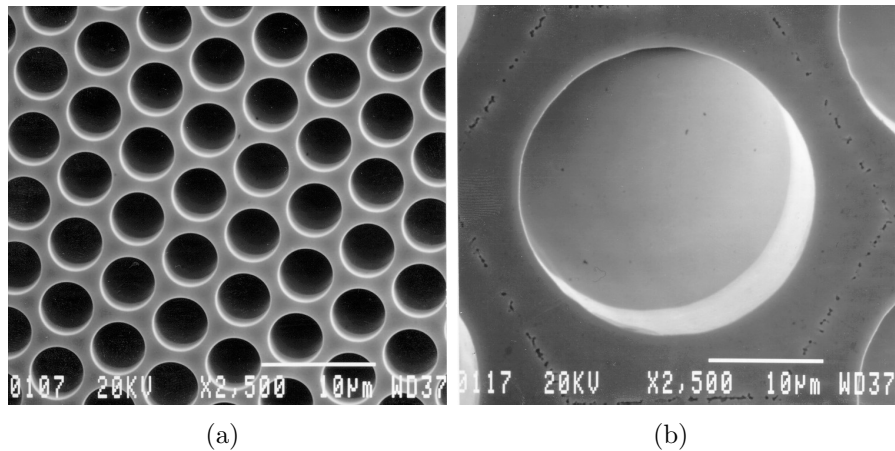


Figure 2.8: Images of MCPs obtained by electron microscopy. Images from Burle, Inc. [18]

to the electrodes. The EGPs in question are patented and produced by *Burle, Inc.* [4] They have not published any details on what type of materials that are used, nor do they wish to disclose any information about it at this time.

Even though the operating principle of the MCP and EGP are similar, the applications are completely different. The MCP is used to amplify a signal, while the EGP is used as a cold electron source. The electron emission from the EGP can be varied over a broad range by controlling the applied voltage. The typical operating voltage is up to 1000 V for a single EGP, resulting in an electron current claimed to be of about  $10^{-9}$  A/cm<sup>2</sup> with a uniformity of  $\pm 10\%$  across the active area. As with the MCPs, the EGPs can also be assembled in a stack configuration (Chevron, Z-Stack), called an *Electron Generator Array* (EGA), making emission rates of up to  $10^{-4}$  A/cm<sup>2</sup> possible [18, 10].

It is worth noting that a magnetic field might affect the performance of both the MCP and EGP. The efficiency might be reduced, but the performance is expected to still be satisfactory [3, 19]. However, Burle, Inc. has not conducted specific test on their MCPs or EGPs operating in magnetic fields. Another manufacturer of MCPs, Hamamatsu Photonics K.K., has done some measurements on their MCPs operating in magnetic fields up to 1000 Gauss [20]. Their results show that the effect is dependent upon both the magnitude and direction of the magnetic field with respect to the axis of the channels in the MCP. For magnetic fields parallel to the channels, as in the IPM, the efficiency is actually found to increase by up to 40%, rather than to decrease.

As input to the simulations, and to be able to predict the behaviour of the calibration system in more detail, not only the emission rate of the electron source is of interest, but also the energy distribution and the initial direction of

the electrons are important. In the next section, an attempt is made to describe these parameters for two different electron sources.

## 2.4 Electron emission

As shown in previous sections, knowledge of the initial energy of the electrons is important in order to predict their path through the IPM. The distribution of the energy of the electrons, both in magnitude and direction, should be known. In addition knowledge of the number of emitted electrons per second, the electron current, is needed.

The theoretical description of these figures differ for the two electron sources in question, and they are therefore treated separately.

### 2.4.1 Emission from heated metal wires

Running a current through metal wires will cause them to heat up, and thereby emit electrons. For electron emission from a heated metal surface at low fields (below  $10^8$  V/m), the theory of *thermionic emission* applies. For this regime the field that is applied to draw the electrons from the metal surface can be completely neglected. In this approximation, a step function with height  $W$ , the *work function*, can be used to describe the potential barrier between metal and vacuum. For thermionic emission, the energy distribution  $dI/dU$  (current as a function of energy) is [21]

$$dI/dU = p(U) = \frac{4\pi m^* q}{h^3} U e^{-\frac{U+W}{kT}}, \quad (2.48)$$

where  $m^*$  is the effective mass of an electron,  $h = 6.63 \times 10^{-34}$  Js is Planck's constant,  $k = 8.62 \times 10^{-5}$  eV/K is the Boltzmann constant,  $U$  is the energy and  $T$  is the temperature.

This distribution is equal to a *gamma distribution* [22]

$$p(x) = \frac{x^{\alpha-1}}{\Gamma(\alpha)\beta^\alpha} e^{-\frac{x}{\beta}}, \quad (2.49)$$

if the parameters  $\alpha = 2$  and  $\beta = kT$  are chosen. The random variable  $x$  then corresponds to the energy  $U$ , and the expression for the energy distribution can be written as

$$p(U) = \frac{4\pi m^* q}{h^3} U e^{-\frac{U+W}{kT}} = CU e^{-\frac{U}{\beta}}, \quad (2.50)$$

where  $C$  is a constant. This is the energy distribution which was used in the simulations.

Integrating the original distribution from Eq. 2.48 over all energies ( $0 < U < \infty$ ) yields the current density  $I$

$$I = \int_0^{\infty} p(U)dU = \frac{4\pi m^* q k^2}{h^3} T^2 e^{-\frac{W}{kT}} = AT^2 e^{-\frac{W}{kT}}, \quad (2.51)$$

where  $A$  is known as the Richardson constant. The Richardson constant  $A$  has the value  $60.2 \text{ A/cm}^2\text{K}^2$  for pure metals, but it can be several orders of magnitude higher for impure metals. The work function  $W$  is the energy required to liberate an electron from the metal. The value of  $W$  is typically in the range 2-5 eV. [23, 24]

The electron current per area emitted from the wires  $I_w$ , is related to the current per area recorded on the MCP  $I_{MCP}$  by

$$I_w = I_{MCP} \frac{A_{MCP}}{A_w}, \quad (2.52)$$

where  $A_{MCP}$  and  $A_w$  is the surface area of the MCP and wires, respectively. Equation 2.51 can now be used to estimate the temperature at which the wires should be heated. This equation is however highly dependent upon material constants, and this value should therefore be verified experimentally. Assuming a pure tungsten wire, it can be calculated that a temperature of about 1450 K would give an electron current of  $10^{-9} \text{ A/cm}^2$  at the MCP. [23].

The average energy of the emitted electrons can be found from the energy distribution given in Eq. 2.48

$$\langle U \rangle = \frac{\int_0^{\infty} U p(U) dU}{\int_0^{\infty} p(U) dU} = 2kT. \quad (2.53)$$

At a temperature of 1450 K, the average kinetic energy would be around 250 meV, and this was the value used in the simulations.

The resulting initial velocity  $u$  of the electrons can be calculated from the energy  $U$  in eV using Eq. 2.31

$$u = \sqrt{\frac{2Uq}{m}}. \quad (2.54)$$

An initial energy of 250 meV will result in a magnitude of the initial velocity of about  $3 \times 10^5 \text{ m/s}$ . However, an estimate for the spatial distribution of the initial velocity of the electrons is also needed. As the electrons are emitted from circular wires, it is assumed that their spatial distribution is homogenous, as no direction is preferred. This is illustrated in Fig. 2.9.

## 2.4.2 Emission from EGP

To the authors knowledge, no data or theoretical calculations for the energy distribution from single EGPs are published. However, Burle, Inc. has conducted

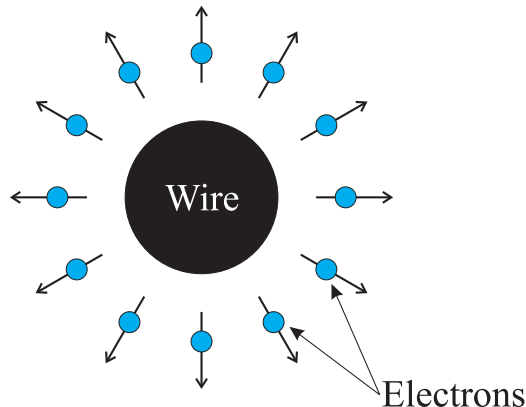


Figure 2.9: *The emittance of electrons from the heated wires is assumed to be spatially homogenous, as no direction is more probable than any other.*

measurements for Z-Stack configuration EGAs [18]. The results are assumed to be similar, but with somewhat lower average energy than for the electrons emitted from a single EGP [19].

The measured results from Burle, Inc. can be fitted to the shape of an *exponential distribution* [22] for the energy  $U$

$$p(U) = \frac{1}{\beta} e^{-U/\beta}, \quad (2.55)$$

where the parameter  $\beta$  is the average energy of the electrons. For the measured results the average energy is in the range of 34 to 40 eV, however these measurements were done using a Z-Stack configuration EGA, not a single EGP as will be used in the IPM. Since it is expected that the average energy will be lower, an estimate of 30 eV is therefore used in the simulations. This coincides with values obtained from measurements of emittance from single MCPs, where the distribution is reported to be exponential with an average electron energy of 30 eV [3]. A plot of the energy distributions is shown in Fig. 2.10.

The electron current emitted from an EGP is claimed to be more or less parallel [18]. However, no exact figures or quantification on how much the electrons deviate from completely parallel emittance are published.

A rough estimate can be made from theory published about the operating principle of MCPs [3]. It is assumed that the initial energy of an emitted secondary electron within the channels of the MCP is approximately 1 eV, and that the secondary electrons are emitted perpendicular to the channels. Further, the total average energy of an electron when leaving the channel, is assumed to be around 30 eV. By taking the ratio between these two values, an estimate for

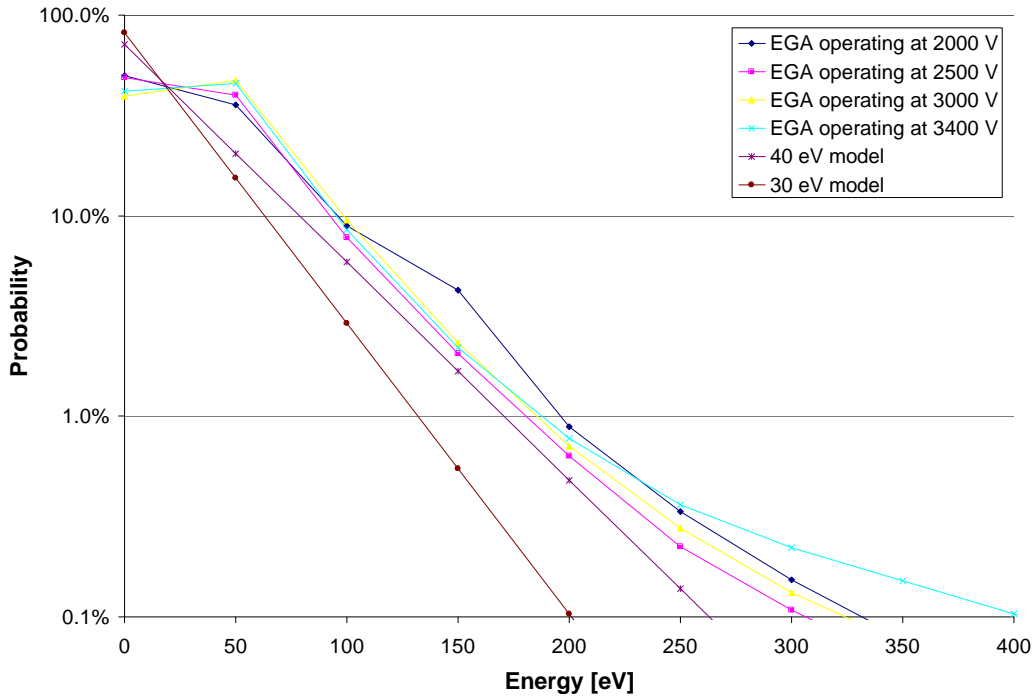


Figure 2.10: *The energy distribution of electrons emitted from the EGA. The measured results are for a Z-Stack configuration measured by Burle. The modelled results are exponential distributions with average energy of 30 or 40 eV, respectively.*

the average angle of emittance with respect to the channel can be found,

$$\theta = \arcsin\left(\frac{1}{30}\right) \approx 2^\circ. \quad (2.56)$$

As input to the simulations, the emittance angle of the electrons with respect to the channels is assumed to have a *uniform distribution* [22] on the interval from  $-5^\circ$  to  $+5^\circ$ . The principle is illustrated in Fig. 2.11. These estimates were used as initial conditions for the simulations presented in the next chapter. The effects of making errors in these estimates will be discussed later.

The EGP from Burle, Inc. is specified to emit minimum  $10^{-9}$  A when operating at 1000 V [11]. The size of the EGP is 5.08 cm by 5.08 cm, so this equals an emission current of more than  $10^{-11}$  A/cm<sup>2</sup>. If the operating voltage is reduced, the emission current will of course be lower.

The emission current from the selected source for the calibration, must of course be within the range of the detection system. The limits of the detection system, will be discussed in the next section.

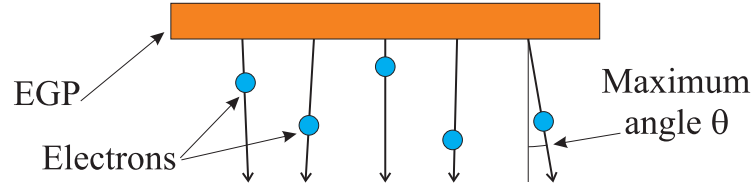


Figure 2.11: *The electrons from the EGP are assumed to be emitted more or less in parallel.*

### 2.4.3 Resulting intensity at the MCP

According to estimates conducted by Jan Koopman,  $10^6$  to  $10^7$  electrons per second are needed on the surface of the MCP to produce a good image of the beam [25]. The size of the MCP is 5.08 cm by 5.08 cm, so this equals a required minimum electron current about of  $10^{-14}$  to  $10^{-13}$  A/cm<sup>2</sup>.

The upper limit of the recordable electron current is given by the saturation limit of the MCP. Saturation effects start to occur at the MCP when the electron current reaches 10% of the MCP bias current [19]. The bias current of the MCP is specified to  $26-106 \times 10^{-6}$  A [11]. Consequently, as a worst-case estimate, saturation effects will start to occur at  $10^{-7}$  A/cm<sup>2</sup> when operating the MCP at 1000 V. Operating the MCP at a lower voltage, will result in a lower threshold for the onset of saturation effects.

The key figures for the electron emission current are summarised in Table 2.1.

Source/detector	Electron current [A/cm <sup>2</sup> ]
Emission from tungsten wire heated to 1450 K	Approximately $10^{-9}$
Emission from EGP operating at 1000 V	Minimum $10^{-11}$
MCP detection range operating at 1000 V	$10^{-14}$ to $10^{-7}$

Table 2.1: *Summary of key figures for electron emission currents.*

The table shows that both sources are expected to be within an acceptable current range, however the value given for the heated wire is somewhat more uncertain than the value for the EGP. This is caused by the exponential dependency upon the temperature  $T$ , and the large uncertainty in the Richardson constant  $A$  in Eq. 2.51. The emittance from a heated wire grid can however relatively easily be adjusted by changing the current in the wire.

The next question to consider, is which of the two sources will give the most homogenous electron distribution at the MCP. The resulting distribution can be computed using the theoretical description of how the electrons move through

electromagnetic fields, presented in the first sections of this chapter. In order to obtain an answer to the question, the estimates of the initial conditions for the electrons originating from the two different sources must be taken into account. For a large number of electrons, the amount of calculations and information to keep track of becomes so large that an analytical approach to this question would be useless. Computer simulations were therefore used to numerically analyse the drift of the electrons, and the resulting distribution at the MCP, subject to different conditions.

Considering the nature of the two different sources, the effect sought by drifting the electron through the chamber is radically different. For the case of the wires, the initial distribution is very inhomogeneous, and the goal when selecting the setting for the electric and magnetic field, is therefore to spread the distribution as much as possible. In this way, the resulting distribution at the MCP would become more uniform. In order to obtain this, two different approaches can be used. Either no magnetic field should be applied, so that the electrons spread out freely, or a magnetic field of

$$\frac{1}{2}B_l = \frac{\pi}{2d} \sqrt{\frac{2m\Phi}{q}}, \quad (2.57)$$

should be applied, so that the electrons complete one half revolution during their drift through the IPM, see Section 2.2.2. For the case of  $d = 90$  mm and  $\Phi = 2143$  V, and no initial energy in the y-direction, a value of  $\frac{1}{2}B_l = 27$  Gauss is found.

When the emission from the EGP is considered, the opposite is the case. The initial distribution is indeed expected to be quite homogenous, and the goal is to preserve this distribution during its drift to the MCP. To achieve this, one solution would be to apply a magnetic field as strong as possible, constraining the maximum possible offset of the electrons, see Section 2.2.2. Another solution would be to apply a magnetic field of

$$B_l = \frac{\pi}{d} \sqrt{\frac{2m\Phi}{q}} = 55 \text{ Gauss}, \quad (2.58)$$

assuming the same conditions as above. This would cause the electrons to complete exactly one revolution, and arrive with the same distribution at the MCP. If the change in drift time, caused by the electrons having initial energy in the y-direction, is taken into account, the value for the magnetic field would be higher.

The results of the simulations for the different cases are presented in the following chapter. The data obtained from the simulations, were used to determine the optimal field configuration.



# Chapter 3

## Simulations

To better understand the behaviour of electrons in the IPM, and more specifically how to implement an electron source to calibrate the system, computer simulations were performed. Numerical simulations offer a higher degree of accuracy, as less approximations have to be made compared with analytical computations. Simulations are also relatively cheap to carry out, and can reduce the need for costly and time consuming experiments.

The computer simulations were split into two main parts: Simulations of the electrical field, and simulations of the paths of the electrons. To compute the electrical fields, the computer program *Maxwell 3D Field Simulator* (M3DFS) from Ansoft Corporation [26] was used. Several programs are able to do these types of computations, but M3DFS was chosen because of its compatibility with the program used for the electron drift, the availability at CERN, and its user-friendliness.

The program used to calculate the paths of the electrons through the electric and magnetic fields was *Garfield* [27]. *Garfield* was originally developed at CERN by Rob Veenhof for simulation of gaseous detectors. The program reads the results of the electrical field simulations created by M3DFS from file, and then calculates the path of the electrons. The *Garfield* program can also be instructed to deal with a magnetic field in addition to the electric field.

Four different setups, or operation modes, of the IPM were simulated. The first case to be considered, to be used as a reference, was a simulation of the electric field in the original IPM setup. Next, field simulations and simulations of the electron paths were done for models of the IPM with a wire grid or an EGP implemented as electron sources. Finally, some simulations were done to understand how implementing an EGP would influence the electric field in IPM during beam profile measurements.

In the following parts of this chapter, the computational principles of the software will be outlined, before the results of the simulations are given.

## 3.1 Electrostatic field simulations

The electric field simulations were done for the electrostatic case, in other words assuming perfect insulators and no drift currents. The equation which is solved by M3DFS is in general [28]

$$\nabla \cdot (\epsilon \nabla \Phi) = -\rho_f, \quad (3.1)$$

where  $\Phi$  is the scalar electric potential. This equation is known as the Poisson equation, and can be derived from Eq. 2.5 using the relation between  $\mathbf{D}$  and  $\mathbf{E}$  given in Eq. 2.11. The relation between the electric field and the scalar electric potential in a static field is given by [15]

$$\mathbf{E} = -\nabla \Phi, \quad (3.2)$$

yielding

$$\nabla \cdot \mathbf{D} = \nabla \cdot (\epsilon \mathbf{E}) = \nabla \cdot (-\epsilon \nabla \Phi) = \rho_f. \quad (3.3)$$

After the solution for the scalar electric potential is generated, M3DFS uses these relationships to compute the electric field  $\mathbf{E}$  and the electric flux density  $\mathbf{D}$ .

The assumption of no drift currents also implies that there will be no free charges, that is  $\rho_f = 0$ . At the interface between two media the following condition then applies [15]

$$\epsilon_1 E_1^\perp - \epsilon_2 E_2^\perp = \rho_f = 0, \quad (3.4)$$

where  $E_1^\perp$  and  $E_2^\perp$  are the normal component of the electric field in media 1 and 2, respectively. The electric field in each material is then determined entirely by the permittivity of the media, as

$$E_1^\perp = \frac{\epsilon_2}{\epsilon_1} E_2^\perp. \quad (3.5)$$

When these relations are known, the next step is to find a suitable numerical method to solve the resulting equations. The employed method is described in the next section.

### 3.1.1 The finite element method

The *finite element method* consists of several numerical techniques to calculate structural properties, flow and fields. It is widely used in engineering, when the problems become too complex to be solved analytically [29, 30, 31]. M3DFS uses this technique to compute an approximation of the scalar electric potential, and from this computes the electric field [28].

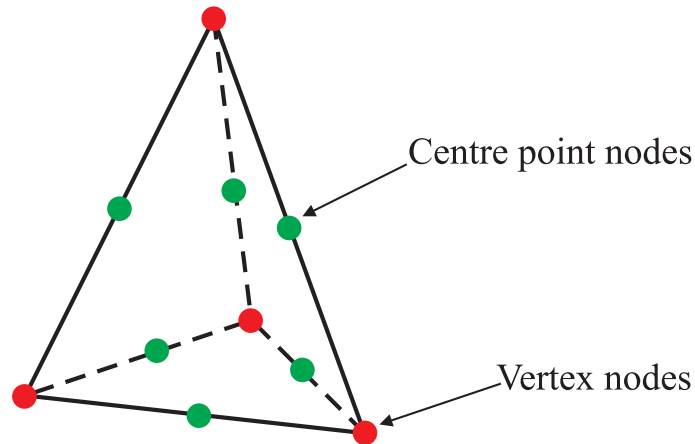


Figure 3.1: *One tetrahedron element with nodes at the vertices and half-way points in between.*

The volume in which the field is to be computed, is subdivided into a number of *elements*. The way the volume is divided is called the *mesh*. In three dimensions, tetrahedrons and hexahedrons are most commonly used. M3DFS uses tetrahedrons to create the mesh, as shown in Fig. 3.1. Elements never cross material boundaries, and so the dielectric constant will always be the same within an element. Since there is no field inside a conductor, no mesh is created within these.

A value for the potential is computed for each of the *nodes* of each element, while trying to satisfy the Poisson equation (Eq. 3.1) and respecting the boundary conditions. At least the vertices are among the nodes of the elements, but also other points can be used in addition. The centre point between two vertices is also commonly included as a node, as is the case for the algorithm used by M3DFS. The nodes at the vertices of two elements are often shared between neighbouring vertices, and thereby assigned the same value. An example of the mesh created by M3DFS is shown in Fig. 3.2.

Nodes located at the surface of a conductor imposed at a specific potential, will be assigned the potential of the conductor. This is called the *Dirichlet boundary condition*. If the value of the potential at a boundary is unknown, the *Neumann boundary condition* will apply. This states that the electric field intensity must be tangential to the boundary.

The potential for the region between the nodes within the elements, is interpolated using *shape functions*. These shape functions are usually first, second or third order polynomials. The potential which is computed, is therefore in general not an exact solution of the Poisson equation (Eq. 3.1). In the case of M3DFS, second order polynomials are used, which implies 10 nodes per

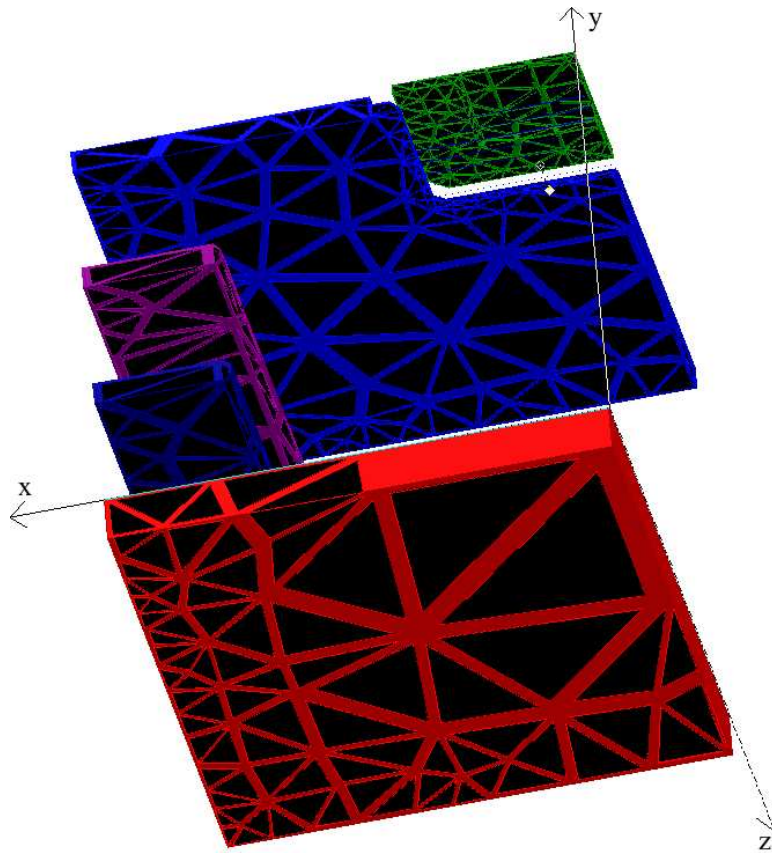


Figure 3.2: *The mesh created at the surface of some of the components in the IPM with the EGP. To better visualise the mesh, some space is included between the elements.*

tetrahedron element.

The accuracy of the solution can be improved by further subdivision of the elements of the mesh where higher accuracy is required. This is normally automatically done by the finite element program, until an acceptably low error is reached. If the model in question has a complex geometry, in particular a large difference in the object dimensions, manual refining of the mesh is often required. The accuracy of the computations can often be substantially improved by adding *virtual volumes*. Virtual volumes are volumes of the same medium added around the objects of particular interest. Adding several such volumes around each other, will force the finite element program to make a finer mesh in this area, as the elements of the mesh never cross volume borders. An sketch of how this can be done is shown in Fig. 3.3.

Finite element methods compute the potential, and not the electric field which determines the movement of the particles in the detector. The potential is guaranteed to be continuous, as the value of the nodes common to adjacent

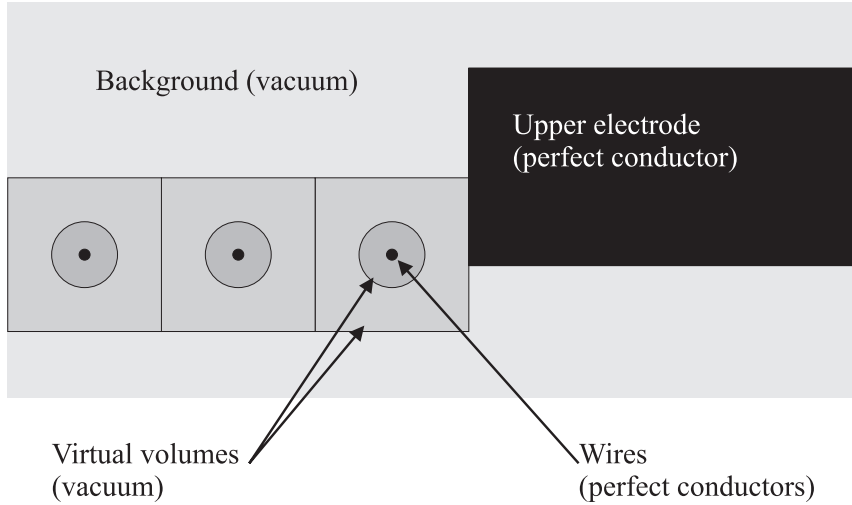


Figure 3.3: An example of how virtual volumes can be used to improve meshing (not to scale). The dimensions of the wires are very small compared to the rest of the geometry in the model, and it is important to accurately compute the field near the wires because this affects the path of the electrons. Adding virtual volumes around the wires improve the meshing, and thereby the accuracy of the field calculations, as elements never cross the boundaries of the virtual volumes.

elements indeed has the same potential. However, the finite element method does not guarantee a continuous electric field, in fact the field is often discontinuous. This unavoidably introduces some errors when tracing particles through the field. Nevertheless, using a mesh that is sufficiently fine, these errors can be kept at a minimum.

## 3.2 Electron path simulations

The path of the electrons through the IPM chamber is calculated by the Garfield program, integrating the expression for the acceleration given in Eq. 2.27

$$\mathbf{a} = \frac{q}{m} \gamma^{-1} (\mathbf{E} + \mathbf{u} \times \mathbf{B} - \frac{1}{c^2} \mathbf{u}(\mathbf{u} \cdot \mathbf{E})). \quad (3.6)$$

The numerical method used by the Garfield program is *Runge Kutta Fehlberg integration* [27].

An estimate for the time used by an electron to drift through the chamber can be calculated from Eq. 2.32. With a distance between the electron emitter and the MCP of  $d=90$  mm and a potential difference of about  $\Phi=2000$  V, the drift time is 6 to 7 ns. The initial energy of the electrons is not taken into account in

this estimate. More exact values for the drift time will be presented later in this chapter.

Using this estimate for the drift time, together with values for the electron current presented in Section 2.4.3, an estimate for the average number of electrons present at the same time in the drift volume of the IPM can be given. The results are presented in Table 3.1.

Source/detector	e <sup>-</sup> in drift volume	e <sup>-</sup> per cm <sup>3</sup>
Wire heated to 1450 K	1000	5
EGP operating at 1000 V	10	0.05
Acceptable MCP range at 1000 V	0.01 to 10 <sup>5</sup>	5 × 10 <sup>-5</sup> to 500

Table 3.1: *The average number of electrons present at the same time in the drift volume of the IPM, and per cm<sup>3</sup>. A drift volume of  $9 \times 5.08 \times 5.08 \text{cm}^3 = 230 \text{cm}^3$  is assumed.*

Referring to Eq. 2.14, an estimate for the contribution to the electric field caused by the electrons in the drift volume can be made. If the electrons are assumed to be spread out evenly throughout the volume, the resulting field in the center of the volume would be zero, as the field contributions from the electrons in each part of the volume cancel each other.

However, at any of the edges of the drift volume, the electrons will give some contribution. As a worst case scenario, the field contribution at the center of the MCP from a drift volume filled with  $n = 10^5$  electrons can be considered. In this case, the field contribution in the x- and z-direction will cancel out, but there will still be a contribution in the y-direction. Equation 2.14 then simplifies to

$$\mathbf{E}(\mathbf{r}) = \frac{1}{4\pi\epsilon_0} \int_d \frac{\rho}{y^2} \hat{\mathbf{y}} dy, \quad (3.7)$$

where  $d = 90 \text{mm}$  is the distance from the electron emitter to the MCP. The charge density per length in the y-direction will be given as

$$\rho = \frac{nq}{d}. \quad (3.8)$$

Solving the expression yields

$$\mathbf{E}(\mathbf{r}) = \frac{1}{4\pi\epsilon_0} \frac{nq}{d} \left( \frac{1}{y_{min}} - \frac{1}{d} \right) \hat{\mathbf{y}}, \quad (3.9)$$

where  $y_{min}$  is the lower limit of the integration, i.e. the distance from the MCP to the first electron. This cannot be chosen to zero, as this would result in an infinite field. As an estimate for  $y_{min}$ , the average distance between the electrons can be used. Assuming, as previously, that there are  $10^5$  electrons homogeneously

distributed within the drift volume of  $9 \times 5.08 \times 5.08 \text{cm}^3 = 230 \text{cm}^3$ , the average volume per electron is  $2.3 \times 10^{-9} \text{m}^3$ . This results in an average distance between the electrons of about 1 mm. Using these values, the worst-case-estimate for the contribution made to the electric field by the electrons in the drift area becomes

$$E \approx 1V. \tag{3.10}$$

The direction of this field contribution is in the +y-direction. This should be compared to the applied field strength of about 2000 V. Consequently, the resulting field from the electrons present in the drift volume will be negligible compared to the applied electric field in the IPM, even for the highest density of electrons recordable by the MCP. In other words, the effect of electron-electron interactions can safely be disregarded in further computations. An algorithm that does not take electron-electron interactions into account is therefore chosen to be used in the Garfield simulation program.

### 3.2.1 The magnetic field

In addition to the electric field, Garfield was also instructed to deal with the magnetic field in the IPM.

According to previous measurements, the magnetic field applied to the IPM is homogenous within an error of less than 1% throughout the volume of interest, that is the volume of the IPM [32]. The error introduced by using a completely homogenous magnetic field as input to the Garfield program is therefore small. When the program is instructed to include a homogenous magnetic field, it makes corrections for the differences in magnetic permeability among the different materials, although these effects usually are negligible [29].

A magnetic field strength of up to 2000 Gauss can be applied to the IPM, however even if no current is applied to the electromagnet, a remanent field of approximately 5 Gauss will still be present [32].

### 3.2.2 Resolution

The limiting factor for the resolution of the electron path simulations, is the recording of the initial and final position of the electrons. 100 by 100 bins are used, resulting in a bin size of 508 by 508  $\mu\text{m}$ , when the entire area of the EGP or MCP is imaged. Increasing the resolution further would require more computer power. Not only would it require larger matrices to store the positions, but also a larger number of electron paths would have to be computed in each simulation so that an acceptable average number of electron reach each bin. In the simulations  $10^5$  electron paths were computed for each case, resulting in an average of 10 electrons per bin. If the electron distribution is plotted along either the z or x-axis only, an average of 1000 electrons per bin is obtained in one dimension.

For some cases this resolution was too coarse, and more detailed simulations were then done for the region of interest.

### 3.3 Results of the simulations

In the following section, the results of the simulations are presented. To simplify computations, the symmetry of the IPM was exploited so that only one quarter of the volume needed to be modelled. The coordinate system is the same as for the schematic presented in Fig. 1.2 (a) in the introduction, with the origin (0,0,0) chosen at the centre of the upper face of the MCP.

It is assumed that the metal electrodes are perfect conductors, and that the insulators are perfect insulators. They are not present in the model, as a perfect insulator has the same permittivity and conductivity as vacuum. The first case to be considered is the original IPM setup.

#### 3.3.1 The original IPM

The model of the IPM constructed in M3DFS is shown in Fig. 3.4, with some equipotential lines of the electric field indicated. A bias voltage of 1000 V is chosen, that is +1000 V for the positive (lower) electrode, and -1000 V for the negative (upper) electrode. The distance between the electrodes is 84 mm. The wire grid is at the same potential as the negative electrode. The absolute value of the voltage chosen is in fact arbitrary, because in this case the interesting feature are the relative differences in the field.

A plot of the equipotential lines of the electric field for the entire volume of interest, is shown in Fig. 3.5. The plots show cuts through the volume at  $x=0$  and  $z=0$ , respectively. The field is plotted a small distance away from the planes at  $x=0$  and  $z=0$ , because some numerical inaccuracy occurs here as this is the outer boundary of the M3DFS simulations. The plots are made using the Garfield program, after importing the field maps from M3DFS.

From the plots of the equipotential lines of the electric field, it is evident that the cathode grid causes some distortion to the field in the IPM. However, in the lower half of the IPM, the field is quite homogenous. This is what really matters, since during operation of the IPM the electrons to be imaged are created near the centre and then drift down to the MCP. It is important that implementing an electron emitter in the IPM does not cause further inhomogeneity to this field during beam measurements.

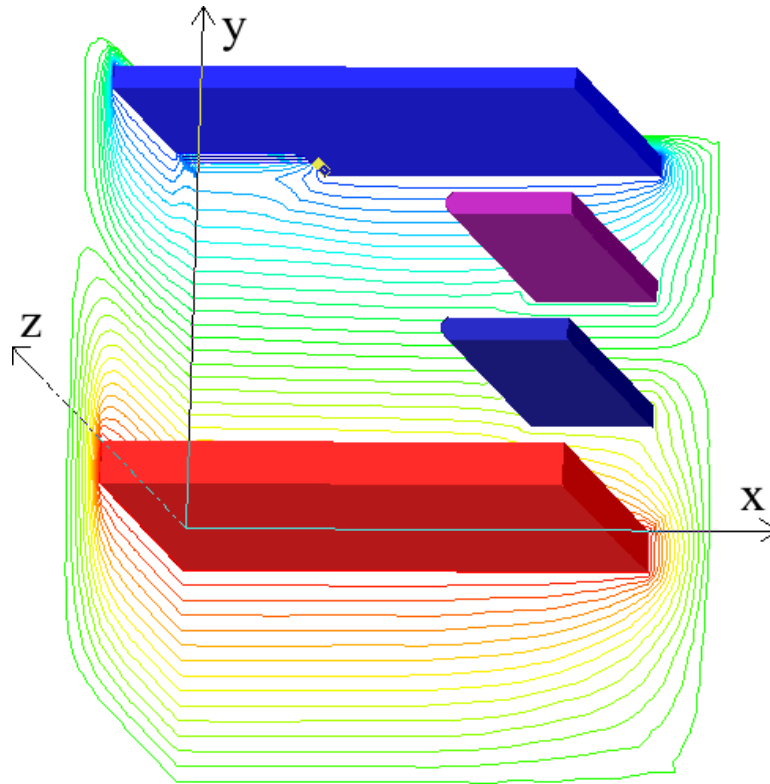


Figure 3.4: *The model of the original IPM as constructed in M3DFS. Symmetry was exploited, so that only one quarter of the volume is modelled. For clarity, the shielding ground tank is not shown in the drawing. The cathode grid can be seen in the upper left part of the model. The lateral electrodes are included in the system to improve the homogeneity of the electric field. In addition, some equipotential lines of the electric field are shown along the symmetry axis of the model.*

### 3.3. RESULTS OF THE SIMULATIONS

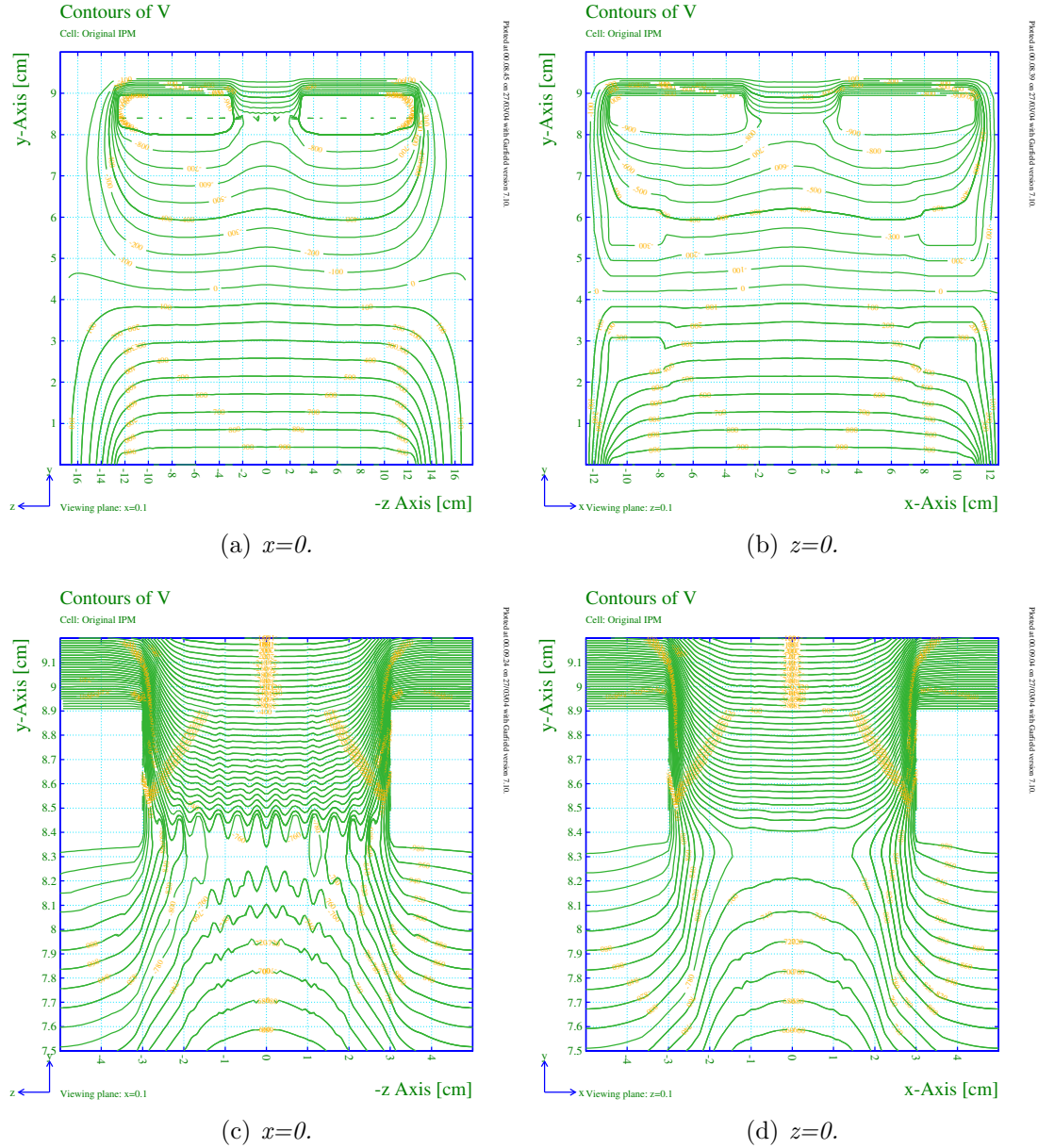


Figure 3.5: Equipotential lines of the electric field for the original setup of the IPM. Cuts are made through the centre of the volume, but the view is chosen a small distance away from the axis, to suppress numerical inaccuracy near the edges of the simulation. (a) and (b) show the entire volume, while (c) and (d) present enlarged plots of the region near the cathode grid. The beam passes in direction of the  $z$ -axis.

### 3.3.2 IPM with wire grid emitter

The original model of the IPM was modified to include a wire grid as an electron source for calibration, as described in the introduction and sketched in Fig. 1.6. The emitting wire grid was chosen to have the same dimensions as the cathode grid, that is a wire diameter of  $50 \mu\text{m}$  and a distance between the wires of  $4.65 \text{ mm}$ . The emitting wire grid was placed  $6 \text{ mm}$  above the cathode grid, with the wires perpendicular to it. In order to heat the wires, a potential difference must be applied to them. The potential will drop along the wires, but the perturbations this would cause to the electric field are not taken into account in the model, as they are expected to be small compared to the applied electric field. The voltage drop across such a wire would typically be around  $10 \text{ V}$ , resulting in a contribution to the electric field of approximately  $1\text{-}2 \text{ V/cm}$ . In comparison the electric field used during calibration of the IPM is approximately  $240 \text{ V/cm}$ . The wire grid could also be arranged so that the voltage drop across neighbouring wires would be in opposite directions, thereby minimising the perturbations further.

An electrode is also introduced  $2 \text{ mm}$  above the emitting wire grid, to be able to create and control a sufficient extraction field for the emitted electrons. The modified part of the model is shown in Fig. 3.6.

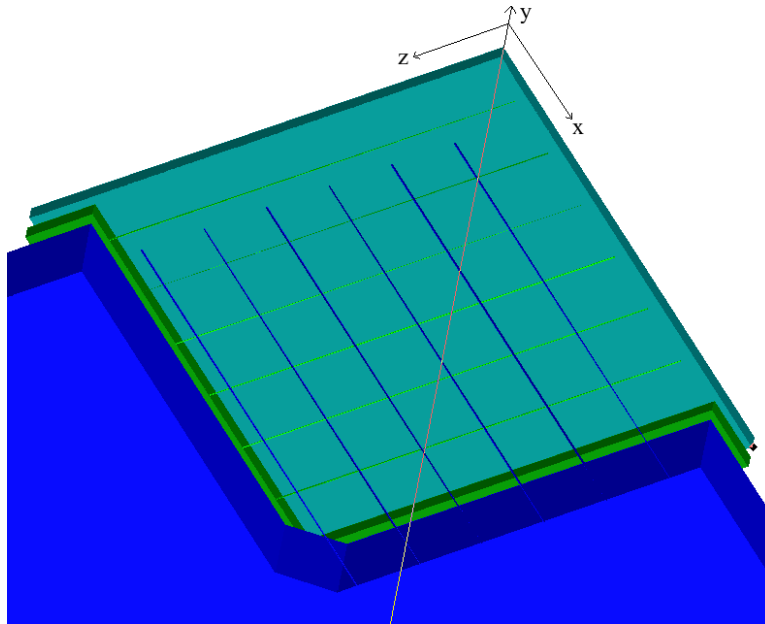


Figure 3.6: *The modified part of the IPM, viewed from below. A wire grid to emit electrons is introduced in addition to a electrode to create an extracting field.*

The potential of the emitting wire grid relative to the cathode grid, is chosen so that the electric field throughout the chamber is as homogenous as possible. The

potential of the emitting wire grid can be found using Eq. 3.2, in one dimension

$$E = -\frac{\partial\Phi}{\partial z}. \quad (3.11)$$

Assuming the electric field  $E$  to be constant between the electrodes, an expression for  $E$  can be found using values of the potentials at the electrodes,  $\Phi_{pos}$  and  $\Phi_{neg}$ ,

$$E = \frac{\Phi_{pos} - \Phi_{neg}}{d_{el}}, \quad (3.12)$$

where  $d_{el}$  is the distance between the electrodes. The potential of the emitting wire grid relative to the negative electrode is then given as

$$\Phi_{wire} = Ed_{wire}, \quad (3.13)$$

where  $d_{wire}$  is the distance between the emitting wire grid and the cathode grid. As  $\Phi_{pos}$  and  $\Phi_{neg}$  are chosen to  $\pm 1000$  V, the value of  $\Phi_{wire}$  becomes

$$\Phi_{wire} = Ed_{wire} = \frac{\Phi_{pos} - \Phi_{neg}}{d_{el}}d_{wire} = \frac{1000 - (-1000)\text{V}}{84\text{mm}}6\text{mm} \approx 143\text{V}. \quad (3.14)$$

The potential of the electrode above the emitting wire grid can be computed in the same way. Note that this field configuration is valid only during calibration mode of the IPM. During beam measurements the potential of the emitting wire grid must be adjusted to avoid secondary electrons escaping from above the cathode grid and into the chamber, as described in Section 1.1 in the introduction.

During operation  $\Phi_{pos}$  and  $\Phi_{neg}$  are chosen to  $\pm 2000$  V, while the beam, the source of the electrons, is in the centre of the chamber. The potential difference for the electrons, from the centre of the chamber to the positive electrode, is therefore 2000 V. During calibration  $\Phi_{pos}$  and  $\Phi_{neg}$  are chosen to  $\pm 1000$  V, as the electrons then drift from the top of the chamber, that is from the heated wire grid.<sup>1</sup> The potential difference for the electrons is then, as during operation, approximately 2000 V.

The energy of the electrons as they reach the MCP is then consequently approximately 2 keV. At this energy the MCP achieves its optimal detection efficiency of 50-85% [3].

The resulting electric field maps are shown in Fig. 3.7. The electric field obtained using the potential settings described above, proves to be quite homogenous within the drift area of interest, the volume between the MCP and the emitting wire grid. Only some small perturbations are observed near the edges of the cathode.

---

<sup>1</sup>One could argue that the potentials during calibration mode should be chosen to  $\pm 933$  V, so that the potential difference between the electron emitter and MCP is exactly 2000 V, instead of 2143 V. However, for simplicity,  $\pm 1000$  V was chosen.

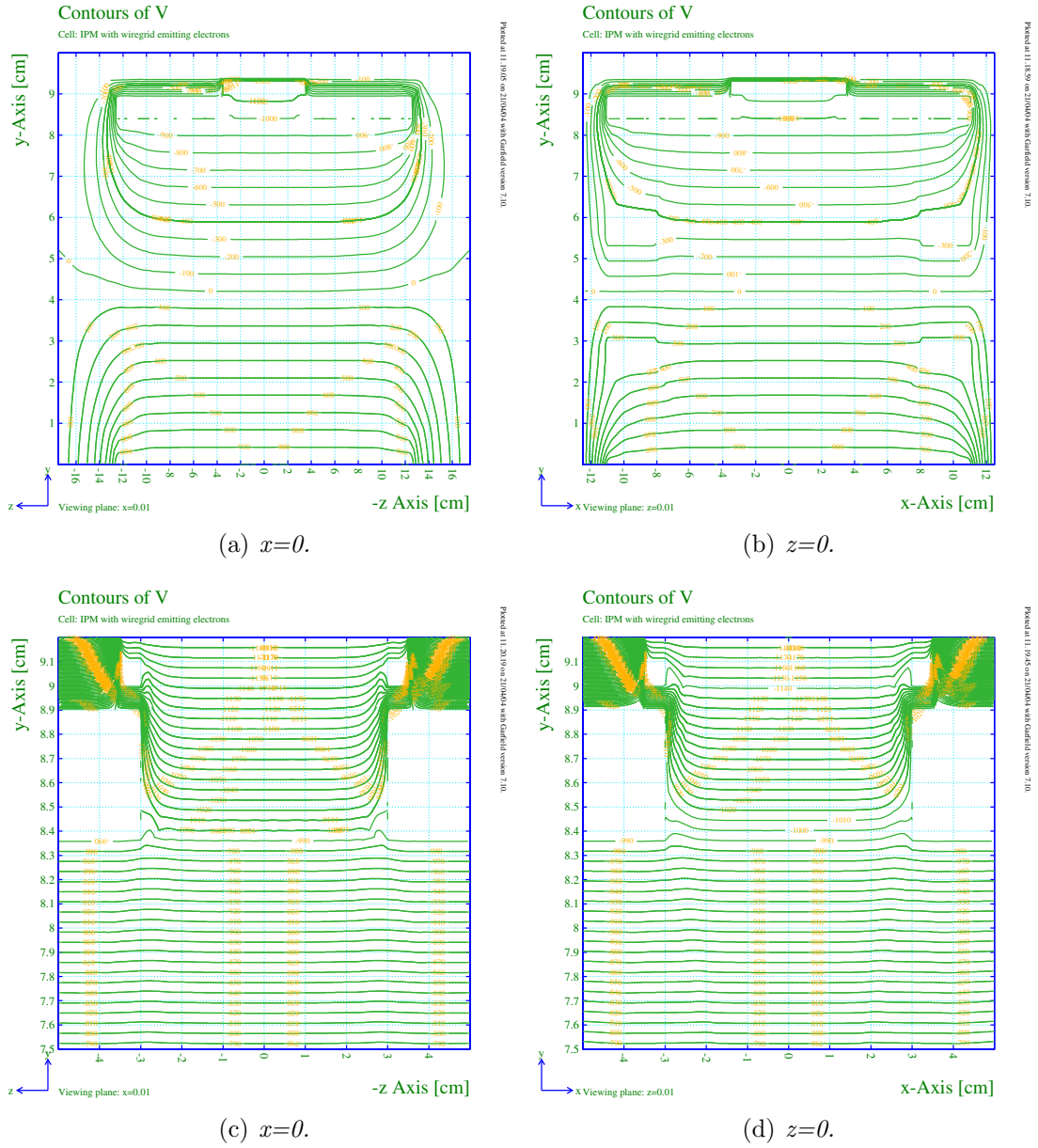


Figure 3.7: The electric field in calibration mode with a wire grid to emit electrons integrated in the IPM. Cuts are made through the centre of the volume, but the view is chosen a small distance away from the axis, to suppress numerical inaccuracy near the edges of the simulation. (a) and (b) show the entire volume, while (c) and (d) present enlarged plots of the region near the cathode grid.

The initial energy distribution of the emitted electron presented in Sec. 2.4.1, was implemented in the source code for the simulations with the Garfield program.

### 3.3. RESULTS OF THE SIMULATIONS

The complete code for the simulations can be found in Appendix A. The resulting energy and velocity distribution is shown in Fig. 3.8. From the graph it is clear that the difference in initial energy and velocity between different electrons is rather large. Individual electrons are therefore expected to take quite different paths from the emitting wire to the MCP.

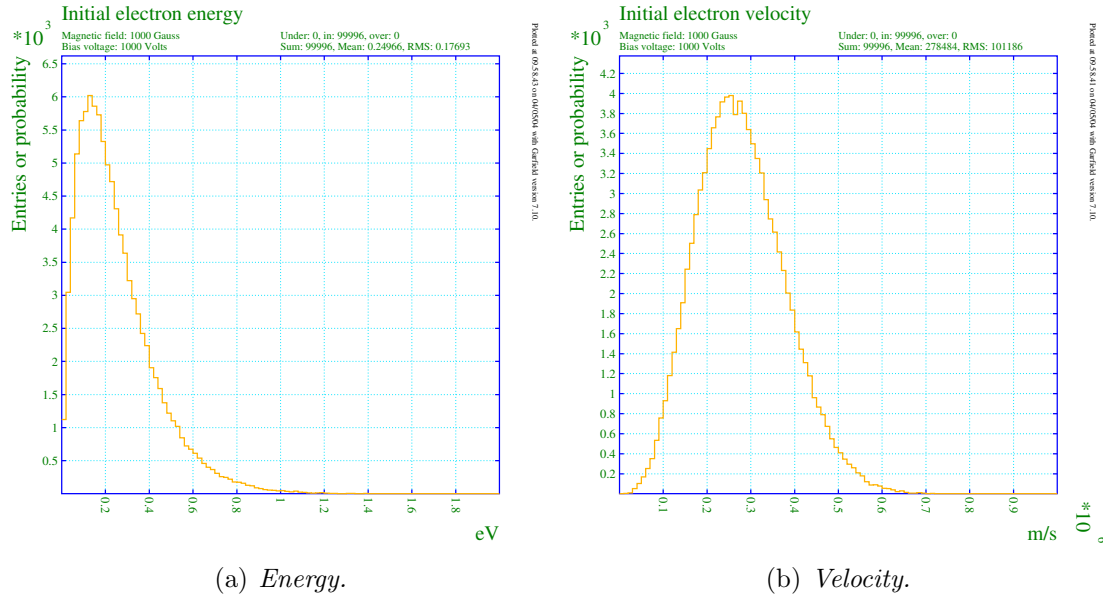


Figure 3.8: Typical distributions of initial energy and velocity of the electrons emitted from the heated wire grid, simulated with the Garfield program.

Using the initial conditions given in Section 2.4.1, a plot of the initial electron distribution could also be generated. The resulting electron distribution is shown in Fig. 3.9.

As shown in Eq. 2.44 in the theory chapter, a variation in the initial energy will also cause a difference in the drift time through the chamber. The drift time is however independent of the magnetic field. A histogram of the resulting drift times are shown in Fig. 3.10. A mean value of 6.52 ns is obtained, and from the graph a FWHM of about 0.3 ns is found. These values are close to the theoretical estimate, as the average initial energy is low compared with the field strength.

The Garfield program was instructed to calculate the drift paths of the electrons as described in Section 3.2. The drift paths were calculated for several different magnetic fields. An example of the drift paths of a few hundred electrons, both in low and a high magnetic field, are shown in Fig. 3.11. As predicted in Section 2.2, the plots indicate that the path of the electrons are highly dependent upon the magnetic field strength.

More time consuming simulations were also done, calculating the path of  $10^5$  electrons in different magnetic fields. Some of the resulting distributions

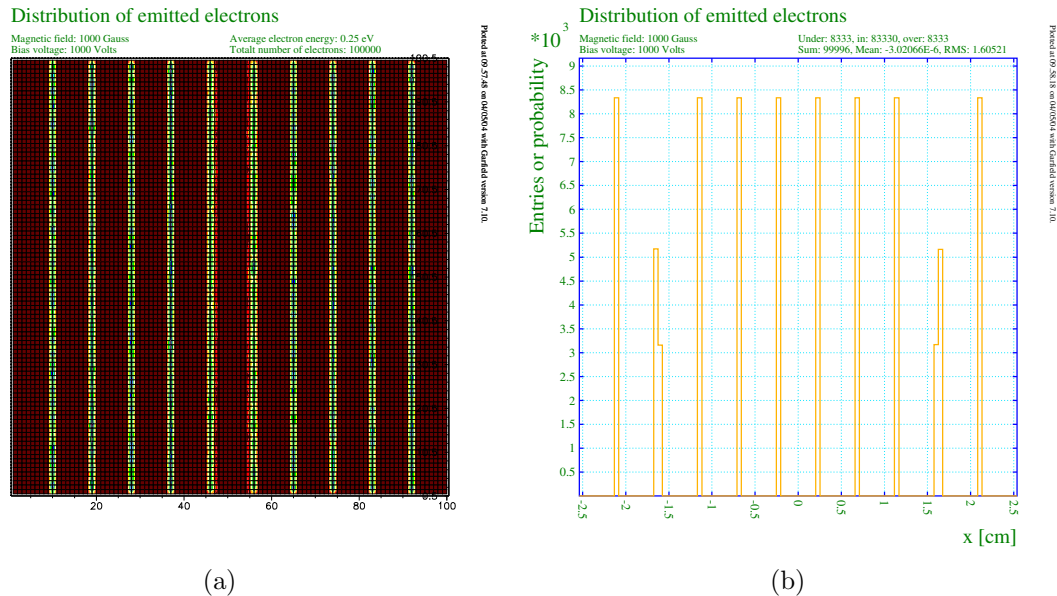


Figure 3.9: *Simulated distributions of emitted electrons from a heated wire grid. (a) Area shown is 5.08 cm by 5.08 cm, the same as the size of the MCP. The colour indicates the intensity of the electron distribution. (b) The intensity projected onto the x-axis. Two of the peaks appear lower and wider than the others, this is caused by large bin size in the histogram and the fact that the entries of probability are divided between two bins.*

of electrons emitted from a heated wire grid reaching the MCP are shown in Fig. 3.12.

From the figure it is evident that a low magnetic field cause the electrons to spread out more before they reach the MCP, thereby creating a more homogenous distribution on the MCP. However, even at low fields, the variations in intensity at the MCP are very large. At low field, some distortion near the edges are also observed. This distortion is assumed to be caused by inhomogeneity in the electric field near the edges. More detailed results are given in Table 3.2. If wires are used to emit electrons, the goal would be to spread the emitted electrons out as much as possible, so that the variation in intensity at the MCP becomes as small as possible. Table 3.2 gives the intensity variation at the MCP for magnetic fields from 0 to 1000 Gauss. The *Int. var. z* and *Int. var. x* columns give values for how much the intensity fluctuates from the average value in the z-direction (along the emitting wires) and the x-direction (perpendicular to the emitting wires), respectively. Small variations are given in percent, while large variations are given as ratio between the high and low values. The *Cross-section* column gives the width of the area without notable edge effects, and it is in this area the values for *Int. var. z* and *Int. var. x* are computed. Near the edges the

### 3.3. RESULTS OF THE SIMULATIONS

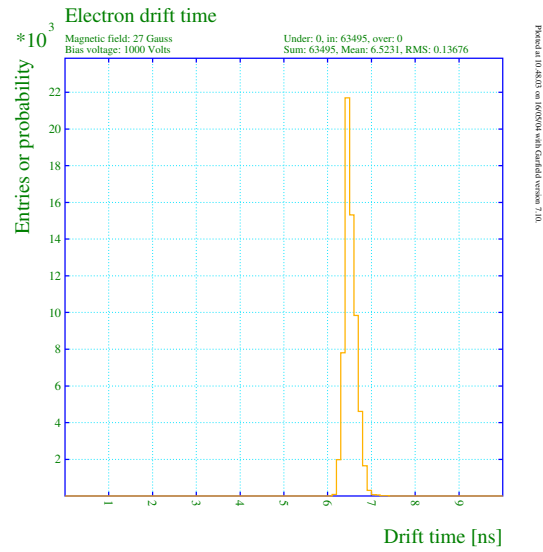


Figure 3.10: A histogram of the drift time for the electrons from the heated wire grid to the MCP.

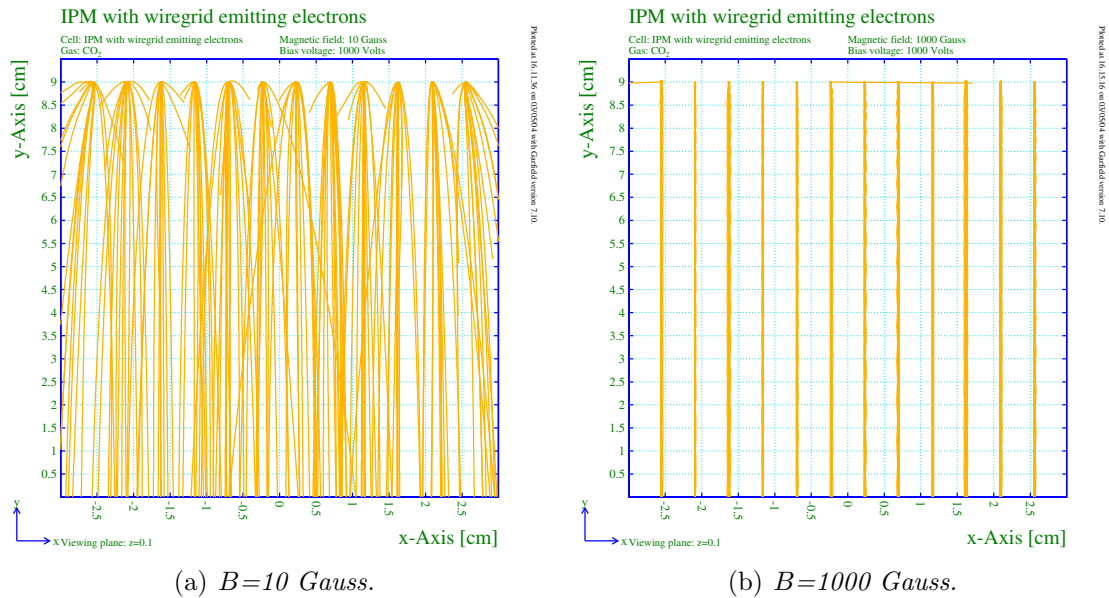


Figure 3.11: Drift lines of emitted electrons drifting through the IPM chamber at low and high magnetic field. (Note that even though perfect vacuum is assumed in the simulations, Garfield still prints a gas type in the graphs.)

variations are much larger, and including these variations in the main results would not provide any useful information. The value for the distortion at the

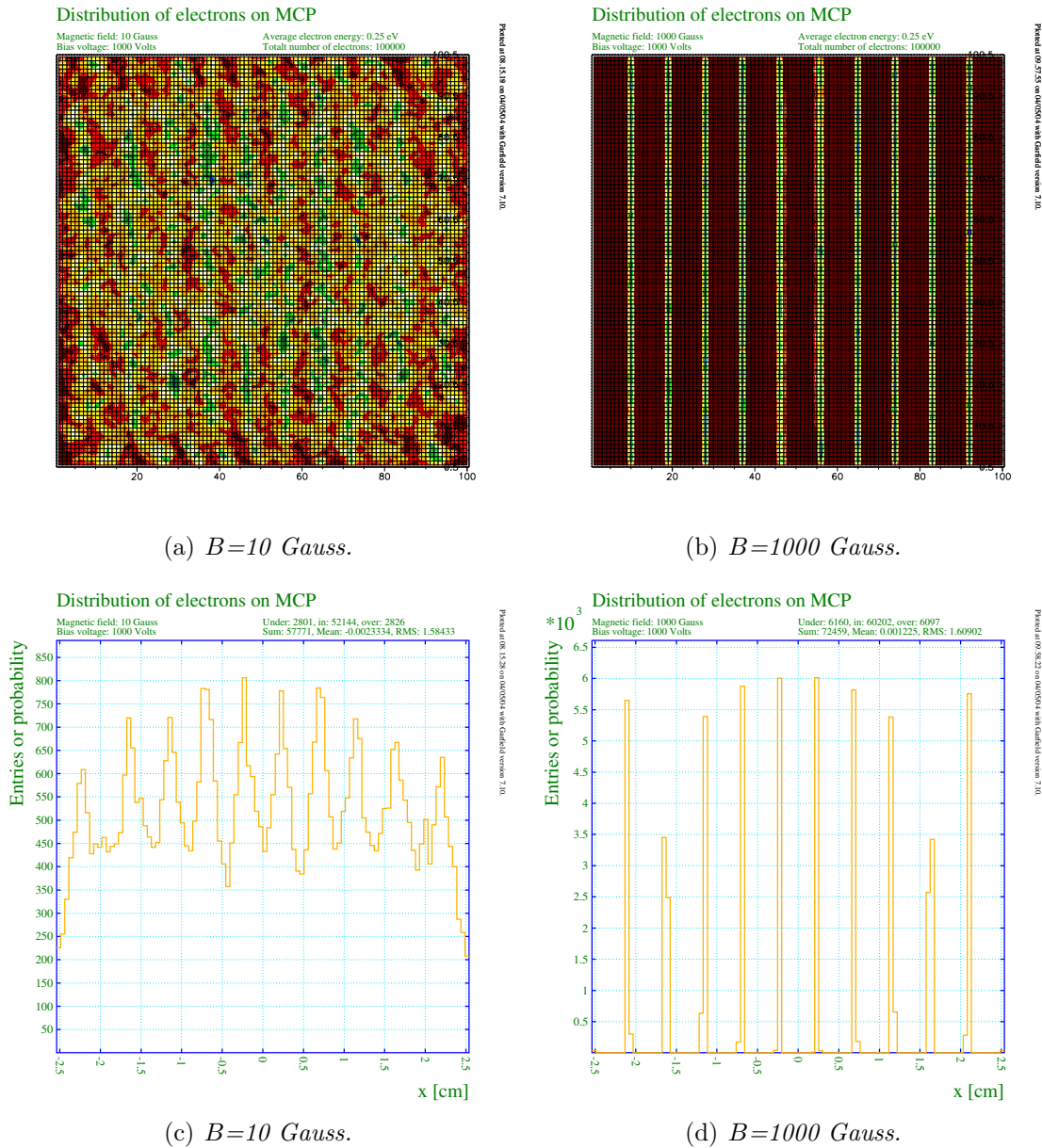


Figure 3.12: The resulting electron distribution on the MCP from Garfield simulations of electrons emitted from a heating wire grid. The area shown in (a) and (b) is 5.08 cm by 5.08 cm, the size of the MCP. In (c) and (d), the projection onto the  $x$ -axis is shown.

edges, is given in the *Edge dist.* column.

Using the average value for the drift time of 6.52 ns obtained from the simulations, the magnetic field required for one complete Larmor revolution can

### 3.3. RESULTS OF THE SIMULATIONS

B-field	Int. var. z	Int. var. x	Cross-section	Edge dist.
0 G	15 %	2 : 1	3.0 cm	50 %
10 G	12 %	3 : 1	3.5 cm	40 %
27 G	14 %	10 : 1	4.0 cm	40 %
100 G	12 %	40 : 1	4.5 cm	20 %
1000 G	10 %	Infinite	5.1 cm	-

Table 3.2: *Intensity variations in the electron distribution arriving at the MCP at different magnetic fields. Spatial resolution used for these computations is 508  $\mu\text{m}$ .*

be computed from Eq. 2.40. By applying a magnetic field at half this value, 27 Gauss, optimal spread of the electrons should be achieved. It is however evident from Table 3.2 that the results for this field strength also are poor.

By comparing the initial and final position, a value for the offset of each electron in the image plane (the plane spanned by the x- and z-axis) can be given. The histograms presented in Fig. 3.13 show the distance  $r$  electrons are shifted in the image plane for low and high magnetic fields.

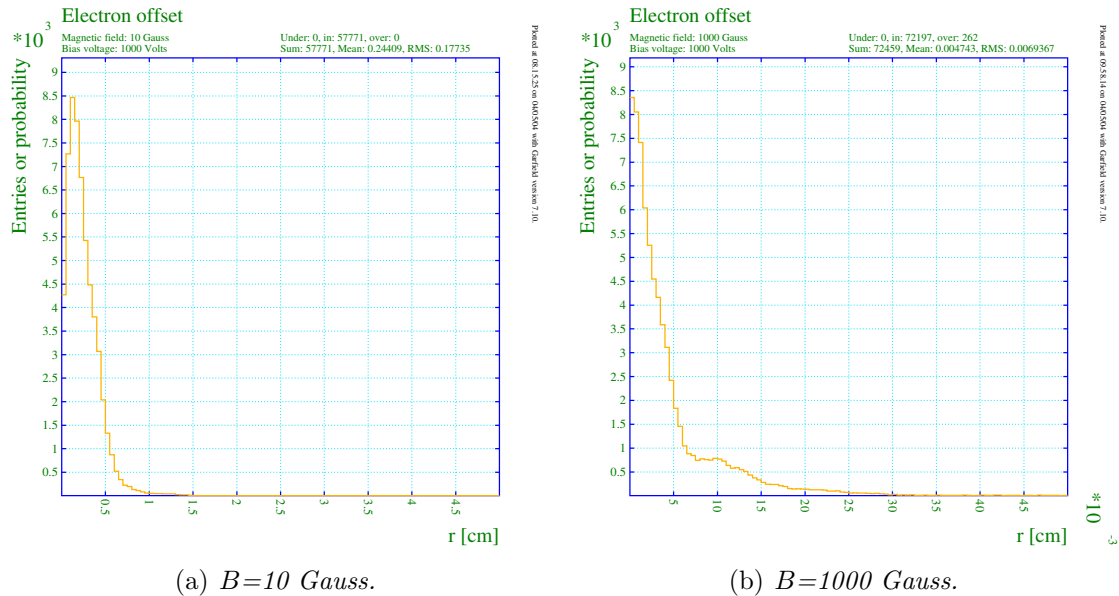


Figure 3.13: *The offset of the electrons in the image plane after drifting from the wires to the MCP at low and high magnetic fields.*

Table 3.3 gives mean and RMS values for the offset for different magnetic fields. 1 Gauss is chosen in the table in stead of 0 Gauss, as the radius of the cyclotron motion is inversely proportional to the magnetic field, and comparing

the value for 0 Gauss with theoretical values would therefore give a meaningless result, see Eq. 2.38.

<b>B-field</b>	<b>Mean offset [mm]</b>	<b>RMS [mm]</b>
1 G	2.42	1.57
10 G	2.44	1.77
27 G	2.19	2.02
100 G	0.619	0.726
1000 G	0.0474	0.0693

Table 3.3: *The electron offset in the image plane (xz-plane) for electrons emitted from heated wires at different magnetic fields.*

The data presented in this section shows that best results for an emitting wire grid are obtained at low magnetic fields, but that these results nevertheless are poor. Even at low fields the intensity variations are unacceptably large, and significant edge effect occur. These figures indicate the need for a much more sophisticated electron source in order to obtain useful results.

### 3.3.3 IPM with EGP

The original model of the IPM was modified again, this time to include a model of the EGP from Burle, Inc. The operating principle was outlined in the introduction, see Fig. 1.7. The emitting face of the EGP was placed in the same position as the wires, i.e. 6 mm above the cathode grid. Fitting the EGP in this position also required some modifications to the cathode and the shielding ground plate. Some rounding of the edges of both the EGP frame and the cathode were include in the model to prevent distortion of the field near the edges, while other minor features were left out to simplify the calculations. In the model the entire EGP was assumed to be metal. This assumption is valid as the field inside and above the EGP is of no interest to the simulation of the field in the drift volume. The exact technical drawings which the model tries to imitate, are given in Appendix B. The technical drawings were made by Giuseppe Foffano preceding the experiments which will be discussed in the next chapter. The modified region of the IPM is shown in Fig. 3.14.

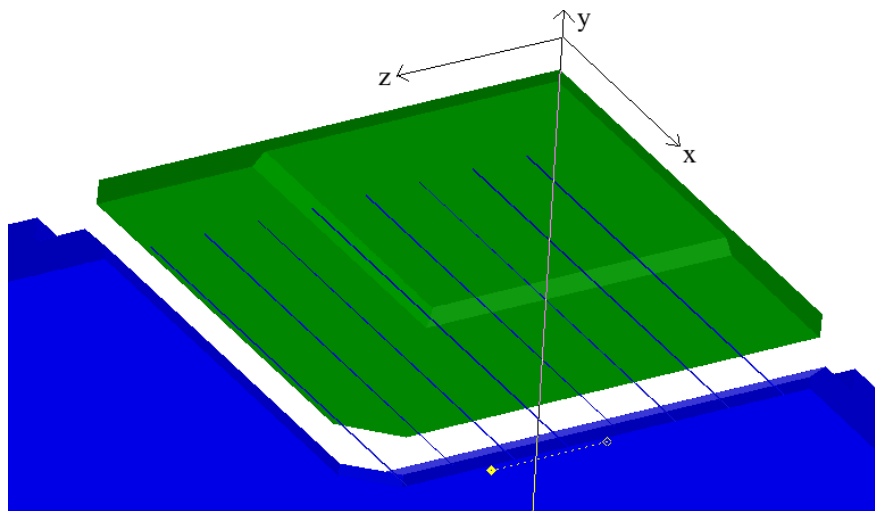


Figure 3.14: *The modified part of the IPM, viewed from below. An EGP is introduced above the cathode grid, in addition to some small modifications of the cathode.*

The potential of the EGP relative to the cathode was adjusted to create an electric field as homogenous as possible, in the same ways as for the emitting wire grid. The resulting electric field is shown in Fig. 3.15. The view is the same as for the computations with the emitting wire grid.

The plots show a quite homogenous field, except for some small edge effects at the corners of the EGP. This is caused by the frame of the EGP having the same potential as the EGP it self, but extending further down into the volume. The rounded edges of the frame and cathode limit this effect to some extent.

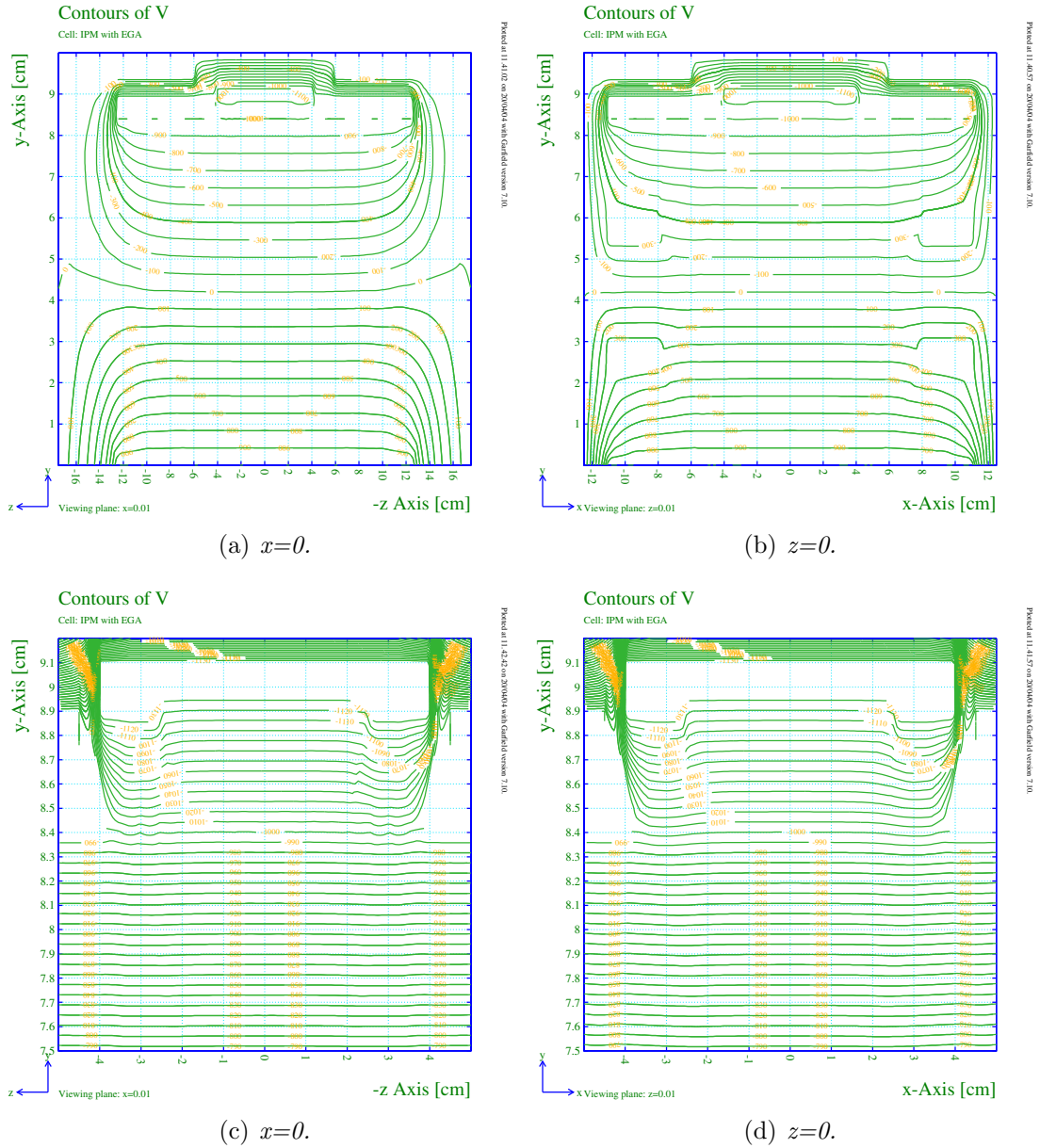


Figure 3.15: *The electric field in calibration mode with an EGP integrated in the IPM. Cuts are made through the centre of the volume, but the view is chosen a small distance away from the axis, to suppress numerical inaccuracy near the edges of the simulation. (a) and (b) show the entire volume, while (c) and (d) present enlarged plots of the region near the cathode grid.*

The initial conditions of the emitted electrons were described in Section 2.4.2, and typical resulting energy and velocity distributions from the Garfield program

### 3.3. RESULTS OF THE SIMULATIONS

are given in Fig. 3.16. From the graphs, it is clear that also for emission from EGPs the spread in initial energy and velocity is large.

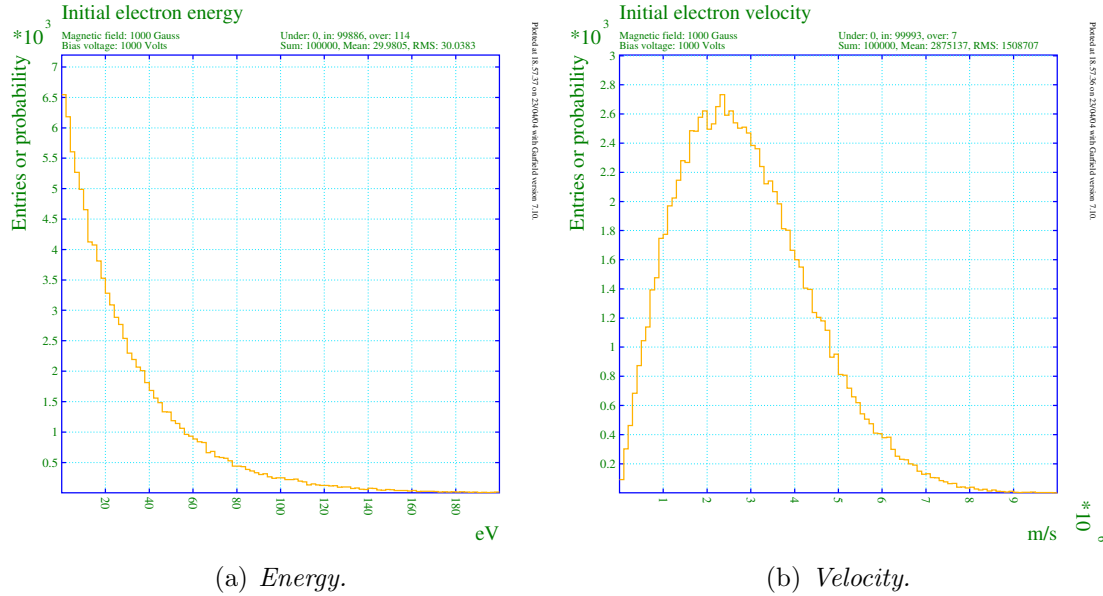


Figure 3.16: Typical distributions of initial energy and velocity of the electrons emitted from the EGP, simulated with the Garfield program.

The resulting initial electron distribution at the EGP is given in Fig. 3.17. The initial positions of the electrons are uniformly randomly distributed. The resulting distribution is therefore close to uniform, but with some random fluctuations.

The drift time of the electrons from the EGP to the MCP was also calculated. A histogram of the results is given in Fig. 3.18. The mean drift time is 5.9 ns, with a FWHM of about 0.8 ns. This value is somewhat lower than the estimate of 6 to 7 ns, due to the more significant initial energy.

The path of some hundred electrons are plotted in Fig. 3.19 for a typical low and high magnetic field, respectively. At low magnetic fields, the edge distortion of the electric field is evident. At high magnetic fields, this effect is suppressed.

More detailed simulations were done, calculating the path of  $10^5$  electrons at magnetic fields from 0 to 1000 Gauss. Typical resulting electron distributions at the MCP are shown in Fig. 3.20 for low and high magnetic fields. These figures confirm what was indicated by the plot of the drift lines, at low fields substantial edge effects occur. In addition, a pattern caused by the cathode grid wires can be seen. This pattern disappears, along with the edge effects, at high fields.

A more detailed description of the results is presented in Table 3.4. The numbers in this table are generated by considering the difference in the electron

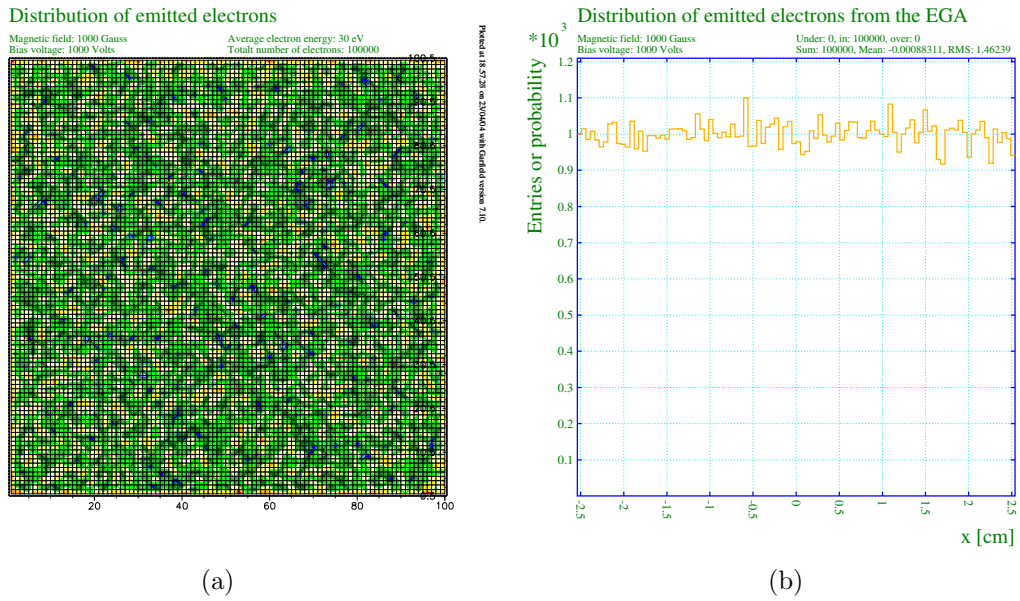


Figure 3.17: *Simulated distributions of emitted electrons from the EGP. (a) Area shown is 5.08 cm by 5.08 cm, the active area of the EGP. The colour indicates the intensity of the electron distribution. (b) The intensity projected onto the x-axis. The distribution is assumed to be homogenous, but random fluctuation occur.*

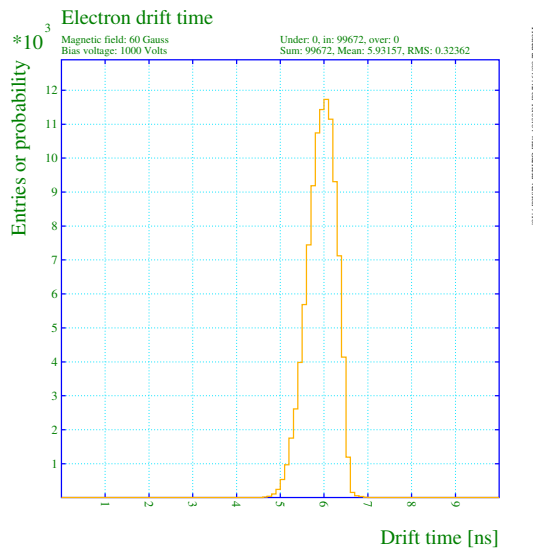


Figure 3.18: *A histogram of the drift time for the electrons from the EGP to the MCP.*



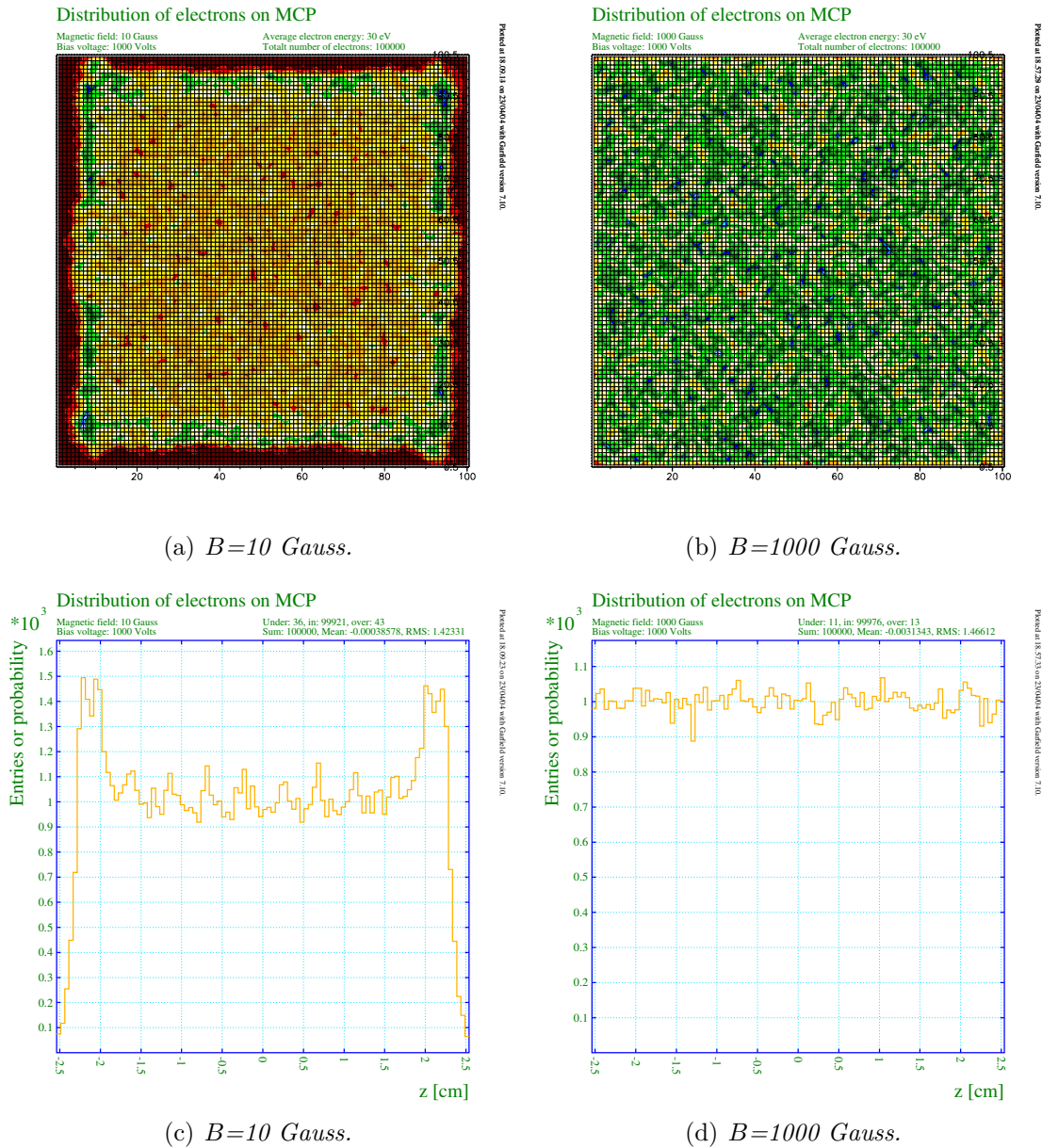


Figure 3.20: *The resulting electron distribution on the MCP from simulations of electrons emitted from an EGP. The area shown is 5.08 cm by 5.08 cm, the size of the MCP, the resolution is 508  $\mu\text{m}$ . Notice how the grid wires of the IPM cause distortion of the distribution at low fields.*

caused by these may still be significant even though no effect is visible for a magnetic field of 1000 Gauss at a resolution of 508  $\mu\text{m}$ . To investigate this matter, a simulation with a resolution of 5  $\mu\text{m}$  was made for a small part of the

B-field	Distortion	Cross-section	Edge dist.
0 G	16 %	3.0 cm	90 %
10 G	16 %	3.6 cm	90 %
60 G	8 %	4.0 cm	22 %
100 G	6 %	4.2 cm	32 %
1000 G	2 %	5.1 cm	-

Table 3.4: *Distortion of the initial electron distribution emitted from the EGP after drifting through the IPM at various magnetic fields. The cross-section is the width of the area without edge effects. The values for the distortion are given for this area, while the last column gives the distortion in the area where the edge effects are significant. Spatial resolution used for these computations is 508  $\mu\text{m}$ .*

IPM around one wire. The results are shown in Fig. 3.21. These simulations show that shadow effects are indeed evident at a magnetic field strength of 1000 Gauss. The width of the shadow is approximately the same as the width of the wire, and in this area the number of electrons reaching the MCP is reduced by up to 50%.

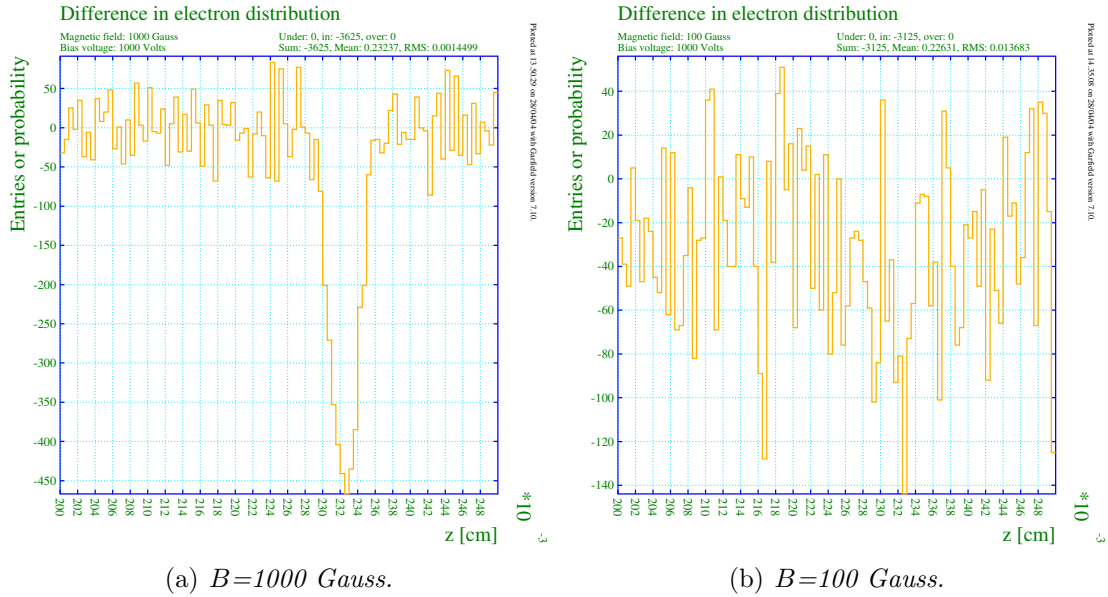
These results coincide with the values computed for the electron offset, the shift in position in the image plane ( $xz$ -plane), resulting from the drift through the chamber. Histograms for the electron offset at low and high magnetic fields are given in Fig. 3.22. More details are given in Table 3.5.

B-field	Mean offset [mm]	RMS [mm]
1 G	1.25	1.30
10 G	1.19	1.21
60 G	0.0979	0.108
100 G	0.231	0.240
1000 G	0.0148	0.0149

Table 3.5: *The electron offset in the image plane ( $xz$ -plane) for electrons from the EGP at different magnetic fields.*

These values should be compared to the resolution limit of the system. The centre-to-centre spacing of the channels of the MCP, which can be used as a measurement for its resolution, is 32  $\mu\text{m}$ . [11] This is the ultimate resolution limit of the imaging system, however the resolution of the camera in use limits the resolution further.

The camera has a pixel size of 20 (horizontal) by 30 (vertical)  $\mu\text{m}$  [33]. The demagnification of the optical system is theoretically 0.1924 [25], so that transposed on the phosphor screen one pixel will correspond to an area of about 104 by 156  $\mu\text{m}$ . Consequently, the size of the area exposed to the shadow of the shielding wires at a magnetic field of 1000 Gauss is smaller than the resolution of


 (a)  $B=1000$  Gauss.

 (b)  $B=100$  Gauss.

Figure 3.21: (a) Simulations with a resolution of  $5 \mu\text{m}$  show that the shielding grid wires create shadows at the MCP at  $B=1000$  Gauss. The FWHM of the shadow is  $40 \mu\text{m}$ , while the diameter of the wires is  $50 \mu\text{m}$ . The centre of the wire is situated at  $z=2325 \mu\text{m}$ , corresponding to the centre of the shadow. In comparison, the resolution of the MCP is about  $30 \mu\text{m}$ . (b) The shadow effect is not clearly distinguishable at 100 Gauss. (Note that both plots show differences in electron distributions, so that the shadow results in negative "Entries of probability".)

the imaging system. In other words, the simulations indicate that with a magnetic field of 1000 Gauss, the shadow effect from the cathode grid will be small, if at all detectable with the imaging system in question, as the low resolution will average out the effect. Since the pixel size is 2-3 times the size of the shadow, the magnitude of the shadow will be decreased by a factor of at least 2-3 compared to what is shown in Fig. 3.21.

The modifications made to the IPM in order to implement the calibration system, may influence the IPM during normal beam measurement operation. The next section will discuss changes to the electrical field and other possible effects caused by implementations of an EGP.

### 3.3. RESULTS OF THE SIMULATIONS

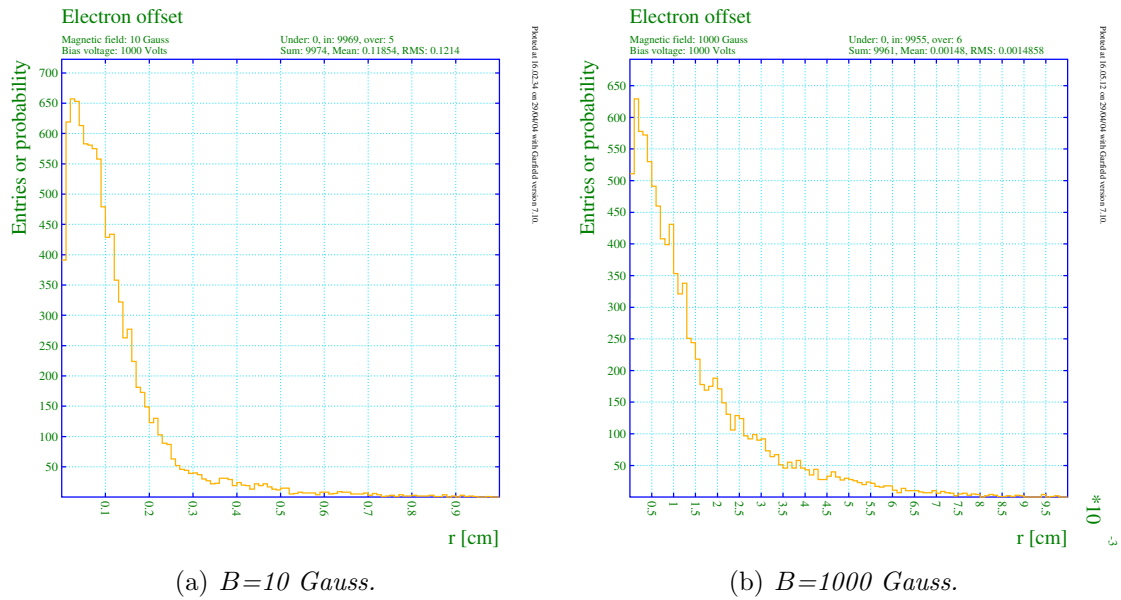


Figure 3.22: The offset of the electrons in the image plane after drifting from the EGP to the MCP at low and high magnetic fields.

### 3.3.4 The new design in operation mode

It is vital that the implementation of a calibration system does not decrease the IPMs performance during beam profile measurements, by causing further distortion to the electric field. The electric field of the original IPM was presented in an earlier section, see Fig. 3.5, and this should be compared to the results obtained in this section. As described in Section 1.1, the function of the cathode wire grid is to prevent secondary emission of electrons due to ions hitting the surface above the MCP. However, as can be seen from the field maps, the wires inevitably cause a distortion to the field, primarily in the upper part of the IPM. This distortion is caused by the large potential difference between the cathode grid and the shielding ground plate directly above it.

When the EGP is introduced between the cathode grid and the ground plate, it is the potential difference of the EGP and the cathode grid that will determine the distortion of the field. By adjusting the potential of the EGP, the potential difference during operation mode can be tuned such that the distortion of the field is made as small as possible, while still having a sufficient field to capture the secondary electrons.

As an example, it is worth noting that measurements suggest that the energy of the secondary electrons from singly charged ions impinging on clean tungsten is less than 20 eV [34]. Consequently, a potential difference of almost 1000 V is then probably far more than necessary to trap such electrons. In addition, all surfaces of the IPM, including the MCP, are treated with a special coating to reduce secondary emission [35, 36]. If necessary, this type of coating may also be applied to the EGP.

These considerations indicate that it should be possible to reduce the potential difference between the EGP and the cathode, and thereby in fact *improve* the homogeneity of the electric field, without increasing the number of secondary electrons escaping into the chamber. This possibility should be verified experimentally, by varying the potential difference during operation of the IPM.

In this way, the implementation of the EGP may in fact improve the performance of the IPM also during operation mode. As a first approach, the potential of the EGP is for simplicity chosen to be the same as in calibration mode (-1143 V), however the potential of the electrodes are raised to  $\pm 2000$  V. With this configuration, the field in the IPM will be close to that of the original configuration. To be able to fit the EGP in the IPM, the ground shielding plate (the wall of the tank) had to be modified, as well as the upper side of the negative electrode. Technical drawings of the modifications are shown in Appendix B. The resulting field is shown in Fig. 3.23. The plot shows that implementing the EGP, using the potential settings suggested above, gives an electric field close to, or more homogenous, than the field of the original IPM.

This chapter has shown that, according to simulations, a calibration system based on an EGP looks quite promising. It also indicates that such a system

### 3.3. RESULTS OF THE SIMULATIONS

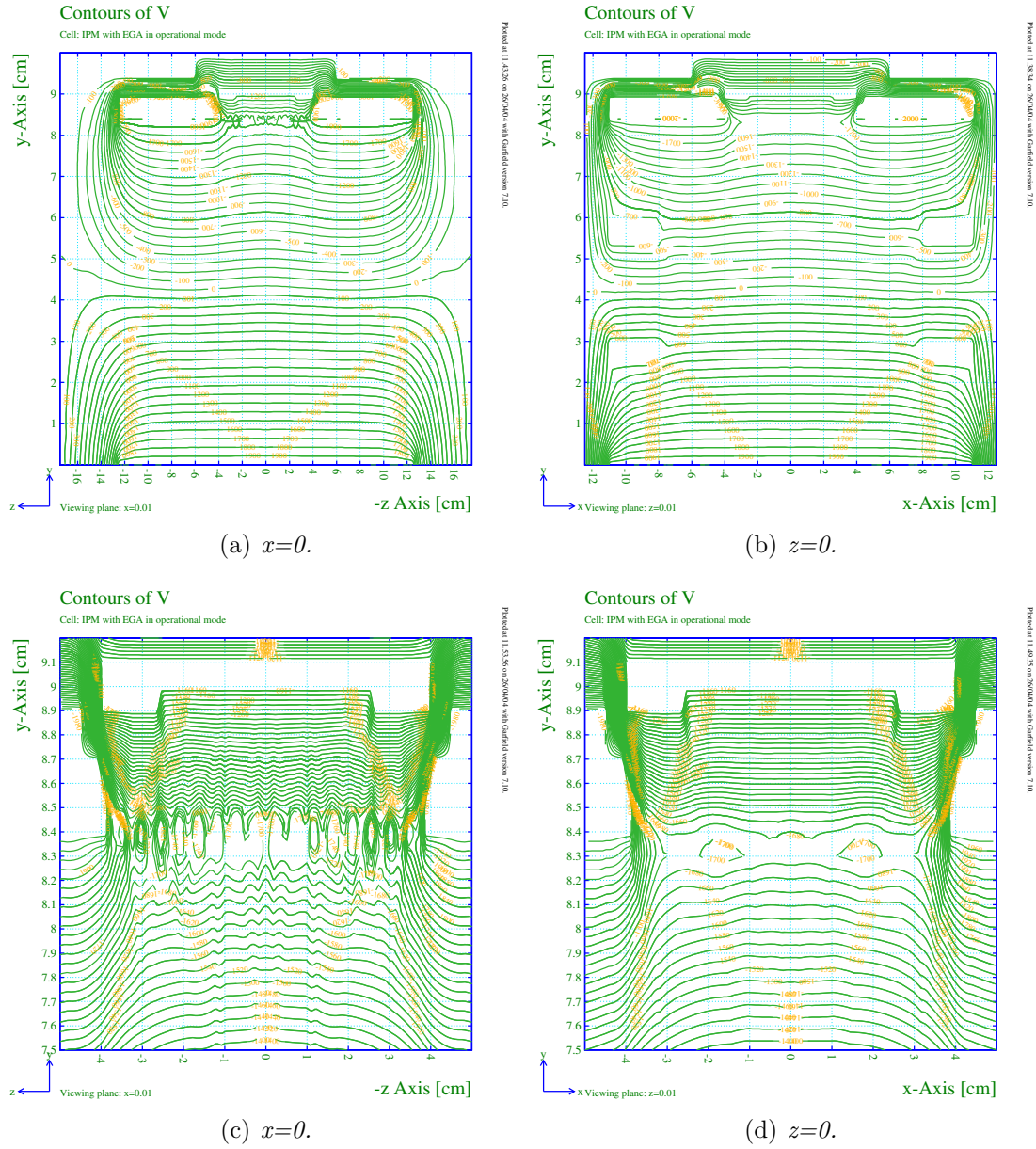


Figure 3.23: The electric field in the IPM in operation mode with the EGP implemented. Cuts are made through the centre of the volume, but the view is chosen a small distance away from the axis, to suppress numerical inaccuracy near the edges of the simulation. (a) and (b) show the entire volume, while (c) and (d) present enlarged plots of the region near the cathode grid. The beam passes in direction of the  $z$ -axis.

could be implemented without disturbing the normal operation of the IPM. To

verify this, a prototype of the calibration system, implementing an EGP, was build. The next chapter will describe the experiments and measurements which were carried out with this setup.

# Chapter 4

## Experiments

In the following chapter, a description of the experiments carried out will be given. The setup will be discussed first, while the results are given in the last section. Some additional simulation results, which include measured values, are also included.

Some experiments, using a heated wire as an electron emitter, have previously been conducted [2]. At first these results were believed to be promising, but later investigations have shown that the published results were erroneous. The main problem encountered in these measurements was saturation of the MCP, due to too high intensity of emitted electrons [25]. In addition, and in accordance with the simulations presented in this thesis, a satisfactory homogeneity of the electron emission seems impossible to obtain using a simple wire grid as electron emitter.

Consequently, no further experiments were conducted with a heated wire as the electron source. Experiments were however carried out using an EGP, from Burle, Inc., as the electron source.

### 4.1 Setup

An IPM was modified to include the EGP above the cathode grid, according to the principle outlined in the introduction, see Fig. 1.7. The emitting face of the EGP was placed 6 mm above the wire grid, after modifying the cathode. Detailed technical drawings of the modifications done to the cathode are given in Appendix B. A simplified schematic of the high voltage connections is given in Fig. 4.2. The voltages applied to the different inputs vary for the different measurements.

The IPM was then mounted in a special test vacuum tank in a laboratory at CERN. After the vacuum pump had been running for one week, a pressure of about  $6 \times 10^{-6}$  mbar was obtained. The pressure was found to vary slightly during the time used for the measurements, with pressures of between 5.7 and  $6.3 \times 10^{-6}$  mbar being recorded. However, the pressure could not be recorded

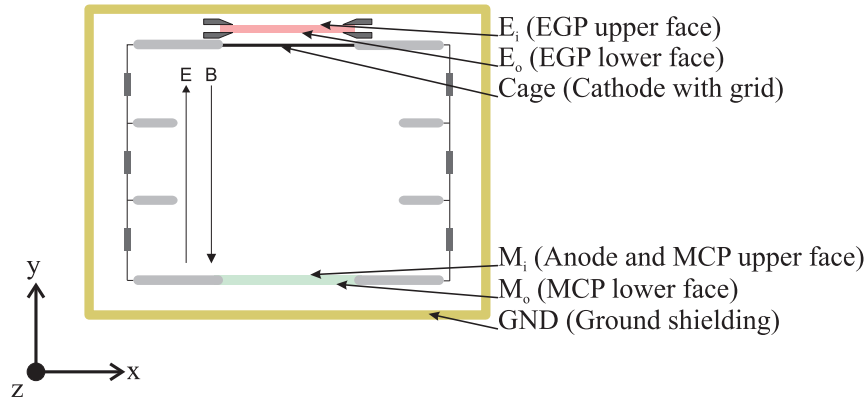


Figure 4.1: *Schematic of the high voltage connections.*

at the same time as the measurements were done, because the pressure gauge emitted electrons which greatly disturbed the image at the MCP. In comparison, a pressure of  $10^{-8}$  to  $10^{-6}$  mbar is used in the SPS during operation [37]. For optimal performance of the MCPs, a pressure of  $10^{-6}$  mbar is recommended [38].

In contrary to the installation in the SPS, no electromagnet was available in the laboratory setup. The experiments were therefore conducted assuming close to zero magnetic field.

A *L3C65 Series Low Light CCD Camera* from e2v technologies, inc. [33] was used to acquire images of the resulting intensity at the phosphor screen. The camera had previously been used during operation in the SPS, and suffered from some radiation damage. The radiation damage caused some noise to the pictures, visible as bright spots.

A picture of the laboratory setup is shown in Fig. 4.2. The picture shows the vacuum tank with the camera mounted on top. The tube in the lower left corner is connected to the vacuum pump. Measuring electronics, high voltage supplies, and a monitor for viewing the image from the camera, can be seen in the background.

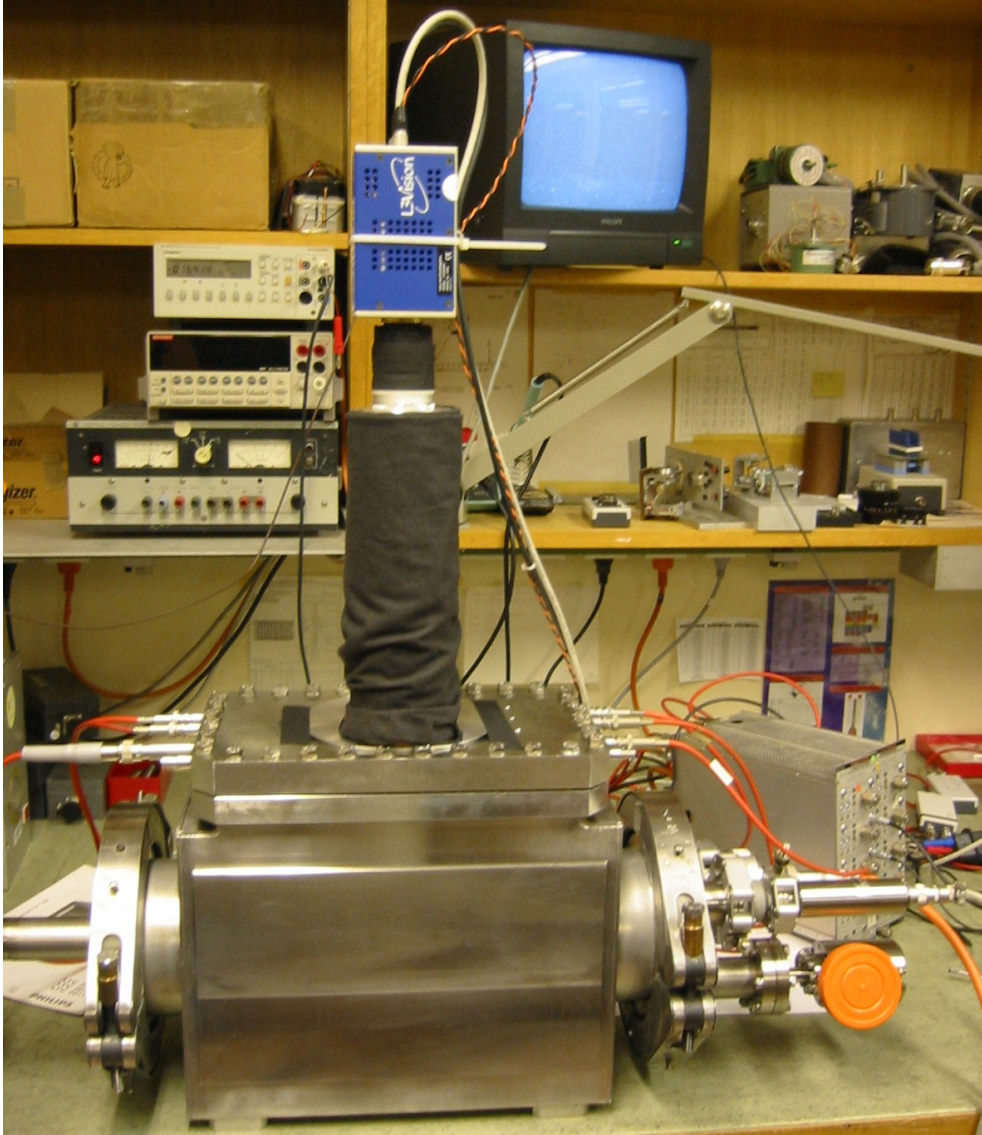


Figure 4.2: *Photo of the laboratory setup.*

## 4.2 Results

Before any high voltage was applied, the impedances through the MCP, the EGP, and between the cathode and anode, were measured. The results are given in Table 4.1.

Measured connectors	Impedance $M\Omega$
$M_i$ to $M_o$ (MCP)	13.0
$E_i$ to $E_o$ (EGP)	4.5
$M_i$ to Cage (Resistors and electrodes)	6.6

Table 4.1: *Measured impedances of the IPM.*

The impedance of the MCP, together with the applied voltage, can be used to determine bias current of the MCP. Knowledge of this value will give a more accurate estimate for the threshold of saturation effects in the MCP, see Section 2.4.3.

Before any measurements with the EGP were done, the voltage applied to  $M_i$  was set to 1000 V, Cage to was set to -1000 V, and  $M_o$  was varied between 1000 and 2000 V. In this way, the voltage applied to the MCP was varied from 0 to 1000 V. No background noise from the MCP was found, even at the highest gain.<sup>1</sup> However, as mentioned above, some noise was induced by radiation damage to the camera.

When voltage was applied across the EGP, the MCP lit up. A voltage across the MCP and EGP (gain) of about 600 V was found to give suitable intensity of the image recorded on the camera. If the MCP is operated at this value, the MCP bias current will be

$$I_{bias} = \frac{600 \text{ V}}{13.0 \text{ M}\Omega} = 46 \times 10^{-6} \text{ A.} \quad (4.1)$$

As noted in Section 2.4.3, saturation effects start to occur when the electron current reaches about 10% of this value, that is  $1.8 \times 10^{-7} \text{ A/cm}^2$ .

The voltages of the IPM were then set to the values used for the simulations, that is  $M_i = 1000 \text{ V}$ ,  $\text{Cage} = -1000 \text{ V}$ , and  $E_o = -1143 \text{ V}$ .  $M_o$  and  $E_i$  were set to 1600 V and -1743 V, respectively, so that the gain of both plates was 600 V. With this configuration stripes, caused by the cathode grid, were clearly visible. By adjusting the Cage voltage to  $-1163 \pm 1 \text{ V}$ , these stripes were found to disappear. However, if either of the voltages were changed by just a few volts, the wire pattern reappeared. An example of this phenomena is shown in Fig. 4.3. It should be noted however, that the sensitivity to changes in the electric field,

<sup>1</sup>When the pressure gauge was switched on, substantial background noise was recorded when a voltage of more than 400 V was applied across the MCP.

are expected to be less if a magnetic field is applied. The reason for this is, as explained in Section 2.2.2, that the magnetic field will constrain the movement of the electrons.

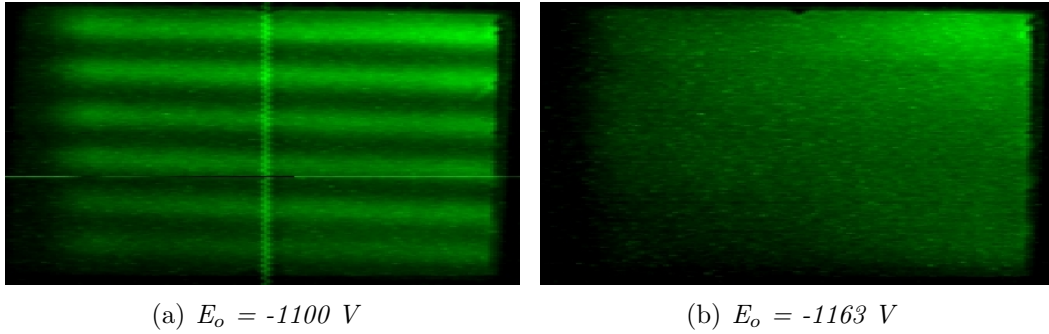


Figure 4.3: *The effect of changing the voltage applied to  $E_o$  is clearly seen by the wire pattern shown in (a) disappearing in (b).  $M_i = 1000$  V and  $C_{age} = -1000$  V is used, as well as a gain of about 600 V for the EGP and MCP. The cross shown in (a) is for alignment, and produced by the acquisition electronics.*

When the potentials were adjusted so that the wire pattern disappeared, and a reasonable value for the gain of the plates was used, it was expected that the image of the intensity at the MCP, shown in Fig. 4.3 (b), would be flat. This was however not the case. The corresponding profiles of the  $z$ - and  $x$ -direction of the image acquired are shown in Fig. 4.4.

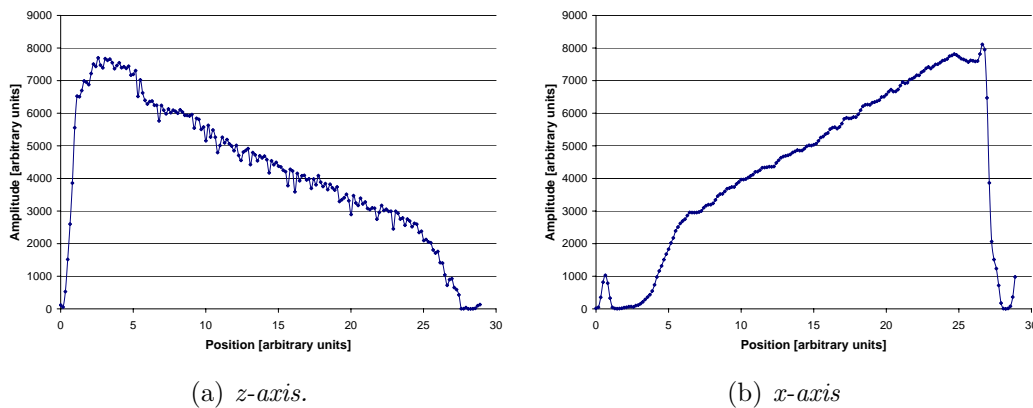


Figure 4.4: *Profiles of the intensity distribution at the MCP. (a) Along the  $z$ -axis, and (b) along the  $x$ -axis.*

The figure shows that the intensity increases towards the upper right corner. To check that it was not the camera causing this effect, the camera was turned i

various ways. However, no significant changes in the recorded intensity pattern could be detected.

The impedance of the resistors connecting the lateral electrodes were measured during the assembly of the IPM [25]. The values were measured both with 500 V applied and without applied voltage. The values are given in Fig. 4.5.

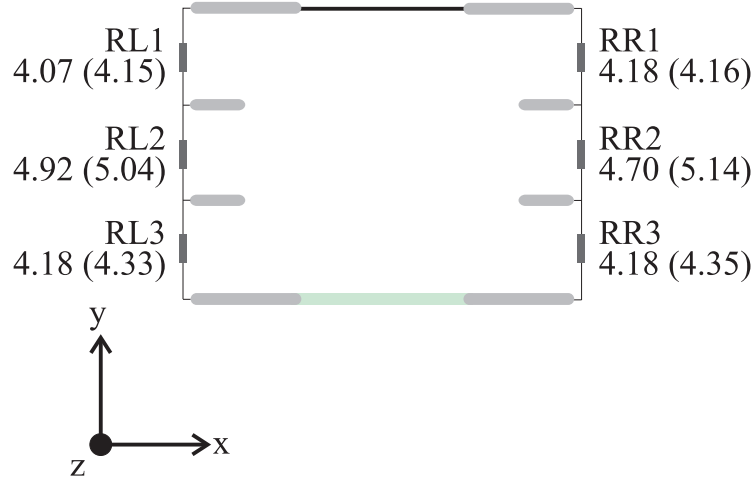


Figure 4.5: Measured impedance values for the resistors when applying 500 V. Values without voltage applied in parenthesis. All values are in  $M\Omega$ .

The values were found to differ noticeably from the desired values, and this could cause some perturbations to the electric field. Perturbations to the electric field could also cause perturbations to the electron distribution. However, considering the symmetry of the IPM, only variations in the x-direction (horizontally in Fig. 4.3) would be expected in the electron distribution. The measured values of the resistors, together with the measured value of  $E_o$  when the wire pattern disappeared, were used to more accurately simulate the electric field in the IPM. The result is shown in Fig. 4.6.

As expected, the figure shows some perturbations of the field along the x-direction. To see if this affected the electron drift, the same drift algorithm as was used for the previous simulations, was used to simulate electron drift through the IPM. However, no significant changes to the electron distribution were found. This indicates that the variations in the resistor values should not affect the intensity at the MCP significantly.

For all the simulations of electrons emitted from the EGP done so far in this thesis, it has been assumed that the electrons were emitted at a random angle between  $-5^\circ$  to  $+5^\circ$  from the normal of the EGP. The channels of the EGP are however specified to have a bias angle of  $8^\circ \pm 1^\circ$ . This means that it is more probable that the electrons are emitted in a certain direction than others. The

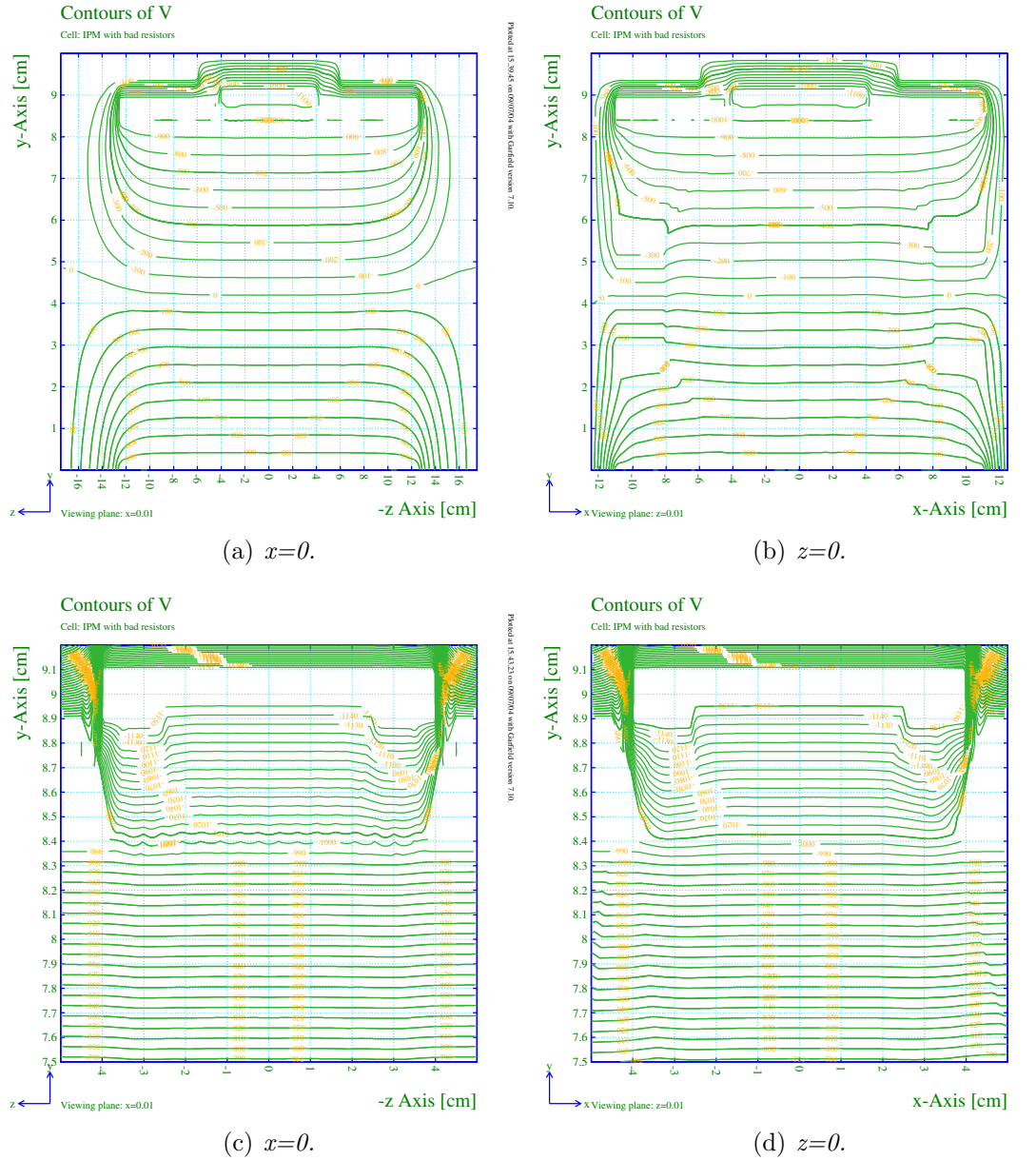


Figure 4.6: Equipotential lines of the simulated electric field in the IPM, with measured values used for the resistors and for  $E_o$ . Some perturbations to the field can be seen in the  $x$ -direction. Cuts are made through the centre of the volume, but the view is chosen a small distance away from the axis, to suppress numerical inaccuracy near the edges of the simulation. (a) and (b) show the entire volume, while (c) and (d) present enlarged plots of the region near the cathode grid.

angle of which the electrons are emitted is important a low magnetic field, as in

our experimental setup. A new simulation, where the electrons are emitted at an angle of  $8^\circ \pm 1^\circ$ , was therefore done, using the electric field shown in Fig. 4.6. The results are shown in Fig. 4.7 and 4.8.

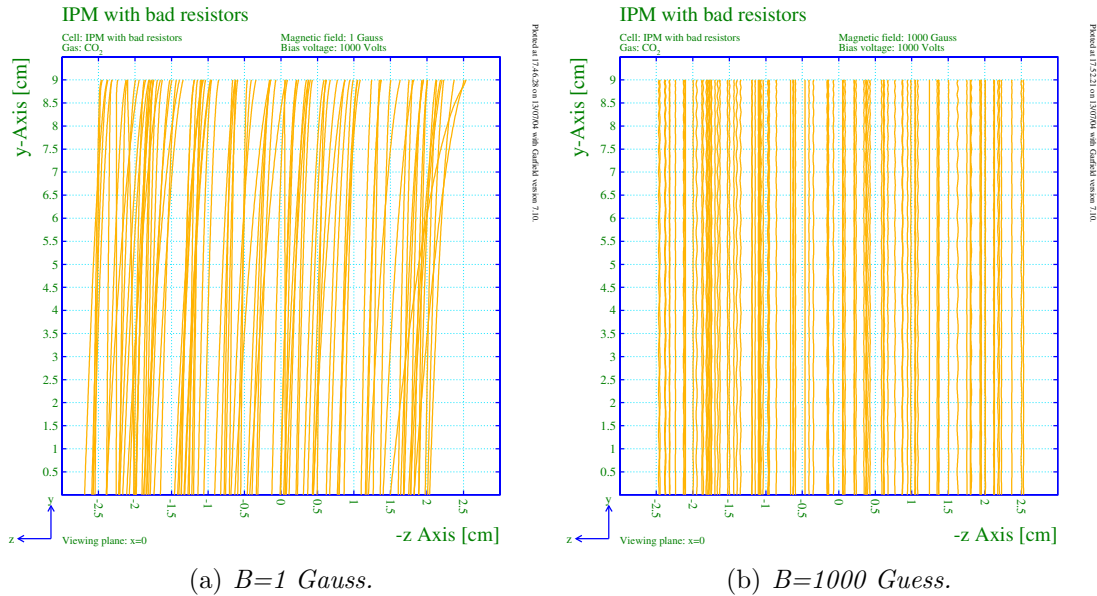


Figure 4.7: Drift lines for electrons emitted from the EGP at high and low fields, assuming electrons are emitted at an angle of  $8^\circ \pm 1^\circ$ . Note that the Garfield program for some reason uses  $-z$  in stead of  $z$  as the horizontal axis.

The plots clearly indicate that the electron distribution is shifted sideways at low magnetic fields, because the electrons are emitted at a biased angle. The edge effects of the field (see Fig. 4.6), direct the electrons, which would otherwise arrive outside the MCP, back in. This effect causes the inclining intensity towards one corner, as was seen in the experiments. As seen in Fig. 4.7 (b) and 4.8 (b), the effect is suppressed at a high magnetic field. The edge effects observed in the simulations, and the effects of the wires, are noticeably greater than those observed in the experimental setup.

More test should be conducted in an environment where a magnetic field is available, as further conclusions about the homogeneity of the electron distribution at the MCP cannot be given with the current experimental setup.

During operation of the IPM a voltage difference, between  $E_o$  and Cage, would be applied to stop any secondary electron from returning into the drift volume of the IPM, see Section 3.3.4. The secondary electrons are assumed to have lower energy than the electrons emitted when a voltage is applied across the EGP. Consequently, a repelling voltage high enough to stop electrons emitted from the EGP, should also stop any secondary electrons.

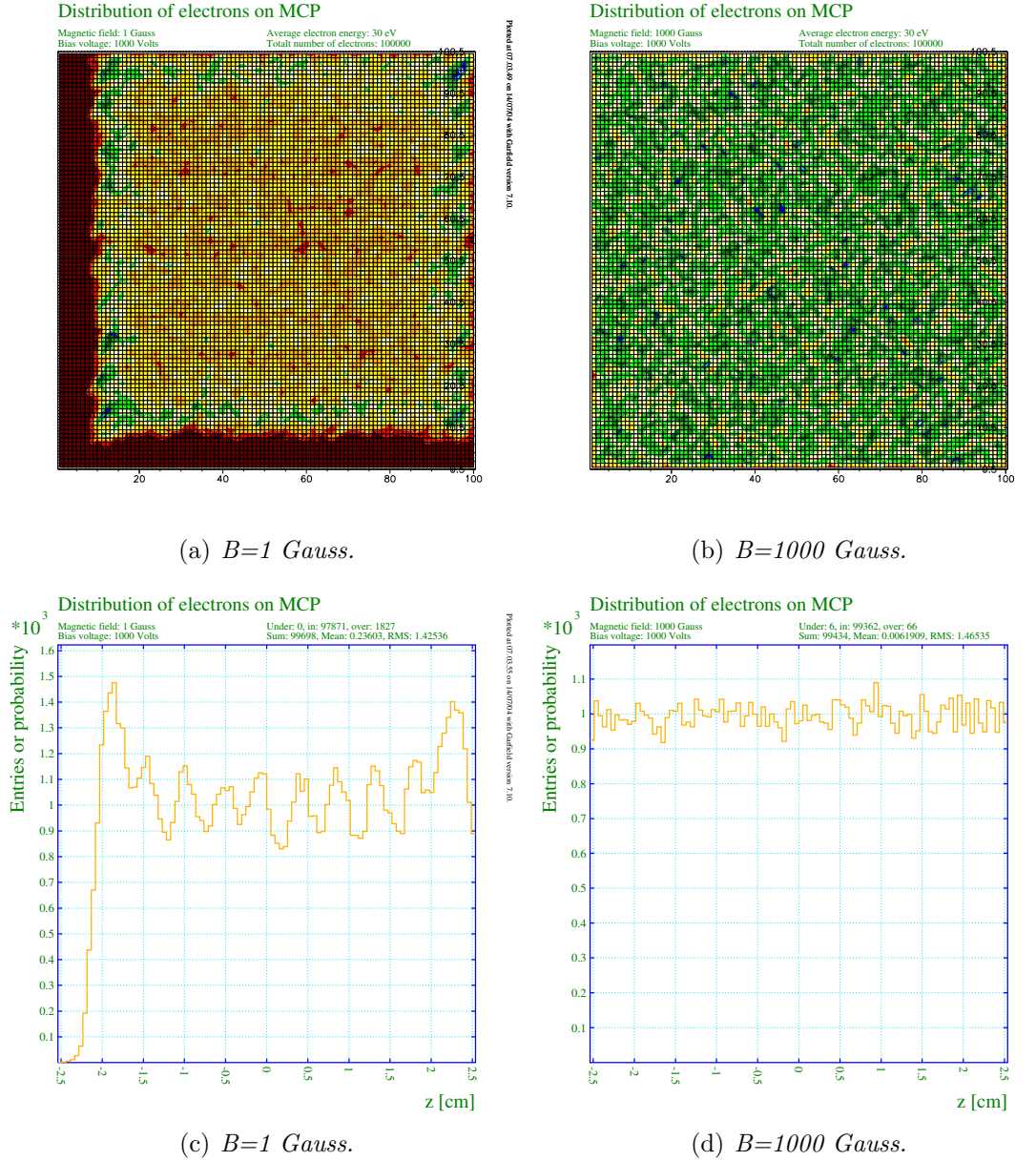


Figure 4.8: The resulting electron distribution on the MCP from Garfield simulations of electrons emitted at an angle of  $8^\circ \pm 1^\circ$  from the EGP. The area shown in (a) and (b) is 5.08 cm by 5.08 cm, the size of the MCP. In (c) and (d), the projection onto the z-axis is shown.

Voltages typically used during operation,  $M_i = 2000$  V,  $M_o = 2600$  V, and Cage = -2000 V, were applied to the IPM.  $E_i$  and  $E_o$  were varied, so that the gain of the EGP varied from 400 V to 800 V. For each gain setting,  $E_o$  was adjusted

so that the retarding potential between,  $E_o$  and Cage, was just enough to stop all the emitted electrons. The repelling voltage required to stop the electrons, as function of the gain of the EGP, is plotted in Fig. 4.9.

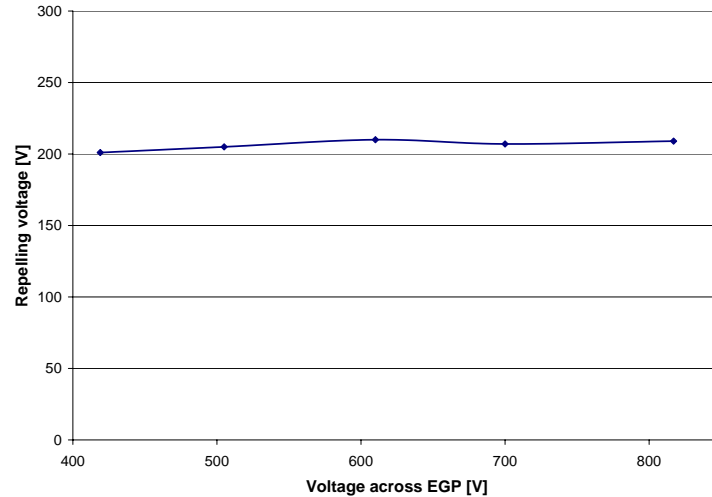


Figure 4.9: *The required voltage to stop the electrons emitted from the EGP, as function of the EGP gain.  $M_i = 2000$  V and Cage = -2000 V was used.*

The figure shows that a potential difference of a little more than 200 V is required to stop all electrons emitted from the EGP, regardless of the EGP gain. Consequently, it should be sufficient to keep the EGP at a voltage of a little more than 200 V below the Cage during operation. Keeping the EGP at this voltage, would improve the homogeneity of the field in the IPM during beam profile measurements, compared with the field configuration in use today.

A plot of the simulated electric field for the IPM in operation mode, with a potential difference between the EGP and Cage of 300 V, is shown in Fig. 4.10. The figure should be compared to Fig. 3.5, and shows that this configuration is more homogenous than the one used today.

A similar experiment was conducted to determine the average energy (in the y-direction) of the electrons emitted from the EGP. A gain of about 700 V was used for the MCP, while the gain of the EGP was varied between 300 V and 800 V. A potential difference, between Cage and  $M_i$ , of 3-400 V was used to guide the electrons to the MCP. The retarding potential needed between  $E_o$  and Cage, to stop an electron, is assumed to be equivalent to the electron's energy in eV. A plot of the electron energy as a function of EGP gain, is shown in Fig. 4.11. The values recorded, are those needed to stop nearly all electrons. Consequently, if the energy distribution is exponential, the recorded values will be higher (closer to the tail of the distribution) than the average electron energy.

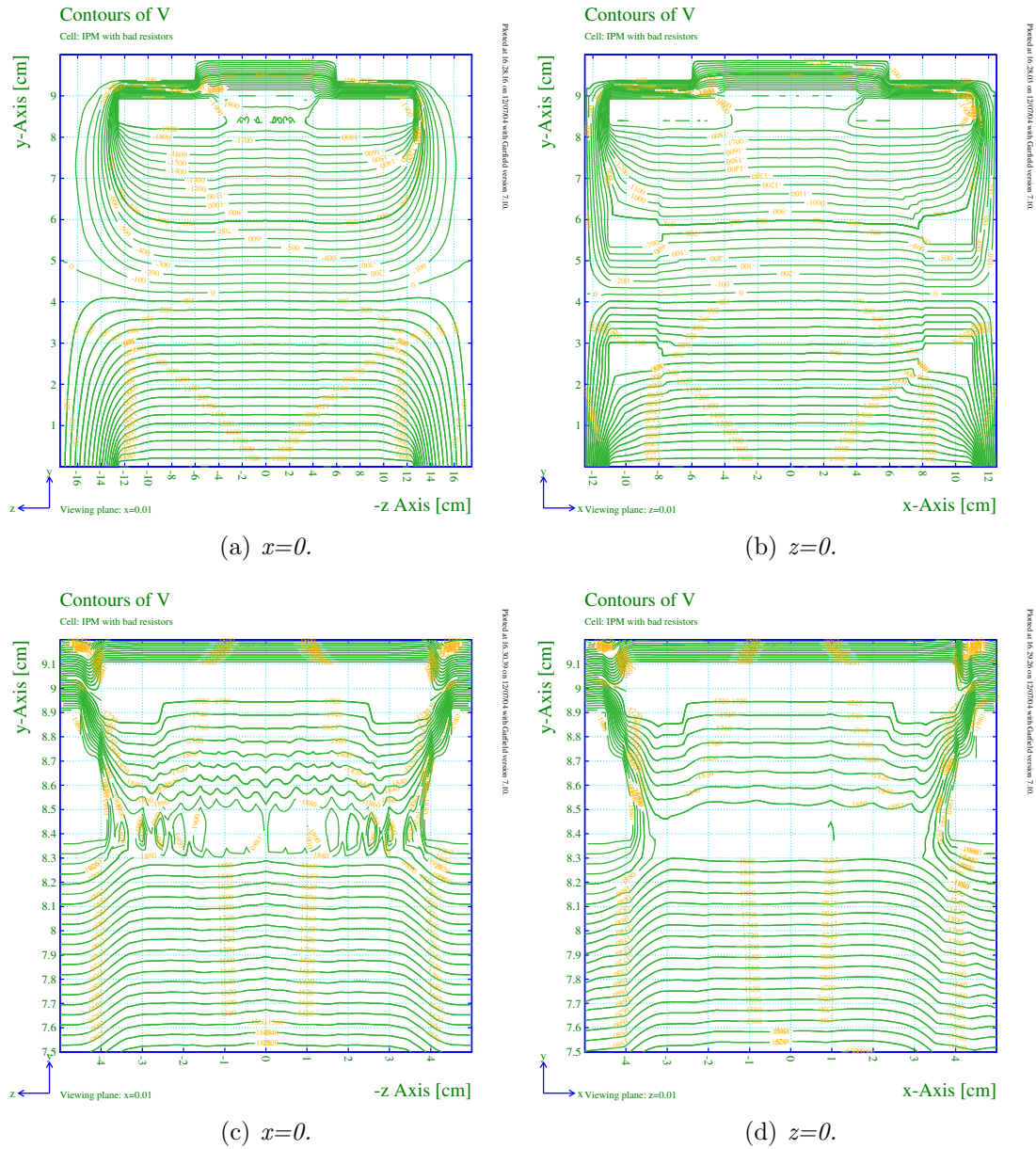


Figure 4.10: Equipotential lines of the simulated electric field in the IPM during operation mode. The measured values for the resistors are taken into account. The potential settings used are  $E_o = -1700$  V,  $C_{age} = -2000$  V, and  $M_i = 2000$  V. Cuts are made through the centre of the volume, but the view is chosen a small distance away from the axis, to suppress numerical inaccuracy near the edges of the simulation. (a) and (b) show the entire volume, while (c) and (d) present enlarged plots of the region near the cathode grid.

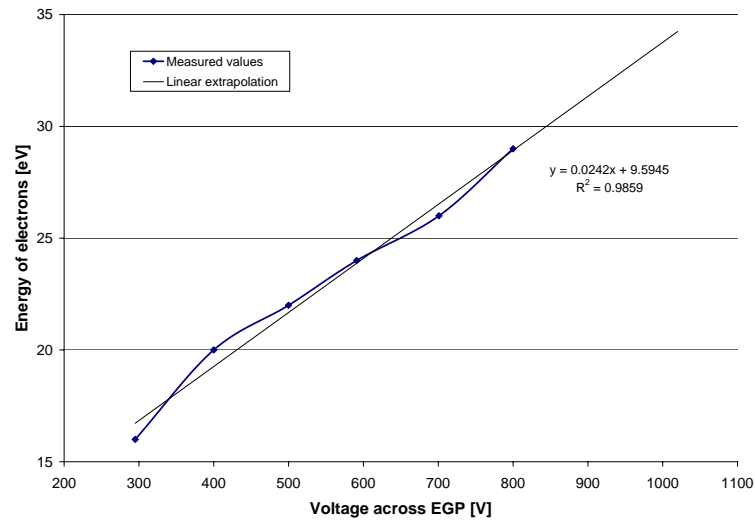


Figure 4.11: *The energy of the electrons emitted from the EGP, as a function of EGP gain. A potential difference of only 3-400 V between Cage and  $M_i$  was used to guide the electrons to the MCP.*

The figure shows a linear relationship between the applied voltage and the electron energy. From fear of damaging the costly EGP, it was never operated at full gain. However, a linear extrapolation to higher gain values is included in the graph. From the graph, electron energies from 16 eV to 34 eV is found when varying the EGP gain from 300 V to 1000 V. The average electron energy is expected to be somewhat lower. In the simulations an average energy of 30 eV was used, which is in the upper range of what was found here.

The results which have been presented in this chapter, should be regarded as preliminary results. Further tests, with a magnetic field available, must be conducted in order to determine the accuracy of the proposed calibration system. Time did not allow for such tests to be carried out within the scope of this thesis. Some valuable information was however obtained from the results, and this will be discussed in the next chapter.

# Chapter 5

## Discussion

Previous measurements done with the IPM have shown that the performance decreases after long term use, caused by the ageing of the MCPs [1, 2]. The goal of this thesis has been to design a calibration system to measure this effect, and thereby be able to compensate for it. The aim of the calibration system is to be able to produce an image from the IPM, where the gain is homogenous within an error of less than 1%. In this chapter the results of the simulations and experiments, and the possibility of reaching this goal, will be discussed.

To be able to calibrate the MCP, a homogenous and controllable electron current must be used as reference signal. In this thesis, two fundamentally different electron sources have been considered. The first source to be considered, was a headed wire grid. As shown in the simulations, the emitted electron current from such a grid is far from homogenous over an area as large as the MCP. As the goal is to make a homogenous distribution at the MCP, the electric and magnetic field must be adjusted so that the electrons spread out as much as possible during their drift through the volume of the MCP. In this way, the resulting distribution at the MCP will become more homogenous.

If an EGP is used as the electron source for calibration, the initial electron distribution is assumed to already be homogenous. In contrary to the case of the wire grid as electron emitter, the objective of the applied electric and magnetic field is now to preserve this homogenous electron distribution during its drift to the MCP.

A third alternative, would be to implement a small, but movable electron source in the IPM. A calibration of the system could then be done by moving this device around. Constructing such a system has however not been considered in this thesis, as building a device that can be accurately moved around, and fitted within the vacuum tank, without affecting the electric field or vacuum pressure, would be very difficult.

Before the work on this thesis begun, some initial experiments had been done with a heated wire as electron source. Using a heated wire grid as the electron source for the initial experiments is a natural first choice, because of its simplicity.

A heated wire grid would be relatively cheap and easy to implement, however the initial experiments showed that the resulting homogeneity of the electron current at the MCP was too poor. This was confirmed by the simulations presented in this thesis, and the demand for a more sophisticated electron emitting device emerged.

To the authors knowledge, the only company producing such a device is Burle, Inc. [4] The Electrongen<sup>TM</sup> EGP produced by Burle, Inc. is characterised as a cold ionisation source, offering a parallel electron current over an area large enough to cover the entire imaged area of the IPM. The emission uniformity is specified to be better than 10% and stable over time [18]. However, an EGP of the required size is a rather costly (\$2-4000) and very fragile device. A custom made ceramic frame and specially trained personnel is needed to mount it. Nevertheless, if the EGP meets the promised specifications, it will provide value for money with its reliability and homogenous electron current.

It is however doubtful that it will allow an absolute calibration of the gain in the system within the accuracy which was aimed for, an error of 1%, as the homogeneity of the emission is specified to be only within 10%. However, if the emission of the EGP remains constant over time, a higher degree of accuracy could probably be achieved by comparing measurements, and thereby obtaining a relative calibration.

To evaluate how the electron distribution from the wires and EGP would change, by the drift through the IPM, the electric field of the IPM and the drift path of the electrons, subject to various conditions, were examined. With the simulations, some values for the resulting homogeneity of the electron distribution at the MCP were also given.

As mentioned above, the way the electrons are manipulated by the drift is fundamentally different depending on the electron source. For the case of the electrons emitted from the heated wire grid, where the aim is to spread out the distribution, two approaches can be made when selecting the magnetic field. The first approach would be to tune the magnetic field so that the electrons complete exactly one half revolution during their drift through the chamber, and thereby get spread out as much as possible. The second approach would be to apply no magnetic field at all, and thereby not constraining the movement of the electron with the magnetic field at all. The simulations indicate that the second case, applying no magnetic field at all, gives the best spread in the electron distribution. However, the spread is still poor, and at low fields the edge effects are significant. Increasing the field reduces the edge effects, but constrains the electrons so that the final distribution at the MCP is very non-homogenous. In all the simulated cases, the results for the wire grid were considered too poor to be useful for calibration purposes.

Considering the EGP as electron emitter, there are also two different approaches to preserve the electron distribution by the use of a magnetic field. The first technique which could be used, is to adjust the magnetic field so that

---

the electrons perform exactly one complete revolution during their drift to the MCP, and thereby preserve their initial position in the  $xz$ -plane. As shown in the theory chapter, the magnetic field required for the electrons to complete exactly one revolution (or an integer number), is dependent upon the initial energy of the electrons. A spread in the initial energy of the emitted electrons will therefore affect the final electron distribution at the MCP. The other scheme, which could be used to preserve the electron distribution from the EGP, is to apply a strong magnetic field. As showed in the theory chapter, the maximum possible offset an electron can get, is inversely proportional to the magnitude of the applied magnetic field. The simulations indicate that this technique will give the best results, and that a magnetic field of 1000 Gauss would be sufficient to constrain the electrons. However, applying an even stronger field would only improve the results further. Indeed, this is the technique which is already in use to constrain the movement of the electrons during beam profile measurements. A magnetic field of 2000 Gauss is used, produced by an electromagnet installed around the IPM in the SPS tunnel.

As a measure for how much the electrons will spread at different magnetic field strengths, the cyclotron radius can be used. The cyclotron radius as a function of the applied magnetic field, together with the values for the electron offset obtained from the Garfield simulations, are shown in Fig. 5.1. The theoretical values are computed analytically based on the assumptions presented in earlier chapters.

Applying a magnetic field of 1000 Gauss, will result in an average offset of less than  $20 \mu\text{m}$ , which is far less then the imaging systems resolution of  $104$  by  $156 \mu\text{m}$ . Applying such a strong field may however result in detectable shadow effects from the cathode wires, while a lower field, allowing more electron offset, might smear out this effect. However, by applying a weaker magnetic field, edge effects caused by inhomogeneity in the electric field become more evident. The exact value of the optimal magnetic field strength should therefore be determined experimentally, however applying a magnetic field of 1000 Gauss or more is expected to give satisfactory results. For simplicity, it is suggested that the magnetic field in calibration mode is chosen to be 2000 Gauss, as this value is used during beam measurements.

At magnetic fields below 10 Gauss, the graph shows that it is no longer the magnetic field which is the limiting factor for the spread of the electrons. It is rather the applied electrical field, or more precisely the ratio between the initial transversal electron energy and the electric field, which cause the electrons to reach the MCP before the offset in the image plane becomes too large, see Section 2.2.1.

As few details about the emission spectra for EGPs are published, several assumptions had to be made in order to complete the simulations of the IPM with the EGP as calibration source. Even though the exact initial energy distribution of the emitted electrons still is unknown, it seems safe to assume that the spread in

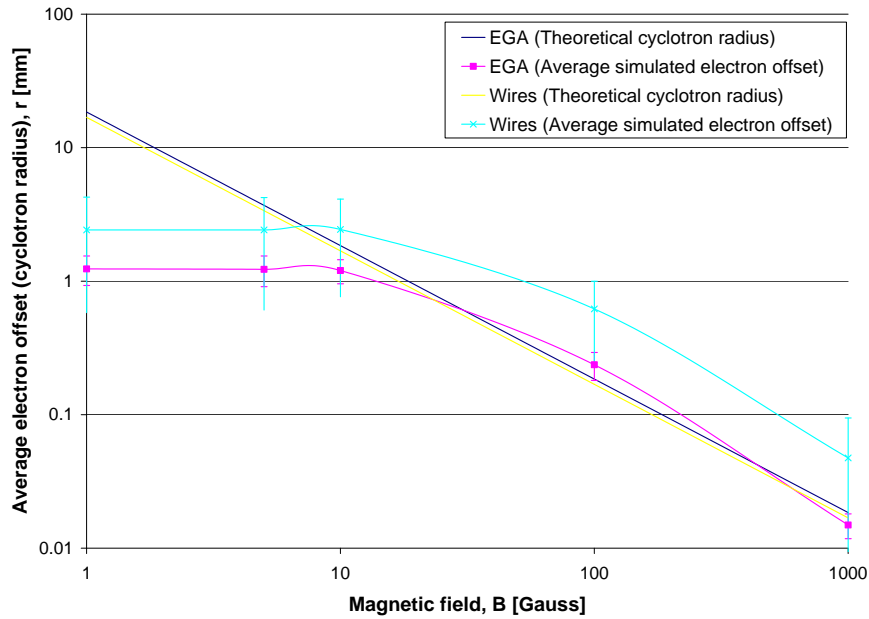


Figure 5.1: *The cyclotron radius obtained from analytical estimates, and the average offset of the electrons in the image plane obtain by drift simulations in Garfield, both plotted as a function of the applied magnetic field.*

energy will be considerable. This supports the idea of choosing a strong magnetic field to constrain the maximum movement of the electrons, rather than trying to match the magnetic field to the energy of the electrons to make them complete exactly one revolution. If a strong magnetic field is used the exact values, or distribution of the initial electron energy, is not important.

For the applied electrical field, there is less freedom in the choice of settings. Because the detection efficiency of the MCP varies with the incoming electron energy, it is important that the energy of the electrons reaching the MCP during calibration, is as close as possible to those detected during beam profile measurements. During normal operation of the IPM, a potential difference of 4000 V is applied between the cathode and anode. The beam passes through the center of the IPM, so the potential difference between the position where the electrons are generated and the MCP will be half of this value, 2000 V. Assuming that the electrons have small energy when they are created, their energy will be 2000 eV when they reach the MCP.

Consequently, the potential difference between the electron emitter and MCP should also be chosen so that the calibration electrons acquire the same amount of energy. This can be obtained by choosing a potential difference of about

---

2000 V between the electron source and the MCP during calibration mode. The potential setting for the emitting face of the EGP ( $E_o$ ), should be chosen so that the electric field becomes as homogenous as possible during calibration mode. The calculations done for the simulations, suggest a value for  $E_o$  of -1143 V, when  $C_{age} = -1000$  V and  $M_i = 1000$  V. In the experimental setup the potentials for  $C_{age}$  and  $M_i$  were kept at the suggested values. A value for  $E_o$  of  $-1163 \pm 1$  V was found to give the best result, a value less than 2% from the predicted value. At this value the pattern from the wires disappeared completely. However, the pattern reappeared, if any of the potentials were changed only by a few volts. The wire pattern is clearly visible at low magnetic fields in the simulations. This is probably because  $E_o$  is not chosen to the optimal value. The optimal value for the simulations will differ slightly compared to the one for the experiments, as the field configurations are not exactly equal and this value is very sensitive to the field configuration.

It should be noted that the high voltage supplies used in the test setup were rather old, and may not have been very accurate, so that there is some uncertainty related to the absolute values of these numbers. It may also be difficult to provide high voltage within an accuracy of  $\pm 1$  V from the power supplies used in the tunnel. If however a magnetic field is added, which is available in the tunnel installation, the effect of perturbations to the electric field will be less. The reason for this is, as mentioned above, that the magnetic field will constrain the movement of the electrons.

In the models used to simulate the electric fields, the geometry was somewhat simplified. This was done to make the field calculations easier, as many small details would have required a lot more computing power. The most important simplifications done, were that few rounded edges of the parts were included. In the IPM, all the electrodes and the frame of the EGP have rounded edges, to produce a smoother field. If this had been taken into account in the simulations, the electric field in areas close to the electrodes and frames, is expected to have been smoother. A result of this can be seen when comparing the simulated results with the experimental data, the edge effects appear noticeably smaller in the experimental data.

In the experimental setup, the resulting intensity on the MCP was found to increase towards one corner. This effect had not been predicted by the simulations, and it took quite some time to understand what was causing it. The effect is suggested to be caused by the channels of the EGP being biased at an angle of  $8^\circ \pm 1^\circ$  from the normal of the EGP [11], in the direction towards the brighter corner. This changes the energy of the electrons in the transverse direction (xz-direction), compared to the electrons being emitted normal to the EGP. The effect is most significant at low magnetic fields, where the initial transversal electron energy strongly affects the resulting electron distribution at the MCP.

A simulation was done, assuming that the electrons were emitted at an angle

of  $8^\circ \pm 1^\circ$  from the normal of the EGP, instead of  $-5^\circ$  to  $+5^\circ$  as previously assumed. The results of the simulation fit qualitatively with the experimental data, as the electron distribution was found to be shifted towards one corner. In the experimental data, the projection of the intensity onto either axis is seen to steadily increase. The same trend can be seen in the simulated data, but the result is not quite as pronounced. A reason for this is that the distortion from the wires and edges are much more evident in the simulated data.

In the same way as the emission angle of the electrons is important at low magnetic field, the average initial electron energy and distribution is important. The average initial energy of the electrons was found to vary linearly with the gain of the EGP, and the estimate used in the simulations was in the upper range of what was found in the experiments. This should, however, be of less importance if a magnetic field is applied.

To check how homogenous the final electron distribution at the MCP actually is, and if it is good enough to be used for calibration purposes, further test must be conducted. The test should be done in a setup where the magnetic field can be controlled.

If perturbations to the resulting intensity distribution still are found, it might be difficult to tell if they originate from the EGP or the MCP, without any other electron source in the system. To investigate this matter a possible procedure would be to dismantle the IPM, turn one of the plates by 90 or 180 degrees, and then reassemble the system. If the intensity pattern were to change as a result of this intervention, the source of error should be expected to be the plate which was turned. If no change in the pattern is found, the source of error must be the other plate, or somewhere else in the setup. This procedure should be repeated until the source of error is found, or until it can be ruled out that the EGP or MCP is the source of error. Dismantling and reassembling the IPM is however a quite comprehensive task, which requires qualified personnel. Restoring the vacuum in the tank may also take some time.

Another possible source of error for the read out system, could be the phosphor layer where the electrical signal is transformed to photons visible to the camera. Uneven deposition of the phosphor on the prism, could cause the electron-photon conversion to be lower at certain areas. Another remote possibility is that there is a problem with the prism itself, i.e. that it does not act as a perfect mirror. Both these effects are regarded as unlikely to cause any distortion.

During operation, the intensity of electrons will vary considerably across the area of the MCP. Consequently, it is difficult to give an estimate of the optimal electron current, using values only from beam profile measurements. Rather, the properties of the MCP and EGP must be considered. As an upper limit for the electron current, the worst case estimate for the onset of saturation in the MCP is chosen, that is  $10^{-7}$  A/cm<sup>2</sup> when operating with a bias voltage of 1000 V. The lower limit is determined by the properties of the EGP, as the emission current of the EGPs cannot be assumed to keep its homogeneity below

---

$10^{-12}$  A/cm<sup>2</sup> [19]. The EGP used in this setup, is specified to produce an electron current of  $10^{-9}$  A/cm<sup>2</sup> at a bias voltage of 1000 V [11].

The experiments showed that a gain of 1000 V, for both the EGP and MCP, is too high. The gain should not be higher than necessary, as the lifetime of the plates is shorter when operating at high gain. However, the gain should not be too low either, as this may result in a less homogenous electron emission [19]. Gain values of around 600 V were found to be suitable for both plates, and resulted in an easily detectable signal, with intensity well below any visible saturation effects. For a gain of 600 V, a saturation limit of  $1.8 \times 10^{-7}$  A/cm<sup>2</sup> was calculated for the MCP used in the setup. This is slightly above the predicted worst-case estimate for an MCP operating at 1000 V.

The vacuum pressure of only about  $6 \times 10^{-6}$  mbar used in the experimental setup, could also cause trouble if the MCP was operated at full gain. A pressure above  $10^{-6}$  mbar is not recommended for operating the MCP, and could cause damaging ion feedback or electrical breakdown [38]. For the gain values used in this experiment however, no effects of poor vacuum were seen.

It is vital that the implementation of the EGP, as an electron source for calibration of the IPM, does not decrease the IPMs performance during normal operation. The changes made to the IPM should not decrease the homogeneity of the electric field, and it must be certain that no electrons are emitted into the drift volume during beam profile measurements. The experiments indicate that in operation mode, a potential difference of about 200 V between E<sub>o</sub> and Cage is all that is required to stop electrons emitted from the EGP. As secondary electrons are assumed to have lower energy than the electrons emitted from the EGP, this enables the EGP to be kept at a potential of only 2-300 V lower than Cage during operation. In this way, the electric field in the IPM during operation mode is in fact improved, compared to the original design.

To prevent the EGP from emitting any electrons, it should be sufficient to make sure no potential difference is applied to it, even when operating in an environment of heavy ion bombardment [19]. Should it however turn out to be a problem that the EGP emits electrons during beam profile measurements, a reversed bias voltage could be applied. This would cause any generated electrons to be emitted up from the EGP, instead of down into the chamber. Furthermore, coating the EGP to reduce secondary emission as were done with the MCPs and other interior of the IPM, should be considered.

Based on the results presented in this thesis, a summary of recommended potential settings for the calibration and operation mode of the IPM are given in Fig. 5.2.

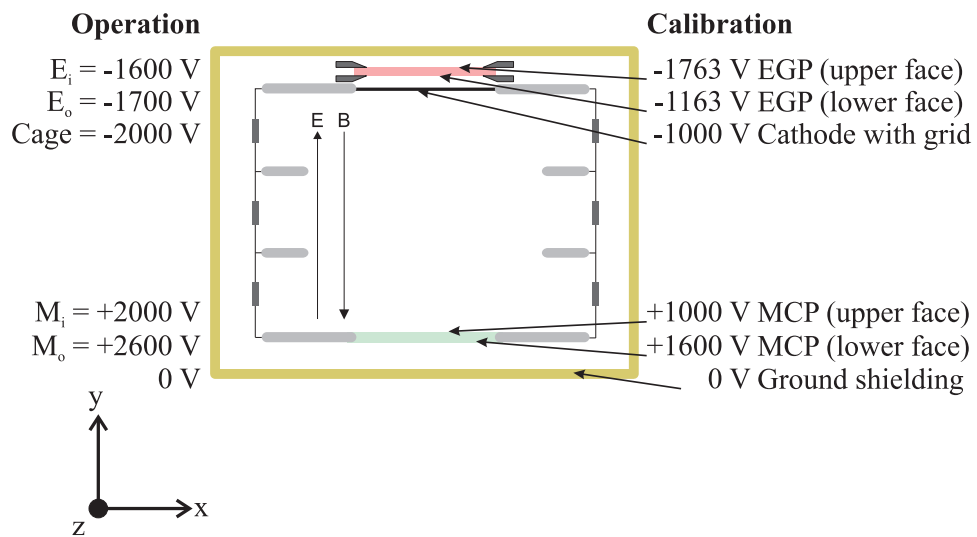


Figure 5.2: A summary of the recommended potential settings for use during calibration and operation mode of the IPM.

# Chapter 6

## Conclusion

The goal of this thesis has been to design a calibration system that measures the gain of the imaging system in the IPM. Two different sources have been considered as electron emitters, a heated wire grid and an EGP. The simulations presented in this thesis, showed that the wire grid would not produce a distribution of electrons that is sufficiently homogenous to be used for calibration purposes.

The EGP shows promising results, however, no final conclusion about the accuracy of a calibration system based on this device could be made with the experimental setup available. When the bias angle of the EGP was taken into account, the simulations were in agreement with the experimental data. The edge effects and effect of the cathode wires on the resulting electron distribution, were more evident in the simulations than in the experimental data. This is expected to be caused by inaccuracy in the simulated model, in particular the edges of the objects, and the potential settings. As no magnetic field was available, an electron distribution that was shifted, and increased in intensity in the direction of the channels of the EGP, was found. Simulations indicated that this effect is expected to be suppressed, if a magnetic field was applied.

The detection efficiency of the MCP is dependent upon the energy of the incoming electrons. In order to make the calibration system as accurate as possible, the electrons arriving at the MCP during calibration should have the same energy as the electrons arriving during beam profile measurements. As the beam passes through the center of the IPM, while the calibration electrons are emitted near the cathode, this can be obtained by using half the value of the potential difference between the anode and cathode during calibration, compared to what is used during beam profile measurements. The potential of the EGP must also be carefully adjusted, in order to avoid distortion to the electron distribution caused by the wires of the cathode grid.

Gain values of about 600 V for both the MCP and EGP were found to give sufficient intensity of the signal. Operating the plates at this value, well below the maximum specified gain values, will prolong their lifetime.

The values for the impedance of the resistors connected between the lateral

electrodes, were found to differ noticeably. However, simulations indicate that the effect this may have on the resulting electron distribution, is small.

Further test should be performed, applying a magnetic field of at least 1000 Gauss. 2000 Gauss is used during beam profile measurements, and it is recommended that this value also should be used for calibration purposes. Experiments carried out under these conditions, will reveal what accuracy can be obtained using the calibration system. At a magnetic field of 1000 Gauss or more, the resolution is limited only by the camera used to acquire the images.

The goal for the calibration system, is to be able to measure the gain of the imaging system within 1%. It is doubtful that an absolute calibration can be achieved to this accuracy, as the EGP is specified to emit a homogenous field of electron only within 10%. Depending on how the EGPs emission change over time, it is possible that higher accuracy may be achieved for relative calibrations, by comparing images.

Both simulations and experiments indicate that the proposed calibration system, should not deteriorate the performance of the IPM during beam profile measurements. The experiments showed that a potential difference of a little more than 200 V between the EGP and the cathode, was sufficient to prevent any electrons, originating from the EGP, from reaching the MCP, when the cathode and MCP were at  $\pm 2000$  V. Simulation show that the homogeneity of the electric field in operation mode in fact will improve with the calibration system implemented, when a potential difference of 300 V between the EGP and cathode is applied. 300 V is probably more than necessary, but these values should eventually be verified during actual beam profile measurements.

# Bibliography

- [1] J. Koopman, “IPMV51734, problems and cures.” Presentation 14.01.2004 at BDI day, CERN, January 2004.
- [2] G. Ferioli, C. Fischer, J. Koopman, and M. Sillanoli, “Sensitivity studies with the SPS rest gas profile monitor.” CERN SL-2001-026 BI, May 2001. CERN Technical Note. Presented at DIPAC 2001, Grenoble, France.
- [3] J. L. Wiza, “Microchannel plate detectors,” *Nucl. Instr. and Methods* **162**, pp. 587–601, 1979.
- [4] Burle, Inc., “Burle, Inc. Homepage.” Web page: <http://www.burle.com>. Visited May 5, 2004.
- [5] CERN, “CERN Homepage.” Web page: <http://cern.ch>, April 2003. Visited May 4, 2004.
- [6] F. Hornstra, “Residual gas ionization profile monitors for the HERA proton machines.” DESY HERA 87-25, October 1987. DESY Technical Note.
- [7] R. Connolly, P. Cameron, W. Ryan, T. J. Shea, R. Sikora, and N. Tsoupas, “A prototype ionization profile monitor for RHIC.” PAC 1997 Conference Papers, Vancouver, May 1997. pp. 2152-2154.
- [8] J. Amundson, J. Lackey, P. Spentzouris, G. Jungman, and L. Spentzouris, “Calibration of the fermilab booster ionization profile monitor,” *Phys. Rev. ST Accel. Beams* **6**(102801), pp. 1–8, 2003.
- [9] C. Fischer and J. Koopman, “Ionisation profile monitor tests in the SPS.” CERN SL-99-046 BI, August 1999. CERN Technical Note.
- [10] Burle, Inc., “Electrogen<sup>TM</sup> electron generator arrays.” Web page: <http://www.burle.com>, February 2002. Burle Technical Note TP220.
- [11] Burle, Inc., “Procedures and specifications for MCPs and EGAs.” Data sheets, 2004.

## BIBLIOGRAPHY

---

- [12] R. Connolly, "SNS IPM Status." Presentation given at the SNS Beam Diagnostics Review Meeting, Brookhaven National Laboratory, Web page: <http://www.sns.gov/diagnostics/diaghme.html>, February 2004. Visited June 3, 2004.
- [13] R. Connolly. Private communication, 2004.
- [14] S. Pordes. Private communication, 2004.
- [15] D. J. Griffiths, *Introduction to Electrodynamics*, Prentice-Hall, Inc., 3rd ed., 1999.
- [16] F. Hornstra, "Conversion of the HERA residual gas ionization profile monitors into spectrometers (to measure energies of electrons and ions liberated by high energy protons.)" DESY HERA 89-03, January 1989. DESY Technical Note.
- [17] Burle, Inc., "Burle Long-Life<sup>TM</sup> MCP Selection Guide." Web page: <http://www.burle.com>, February 2003. Burle Technical Note EP107.
- [18] B. N. Laprade, F. E. Langevin, and R. Starcher, "The development of a novel, cold electron source." Paper 328, Presented at The ASMS Conference, Orlando, Florida, June 2002.
- [19] Burle, Inc. Private communication with R. Cochran., 2004.
- [20] Hamamatsu Photonics K.K., "MCP assembly - technical information." Technical note, May 1994. Cat. No. TPMH1094E01.
- [21] M. J. Fransen, *Towards High-brightness, Monochromatic Electron Sources*, Delft University of Technology, 1999. Ph.D Thesis.
- [22] V. K. Rohatgi and A. K. M. E. SALEH, *An Introduction to Probability and Statistics*, John Wiley & sons, Inc., 2nd ed., 2001.
- [23] F. Rosebury, *Handbook of electron tube and vacuum techniques*, Addison-Wesley Publishing Company, Inc., 1965.
- [24] S. M. Sze, *Physics of semiconductor devices*, John Wiley & sons, Inc., 2nd ed., 1981.
- [25] J. Koopman. Private communication, 2004.
- [26] Ansoft Corporation, "Ansoft Corporation Homepage." Web page: <http://www.ansoft.com>. Visited March 30, 2004.
- [27] R. Veenhof, "Garfield homepage." Web page: <http://cern.ch/garfield>, 2001. Visited March 30, 2004.

- [28] Ansoft Corporation, “Maxwell manual.” Web page:  
<http://wwwce.web.cern.ch/wwwce/ae/Maxwell/documentation.html>,  
2002. Visited March 30, 2004.
- [29] R. Veenhof, “Garfield technical notes.” Web page:  
<http://rjd.home.cern.ch/rjd/garfield/notes.html>, 2004. Visited  
April 14, 2004.
- [30] N. Ida and J. P. A. Bastos, *Electromagnetics and calculation of fields*,  
Springer-Verlag New York, Inc., 2nd ed., 1997.
- [31] J. Jin, *The Finite Element Method in Electromagnetics*, John Wiley & sons,  
Inc., 2nd ed., 2002.
- [32] R. Chritin, “Mesures de l’aimant dipôle radial RFM-Hn avec culasse  
modifiée.” SL-Note-2001-050 MS, Décembre 2001. CERN Technical Note.
- [33] e2v technologies, inc, “L3C65 series low light CCD camera.” Data sheet,  
September 2003.
- [34] P. Varga and H. Winter, *Particle Induced Electron Emission II*, vol. 123  
of *Springer Tracts in Modern Physics*, ch. Slow Particle-Induced Electron  
Emission from Solid Surfaces, pp. 149–213. Springer-Verlag, 1992.
- [35] A. Rossi, “SPS electron cloud measurements with TiZrV NEG coating.”  
Presentation at CERN: SPS Scrubbing Run Results and Implications for  
the LHC, June 2002.
- [36] W. Vollenberg, “NEG coating on MCP.” CERN Internal work report,  
February 2004.
- [37] B. Dehning. Private communication, 2004.
- [38] Burle, Inc., “Storage, Handling, and Operation of Microchannel Plates.”  
Web page:  
<http://www.burle.com>, August 2003. Burle Technical Note.

## BIBLIOGRAPHY

---

# Appendix A

## Garfield source code

The source code used for the simulations are given in the following sections. For the case of electrons emitted from the EGP, the complete source code is included. For the simulations of electrons emitted from wires, and the simulation where the bias angle of the channels of the EGP is taken into account, only the part describing the electron emission is included. The rest of the source code is identical, or very similar, to the one used for electron emission from the EGP.

The complete source code for all cases can be downloaded from <http://www.fysmat.ntnu.no/~refsum/diplom/>.

### A.1 Electron drift from EGP

```
1 *****
2 * Simulation of electron drift in vacuum chamber *
3 * Helge H. Refsum, AB/BDI/BL, CERN *
4 * 2004 *
5 *****
6
7 * GLOBAL PARAMETERS
8
9 Global nrndm = 100000 // Number of drift lines
10 Global field = false // Do you want to plot the field area?
11 Global plot = false // Do you want to plot the drift area?
12 Global file = true // Write plot output to file?
13 Global read = false // Read Maxwell files?
14
15 * Path to Maxwell files
16 Global MaxPath = '~/Maxwell/project_dirs/default/IPM_EGA_Burle.pjt/'
17
18 * Output format for plot files
19 *Global ini_file = '~/garfinit_color'
20 Global filepre = 'ega'
21 Global filepost = '.eps'
22 Global filetype = 'EPS'
23 *Global filepost = '.tex'
24 *Global filetype = 'LaTeX'
25
26 Global ega = 9.0 // y-position of ega [cm]
27 *Global wire = 8.4 // y-position of wires (height of chamber) [cm]
28
```

## APPENDIX A. GARFIELD SOURCE CODE

---

```
29 global E_ave = 30          // Average electron energy [eV]
30 global gamma = E_ave      // Gamma parameter i exp-dist
31 *global V_EGA = 500       // EGA operating voltage - Check value!
32
33 *Magnetic field strength
34 global magnetic = 60      // Rest field approx 6 Gauss, max field 2000 Gauss
35 *Parse Arg magnetic
36 *Say "Magnetic field = {magnetic} Gauss"
37 global V_Bias = 1000     // Bias voltage
38
39 * Define area spanned by Electron Generator Array (EGA)
40 global ega_x=5.08
41 global ega_z=5.08
42 global ega_y=0.102
43
44
45 If batch Then
46     !deact metafile
47     !close metafile
48     !del metafile
49 Endif
50
51 * Read field-map from Maxwell
52 &CELL
53 cell-id "IPM with EGA"
54
55 if read then
56     If file then
57         !add meta type "{filetype}" ...
58             file-name "{filepre}_Mesh_histogram{filepost}"
59         !open meta
60         !act meta
61     Endif
62
63     * Read field-map from Maxwell files
64     field-map ...
65         files "{MaxPath}V.reg" "{MaxPath}E.reg" "{MaxPath}D.reg" ...
66         field-simulator-3d ...
67         drift-medium 1.0 ...
68         x-mirror-periodic ...
69         z-mirror-periodic ...
70         not-y-periodic ...
71         plot-map ...
72         histogram-map
73
74     If file then
75         !deact meta
76         !close meta
77         !del meta
78     Endif
79
80     save-field-map "{MaxPath}ipm.map"
81 else
82     * Read saved Garfield files
83     read-field-map "{MaxPath}ipm.map"
84 endif
85
86
87 * Show field
88 &FIELD
89 If field then
90
91 If file then
92     !add meta type "{filetype}" file-name "{filepre}_field_z0{filepost}"
93     !open meta
```

## A.1. ELECTRON DRIFT FROM EGP

---

```
94         !act meta
95 Endif
96
97 area {-12.5, 0, -17.5, +12.5, +10, +17.5} view z=0.01 // Select plot area
98 plot-field contour // make the plot
99
100 If file then
101     !deact meta
102     !close meta
103     !del meta
104 Endif
105
106
107 If file then
108     !add meta type "{filetype}" file-name "{filepre}_field_x0{filepost}"
109     !open meta
110     !act meta
111 Endif
112
113 area {-12.5, 0, -17.5, +12.5, +10, +17.5} view x=0.01 // Select plot area
114 plot-field contour // make the plot
115
116 If file then
117     !deact meta
118     !close meta
119     !del meta
120 Endif
121
122 !contour-parameters ...
123     epsilon-gradient 1e-4 ...
124     epsilon-tracing 1e-4 ...
125     grid-tolerance 0.5
126 grid 20
127
128 If file then
129     !add meta type "{filetype}" ...
130         file-name "{filepre}_field_z0_zoom{filepost}"
131     !open meta
132     !act meta
133 Endif
134
135 area {-5, 7.5, -5, +5, +9.2, +5} view z=0.01 // Select plot area
136 plot-field contour N 100 // make the plot
137
138 If file then
139     !deact meta
140     !close meta
141     !del meta
142 Endif
143
144
145 If file then
146     !add meta type "{filetype}" ...
147         file-name "{filepre}_field_x0_zoom{filepost}"
148     !open meta
149     !act meta
150 Endif
151
152 area {-5, 7.5, -5, +5, +9.2, +5} view x=0.01 // Select plot area
153 plot-field contour N 100 // make the plot
154
155
156 If file then
157     !deact meta
158     !close meta
```

## APPENDIX A. GARFIELD SOURCE CODE

---

```
159         !del meta
160     Endif
161
162 Endif
163
164
165 * Define magnetic field (x,y,z)
166 &MAGNETIC
167 components 0 -{magnetic} 0 G // Rest field approx 6 Gauss, max field 2000 Gauss
168
169 * Input gas data // Will not be used yet, simulating electron drift in vacuum
170 &GAS
171 temperature 300 K
172 pressure 1e-8 torr // Near vacuum
173 CO2 // Check gas data!
174
175
176 &DRIFT // Simulate electron drift
177
178 If file*plot then
179     !add meta type "{filetype}" file-name "{filepre}_drift{filepost}"
180     !open meta
181     !act meta
182 Endif
183
184 * Simulate drift in vacuum:
185 integration-parameters ...
186     integration-accuracy 1e-4 ...
187     nomaximum-step-length ...
188     mc-dist-int 0.001 ...
189     trap-radius 1
190 * Declare variables
191 global time // Drifttime
192 global status // Status at end-of-drift calculation
193
194 * Open a plot frame
195 area {-3, 0, -3, +3, +9.5, +3} view x=0 cut // Select plot area
196 *area {-12.5, 0, -17.5, +12.5, +10, +17.5} view x=0 cut // Select plot area
197 *area {-4, -1, +4, +11} cut // Select plot area
198 *area {-12, -1, +12, +11} cut // Select plot area
199 *area {-1, 8, 1, 9} cut // Select plot area
200 *area {-1, 0, 1, 9} cut // Select plot area
201
202 If plot Then Call plot_drift_area
203
204 * Histograms to check the homogeneity
205 Call book_histogram(hx_start, 100, -ega_x/2, ega_x/2)
206 Call book_histogram(hx_end, 100, -ega_x/2, ega_x/2)
207 Call book_histogram(hz_start, 100, -ega_z/2, ega_z/2)
208 Call book_histogram(hz_end, 100, -ega_z/2, ega_z/2)
209 Call book_histogram(hz_start_2, 100, 0.200, 0.250)
210 Call book_histogram(hz_end_2, 100, 0.200, 0.250)
211 Call book_histogram(velocity, 100, 0, 1000*1e4)
212 Call book_histogram(energy, 100, 0, 200)
213 Call book_histogram(offset, 100, 0, 50/magnetic)
214 Call book_histogram(drift, 100, 0, 10)
215
216 * Matrix for 3D plot
217 Call book_matrix(start, 100, 100)
218 Call book_matrix(MCP, 100, 100)
219 global start[;] = 0
220 global MCP[;] = 0
221 global range row(100)
222
223 For irndm From 1 To nrndm Do
```

## A.1. ELECTRON DRIFT FROM EGP

```

224 *Startpoint of electron [cm] At Electron generator array
225 * global x = -1 + 2*(irndm-1)/(nrndm-1)
226 * global x = -ega_x/2 + ega_x*(irndm-1)/(nrndm-1)
227 global x = -ega_x/2 + ega_x*rnd_uniform
228 global y = ega
229 global z = -ega_z/2 + ega_z*rnd_uniform
230
231 *Initial velocity of electron [cm/microsec]
232 global E = rnd_exponential(gamma) // [eV]
233 global v = 59.3*sqrt(E) // [cm/us]
234 global theta = 0.1*(2*rnd_uniform-1)
235 global phi = 6.28*rnd_uniform
236 global vy = -v*cos(theta)
237 global vx = v*sin(theta)*cos(phi)
238 global vz = v*sin(theta)*sin(phi)
239
240 If entier(irndm/100)*100=irndm Then
241     Say "i = {irndm}/{nrndm}"
242     *say "E = {E} [eV]"
243     *say "v = {v} [cm/microsec]"
244     *Say "vx, vy, vz = {vx, vy, vz} [cm/microsec]"
245 endif
246
247 * Simulate electron drift in vacuum
248 call drift_vacuum_electron(x,y,z, vx,vy,vz, status, time)
249 Call drift_information( ...
250     'steps',nstep,'x_end',x_end,'y_end',y_end,'z_end',z_end)
251 * Say "Drift line ended with status {status}, t={time}, {nstep} steps"
252 * Say "x,y,z = {x,y,z}"
253 * Say "x_end, y_end, z_end = {x_end, y_end, z_end}"
254
255 * Enter data in the histograms and matrix
256 Call fill_histogram(velocity, v*1e4)
257 Call fill_histogram(energy, E)
258 Call fill_histogram(hx_start, x)
259 Call fill_histogram(hz_start, z)
260 Call fill_histogram(hz_start_2, z)
261 global matx = ( ( x + ega_x/2 ) * 100 / ega_x ) + 1
262 global matz = ( ( z + ega_z/2 ) * 100 / ega_z ) + 1
263 *say "matx, matz = {matx},{matz}"
264 if (1 =< matx) & (1 =< matz) & ...
265     (matx =< 100) & (matz =< 100) then ...
266     global start[matx;matz] = start[matx;matz] + 1
267
268 if (y_end < 0.1) then
269     global r = sqrt( (x-x_end)^2 + (z-z_end)^2 )
270     *Say "Electron offset r = {r}"
271     *Say "Drift time = {time}"
272     Call fill_histogram(drift, time*1000)
273     Call fill_histogram(offset, r)
274     Call fill_histogram(hx_end, x_end)
275     Call fill_histogram(hz_end, z_end)
276     Call fill_histogram(hz_end_2, z_end)
277     global matxend = ( ( x_end + ega_x/2 ) * 100 / ega_x ) + 1
278     global matzend = ( ( z_end + ega_z/2 ) * 100 / ega_z ) + 1
279     *say "matxend, matzend = {matxend},{matzend}"
280     if (1 =< matxend) & (1 =< matzend) & ...
281         (matxend =< 100) & (matzend =< 100) then ...
282         global MCP[matxend;matzend] = MCP[matxend;matzend] + 1
283 endif
284
285
286 * Plot the electron
287 If plot Then Call plot_drift_line
288 Enddo

```

## APPENDIX A. GARFIELD SOURCE CODE

---

```
289 If plot Then
290     Call plot_comment('UP-RIGHT',"Magnetic field: {magnetic} Gauss")
291     Call plot_comment('DOWN-RIGHT',"Bias voltage: {V_Bias} Volts")
292     Call plot_end
293 endif
294 If file*plot then
295     !deact meta
296     !close meta
297     !del meta
298 Endif
299
300
301 * Make 3D plots
302 If file then
303     !add meta type "{filetype}" ...
304     file-name "{filepre}_3d_start{filepost}"
305     !open meta
306     !act meta
307 Endif
308 call plot_surface(start, 90, 0, range, range, 'x', 'z', ...
309     'Distribution of emitted electrons')
310 Call plot_comment('UP-LEFT',"Magnetic field: {magnetic} Gauss")
311 Call plot_comment('DOWN-LEFT',"Bias voltage: {V_Bias} Volts")
312 Call plot_comment('UP-RIGHT',"Average electron energy: {E_ave} eV")
313 Call plot_comment('DOWN-RIGHT',"Totalt number of electrons: {nrndm}")
314 Call plot_end
315 If file then
316     !deact meta
317     !close meta
318     !del meta
319 Endif
320
321 If file then
322     !add meta type "{filetype}" ...
323     file-name "{filepre}_3d_end{filepost}"
324     !open meta
325     !act meta
326 Endif
327 call plot_surface(MCP, 90, 0, range, range, 'x', 'z', ...
328     'Distribution of electrons on MCP')
329 Call plot_comment('UP-LEFT',"Magnetic field: {magnetic} Gauss")
330 Call plot_comment('DOWN-LEFT',"Bias voltage: {V_Bias} Volts")
331 Call plot_comment('UP-RIGHT',"Average electron energy: {E_ave} eV")
332 Call plot_comment('DOWN-RIGHT',"Totalt number of electrons: {nrndm}")
333 Call plot_end
334 If file then
335     !deact meta
336     !close meta
337     !del meta
338 Endif
339
340 If file then
341     !add meta type "{filetype}" ...
342     file-name "{filepre}_3d_diff{filepost}"
343     !open meta
344     !act meta
345 Endif
346 global change = MCP - start
347 call plot_surface(change, 90, 0, range, range, 'x', 'z', ...
348     'Change in electron distribution')
349 Call plot_comment('UP-LEFT',"Magnetic field: {magnetic} Gauss")
350 Call plot_comment('DOWN-LEFT',"Bias voltage: {V_Bias} Volts")
351 Call plot_comment('UP-RIGHT',"Average electron energy: {E_ave} eV")
352 Call plot_comment('DOWN-RIGHT',"Totalt number of electrons: {nrndm}")
353 Call plot_end
```

## A.1. ELECTRON DRIFT FROM EGP

---

```
354 If file then
355     !deact meta
356     !close meta
357     !del meta
358 Endif
359
360
361
362
363 * Make histograms
364 If file then
365     !add meta type "{filetype}" ...
366         file-name "{filepre}_hist_drifttime{filepost}"
367     !open meta
368     !act meta
369 Endif
370 Call plot_histogram(drift, ...
371     "Drift time [ns]", "Electron drift time")
372 Call plot_comment('UP-LEFT',"Magnetic field: {magnetic} Gauss")
373 Call plot_comment('DOWN-LEFT',"Bias voltage: {V_Bias} Volts")
374 Call plot_end
375 If file then
376     !deact meta
377     !close meta
378     !del meta
379 Endif
380
381 If file then
382     !add meta type "{filetype}" ...
383         file-name "{filepre}_hist_offset{filepost}"
384     !open meta
385     !act meta
386 Endif
387 Call plot_histogram(offset, ...
388     "r [cm]", "Electron offset")
389 Call plot_comment('UP-LEFT',"Magnetic field: {magnetic} Gauss")
390 Call plot_comment('DOWN-LEFT',"Bias voltage: {V_Bias} Volts")
391 Call plot_end
392 If file then
393     !deact meta
394     !close meta
395     !del meta
396 Endif
397
398 If file then
399     !add meta type "{filetype}" ...
400         file-name "{filepre}_hist_start_x{filepost}"
401     !open meta
402     !act meta
403 Endif
404 Call plot_histogram(hx_start, ...
405     "x [cm]", "Distribution of emitted electrons from the EGA")
406 Call plot_comment('UP-LEFT',"Magnetic field: {magnetic} Gauss")
407 Call plot_comment('DOWN-LEFT',"Bias voltage: {V_Bias} Volts")
408 Call plot_end
409 If file then
410     !deact meta
411     !close meta
412     !del meta
413 Endif
414
415 If file then
416     !add meta type "{filetype}" ...
417         file-name "{filepre}_hist_end_x{filepost}"
418     !open meta
```

## APPENDIX A. GARFIELD SOURCE CODE

---

```
419         !act meta
420     Endif
421     Call plot_histogram(hx_end, ...
422         "x [cm]", "Distribution of electrons on MCP")
423     Call plot_comment('UP-LEFT',"Magnetic field: {magnetic} Gauss")
424     Call plot_comment('DOWN-LEFT',"Bias voltage: {V_Bias} Volts")
425     Call plot_end
426     If file then
427         !deact meta
428         !close meta
429         !del meta
430     Endif
431
432
433     If file then
434         !add meta type "{filetype}" ...
435             file-name "{filepre}_hist_diff_x{filepost}"
436         !open meta
437         !act meta
438     Endif
439     global diff_x = hx_end-hx_start
440     Call plot_histogram(diff_x, ...
441         "x [cm]", "Difference in electron distribution")
442     Call plot_comment('UP-LEFT',"Magnetic field: {magnetic} Gauss")
443     Call plot_comment('DOWN-LEFT',"Bias voltage: {V_Bias} Volts")
444     Call plot_end
445     If file then
446         !deact meta
447         !close meta
448         !del meta
449     Endif
450
451     If file then
452         !add meta type "{filetype}" ...
453             file-name "{filepre}_hist_start_z{filepost}"
454         !open meta
455         !act meta
456     Endif
457     Call plot_histogram(hz_start, ...
458         "z [cm]", "Distribution of emitted electrons from the EGA")
459     Call plot_comment('UP-LEFT',"Magnetic field: {magnetic} Gauss")
460     Call plot_comment('DOWN-LEFT',"Bias voltage: {V_Bias} Volts")
461     Call plot_end
462     If file then
463         !deact meta
464         !close meta
465         !del meta
466     Endif
467
468     If file then
469         !add meta type "{filetype}" ...
470             file-name "{filepre}_hist_end_z{filepost}"
471         !open meta
472         !act meta
473     Endif
474     Call plot_histogram(hz_end, ...
475         "z [cm]", "Distribution of electrons on MCP")
476     Call plot_comment('UP-LEFT',"Magnetic field: {magnetic} Gauss")
477     Call plot_comment('DOWN-LEFT',"Bias voltage: {V_Bias} Volts")
478     Call plot_end
479     If file then
480         !deact meta
481         !close meta
482         !del meta
483     Endif
```

## A.1. ELECTRON DRIFT FROM EGP

---

```
484
485 If file then
486     !add meta type "{filetype}" ...
487         file-name "{filepre}_hist_diff_z{filepost}"
488     !open meta
489     !act meta
490 Endif
491 global diff_z = hz_end-hz_start
492 Call plot_histogram(diff_z, ...
493     "z [cm]", "Difference in electron distribution")
494 Call plot_comment('UP-LEFT',"Magnetic field: {magnetic} Gauss")
495 Call plot_comment('DOWN-LEFT',"Bias voltage: {V_Bias} Volts")
496 Call plot_end
497 If file then
498     !deact meta
499     !close meta
500     !del meta
501 Endif
502
503 If file then
504     !add meta type "{filetype}" ...
505         file-name "{filepre}_hist_start_z_zoom{filepost}"
506     !open meta
507     !act meta
508 Endif
509 Call plot_histogram(hz_start_2, ...
510     "z [cm]", "Distribution of emitted electrons from the EGA")
511 Call plot_comment('UP-LEFT',"Magnetic field: {magnetic} Gauss")
512 Call plot_comment('DOWN-LEFT',"Bias voltage: {V_Bias} Volts")
513 Call plot_end
514 If file then
515     !deact meta
516     !close meta
517     !del meta
518 Endif
519
520 If file then
521     !add meta type "{filetype}" ...
522         file-name "{filepre}_hist_end_z_zoom{filepost}"
523     !open meta
524     !act meta
525 Endif
526 Call plot_histogram(hz_end_2, ...
527     "z [cm]", "Distribution of electrons on MCP")
528 Call plot_comment('UP-LEFT',"Magnetic field: {magnetic} Gauss")
529 Call plot_comment('DOWN-LEFT',"Bias voltage: {V_Bias} Volts")
530 Call plot_end
531 If file then
532     !deact meta
533     !close meta
534     !del meta
535 Endif
536
537 If file then
538     !add meta type "{filetype}" ...
539         file-name "{filepre}_hist_diff_z_zoom{filepost}"
540     !open meta
541     !act meta
542 Endif
543 global diff_z_2 = hz_end_2-hz_start_2
544 Call plot_histogram(diff_z_2, ...
545     "z [cm]", "Difference in electron distribution")
546 Call plot_comment('UP-LEFT',"Magnetic field: {magnetic} Gauss")
547 Call plot_comment('DOWN-LEFT',"Bias voltage: {V_Bias} Volts")
548 Call plot_end
```

## APPENDIX A. GARFIELD SOURCE CODE

---

```
549 If file then
550     !deact meta
551     !close meta
552     !del meta
553 Endif
554
555 If file then
556     !add meta type "{filetype}" ...
557     file-name "{filepre}_hist_velocity{filepost}"
558     !open meta
559     !act meta
560 Endif
561 Call plot_histogram(velocity, "m/s", "Initial electron velocity")
562 Call plot_comment('UP-LEFT',"Magnetic field: {magnetic} Gauss")
563 Call plot_comment('DOWN-LEFT',"Bias voltage: {V_Bias} Volts")
564 Call plot_end
565 If file then
566     !deact meta
567     !close meta
568     !del meta
569 Endif
570
571 If file then
572     !add meta type "{filetype}" ...
573     file-name "{filepre}_hist_energy{filepost}"
574     !open meta
575     !act meta
576 Endif
577 Call plot_histogram(energy, "eV", "Initial electron energy")
578 Call plot_comment('UP-LEFT',"Magnetic field: {magnetic} Gauss")
579 Call plot_comment('DOWN-LEFT',"Bias voltage: {V_Bias} Volts")
580 Call plot_end
581 If file then
582     !deact meta
583     !close meta
584     !del meta
585 Endif
```

## A.2 Electron drift from wires

```

...
230
231 For irndm From 1 To nrndm/12 Do
232 For iw From 1 To 12 Do
233
234   *Initial velocity of electron [cm/microsec]
235   *   global E = rnd_exponential(gamma) // [eV]
236   global E = E_ave/2*rnd_gamma(2) // [eV]
237   global v = 59.3*sqrt(E) // [cm/us]
238   global theta = 3.14*rnd_uniform
239   global phi = 6.28*rnd_uniform
240   global vy = -v*cos(theta)
241   global vx = v*sin(theta)*cos(phi)
242   global vz = v*sin(theta)*sin(phi)
243
244   global y = wire - 0.005*cos(theta)
245   global x = (iw-6.5)*wire_p + 0.005*cos(phi)
246   global z = wire_l*(rnd_uniform-0.5)
247
248
249   *If entier(irndm/10)*10=irndm Then
250     *Say "i = {irndm}/{nrndm/12}"
251     *say "E = {E} [eV]"
252     *say "v = {v} [cm/microsec]"
253     *Say "vx, vy, vz = {vx, vy, vz} [cm/microsec]"
254     *Say "x,y,z = {x,y,z}"
255     *Say "x_end, z_end = {x_end, z_end}"
256     *Say "Drift line ended with status {status}, t={time}, {nstep} steps"
257     *Say " "
258   *endif
259
260   * Simulate electron drift in vacuum
261   call drift_vacuum_electron(x,y,z, vx,vy,vz, status, time)
262   Call drift_information( ...
263     'steps',nstep,'x_end',x_end,'y_end',y_end,'z_end',z_end)
264   * Say "Drift line ended with status {status}, t={time}, {nstep} steps"
265   * Say "x,y,z = {x,y,z}"
266   * Say "x_end, y_end, z_end = {x_end, y_end, z_end}"
...

```

### A.3 Electron drift considering bias angle

```
...
223
224 For irndm From 1 To nrndm Do
225   *Startpoint of electron [cm] At Electron generator array
226   *   global x = -1 + 2*(irndm-1)/(nrndm-1)
227   *   global x = -ega_x/2 + ega_x*(irndm-1)/(nrndm-1)
228   global x = -ega_x/2 + ega_x*rnd_uniform
229   global y = ega
230   global z = -ega_z/2 + ega_z*rnd_uniform
231
232   *Initial velocity of electron [cm/microsec]
233   global E = rnd_exponential(gamma) // [eV]
234   global v = 59.3*sqrt(E) // [cm/us]
235   *   global theta = 0.1*(2*rnd_uniform-1)
236   *   global phi = 6.28*rnd_uniform
237   *   global vy = -v*cos(theta)
238   *   global vx = v*sin(theta)*cos(phi)
239   *   global vz = v*sin(theta)*sin(phi)
240   * Angle: 8 +/- 1 deg
241   global theta = 0.14+0.017*(2*rnd_uniform-1)
242   *   global phi = 6.28*rnd_uniform
243   global vy = -v*cos(theta)
244   global vx = v*sin(theta)
245   global vz = v*sin(theta)
...

```

# Appendix B

## Technical Drawings

As reference, the most important of the technical drawings of the IPM are included here. The first drawing is an overview of the complete inner part of the IPM. The schematics and a photo of this part is shown in Fig. 1.2 in the introduction chapter.

The next two technical drawings show changes made to the IPM in order to integrate the EGP in the system. The modifications made to the cathode (the upper negative electrode), and the shielding ground plate (the wall of the tank), are shown.





EXISTING NUMBER	2	DATE		DESIGNER		APPROVED	
1	NEW STEEL SHEET PILING	1	14.5.2015				
2	NEW STEEL SHEET PILING	1	14.5.2015				
3	NEW STEEL SHEET PILING	1	14.5.2015				
4	NEW STEEL SHEET PILING	1	14.5.2015				
5	NEW STEEL SHEET PILING	1	14.5.2015				
6	NEW STEEL SHEET PILING	1	14.5.2015				
7	NEW STEEL SHEET PILING	1	14.5.2015				
8	NEW STEEL SHEET PILING	1	14.5.2015				
9	NEW STEEL SHEET PILING	1	14.5.2015				
10	NEW STEEL SHEET PILING	1	14.5.2015				
11	NEW STEEL SHEET PILING	1	14.5.2015				
12	NEW STEEL SHEET PILING	1	14.5.2015				
13	NEW STEEL SHEET PILING	1	14.5.2015				
14	NEW STEEL SHEET PILING	1	14.5.2015				
15	NEW STEEL SHEET PILING	1	14.5.2015				
16	NEW STEEL SHEET PILING	1	14.5.2015				
17	NEW STEEL SHEET PILING	1	14.5.2015				
18	NEW STEEL SHEET PILING	1	14.5.2015				
19	NEW STEEL SHEET PILING	1	14.5.2015				
20	NEW STEEL SHEET PILING	1	14.5.2015				
21	NEW STEEL SHEET PILING	1	14.5.2015				
22	NEW STEEL SHEET PILING	1	14.5.2015				
23	NEW STEEL SHEET PILING	1	14.5.2015				
24	NEW STEEL SHEET PILING	1	14.5.2015				
25	NEW STEEL SHEET PILING	1	14.5.2015				
26	NEW STEEL SHEET PILING	1	14.5.2015				
27	NEW STEEL SHEET PILING	1	14.5.2015				
28	NEW STEEL SHEET PILING	1	14.5.2015				
29	NEW STEEL SHEET PILING	1	14.5.2015				
30	NEW STEEL SHEET PILING	1	14.5.2015				
31	NEW STEEL SHEET PILING	1	14.5.2015				
32	NEW STEEL SHEET PILING	1	14.5.2015				
33	NEW STEEL SHEET PILING	1	14.5.2015				
34	NEW STEEL SHEET PILING	1	14.5.2015				
35	NEW STEEL SHEET PILING	1	14.5.2015				
36	NEW STEEL SHEET PILING	1	14.5.2015				
37	NEW STEEL SHEET PILING	1	14.5.2015				
38	NEW STEEL SHEET PILING	1	14.5.2015				
39	NEW STEEL SHEET PILING	1	14.5.2015				
40	NEW STEEL SHEET PILING	1	14.5.2015				
41	NEW STEEL SHEET PILING	1	14.5.2015				
42	NEW STEEL SHEET PILING	1	14.5.2015				
43	NEW STEEL SHEET PILING	1	14.5.2015				
44	NEW STEEL SHEET PILING	1	14.5.2015				
45	NEW STEEL SHEET PILING	1	14.5.2015				
46	NEW STEEL SHEET PILING	1	14.5.2015				
47	NEW STEEL SHEET PILING	1	14.5.2015				
48	NEW STEEL SHEET PILING	1	14.5.2015				
49	NEW STEEL SHEET PILING	1	14.5.2015				
50	NEW STEEL SHEET PILING	1	14.5.2015				
51	NEW STEEL SHEET PILING	1	14.5.2015				
52	NEW STEEL SHEET PILING	1	14.5.2015				
53	NEW STEEL SHEET PILING	1	14.5.2015				
54	NEW STEEL SHEET PILING	1	14.5.2015				
55	NEW STEEL SHEET PILING	1	14.5.2015				
56	NEW STEEL SHEET PILING	1	14.5.2015				
57	NEW STEEL SHEET PILING	1	14.5.2015				
58	NEW STEEL SHEET PILING	1	14.5.2015				
59	NEW STEEL SHEET PILING	1	14.5.2015				
60	NEW STEEL SHEET PILING	1	14.5.2015				
61	NEW STEEL SHEET PILING	1	14.5.2015				
62	NEW STEEL SHEET PILING	1	14.5.2015				
63	NEW STEEL SHEET PILING	1	14.5.2015				
64	NEW STEEL SHEET PILING	1	14.5.2015				
65	NEW STEEL SHEET PILING	1	14.5.2015				
66	NEW STEEL SHEET PILING	1	14.5.2015				
67	NEW STEEL SHEET PILING	1	14.5.2015				
68	NEW STEEL SHEET PILING	1	14.5.2015				
69	NEW STEEL SHEET PILING	1	14.5.2015				
70	NEW STEEL SHEET PILING	1	14.5.2015				
71	NEW STEEL SHEET PILING	1	14.5.2015				
72	NEW STEEL SHEET PILING	1	14.5.2015				
73	NEW STEEL SHEET PILING	1	14.5.2015				
74	NEW STEEL SHEET PILING	1	14.5.2015				
75	NEW STEEL SHEET PILING	1	14.5.2015				
76	NEW STEEL SHEET PILING	1	14.5.2015				
77	NEW STEEL SHEET PILING	1	14.5.2015				
78	NEW STEEL SHEET PILING	1	14.5.2015				
79	NEW STEEL SHEET PILING	1	14.5.2015				
80	NEW STEEL SHEET PILING	1	14.5.2015				
81	NEW STEEL SHEET PILING	1	14.5.2015				
82	NEW STEEL SHEET PILING	1	14.5.2015				
83	NEW STEEL SHEET PILING	1	14.5.2015				
84	NEW STEEL SHEET PILING	1	14.5.2015				
85	NEW STEEL SHEET PILING	1	14.5.2015				
86	NEW STEEL SHEET PILING	1	14.5.2015				
87	NEW STEEL SHEET PILING	1	14.5.2015				
88	NEW STEEL SHEET PILING	1	14.5.2015				
89	NEW STEEL SHEET PILING	1	14.5.2015				
90	NEW STEEL SHEET PILING	1	14.5.2015				
91	NEW STEEL SHEET PILING	1	14.5.2015				
92	NEW STEEL SHEET PILING	1	14.5.2015				
93	NEW STEEL SHEET PILING	1	14.5.2015				
94	NEW STEEL SHEET PILING	1	14.5.2015				
95	NEW STEEL SHEET PILING	1	14.5.2015				
96	NEW STEEL SHEET PILING	1	14.5.2015				
97	NEW STEEL SHEET PILING	1	14.5.2015				
98	NEW STEEL SHEET PILING	1	14.5.2015				
99	NEW STEEL SHEET PILING	1	14.5.2015				
100	NEW STEEL SHEET PILING	1	14.5.2015				

